Microwave Characteristics of Particulate Magnetic Composites

Author:
Cameron Patrick Gallagher

Supervisors:
Prof. Roy Sambles
Prof. Alistair Hibbins

This thesis is submitted by Cameron Patrick Gallagher to The University of Exeter as a thesis for the degree of Doctor of Philosophy in Physics

September 2018

I certify that all material in this thesis which is not my own work has been identified and that any material that has previously been submitted and approved for the award of a degree by this or any other University has been acknowledged.

Signed:

_____

Date:

_____

Abstract

Microwave Characteristics of Particulate Magnetic Composites

Spherical magnetic particles have recently become of interest for applications in microwave communications devices as they exhibit magnetic absorption modes at frequencies much larger than conventional materials. These higher order modes allow composites comprising spherical magnetic particles in dielectric matrices to have relative permeabilities above unity at frequencies surpassing conventional magnetic materials. The higher order magnetic modes seen in spherical iron powders are a result of the vortex domain structure of magnetic spheres and exist also in magnetic spherical shells. Composite materials containing these magnetic spheres have use in miniaturisation of communications devices and allow access to frequency bands previously unattainable for communications as the increase in permeability at high frequencies will not only increase the refractive index of the material, but also decrease the impedance of the material, improving impedance matching to air. This thesis presents work for the investigation of higher order modes in spherical iron powders, particularly carbonyl iron powders, with the intent to demonstrate how properties such as particle size distribution affects the higher order resonances exhibited.

A stripline technique for broadband characterisation of dielectric and magnetic composites is presented in the thesis, which demonstrates an ability to extract the relative permittivity and permeability of composites across an unprecedented broadband frequency range of 0.2 - 50 GHz. Although the relative permittivity and permeability of composites was able to be extracted for most cases, the refractive index of materials was shown to be significantly more resistant to uncertainty across broad frequencies. This technique employed a simple method for sample manufacture by wet-casting composites for characterisation, giving a fast and reliable method for characterising small amounts of material across a frequency range that surpasses most readily available methods. The technique was used for characterisation of several carbonyl iron powder grades.

The carbonyl iron grades were imaged by scanning electron microscopy (SEM) analysis to give particle size distributions that were able to be compared between grades to allow an investigation into how the particle size distribution for carbonyl iron powders affects their microwave characteristics. Particle size distribution was confirmed to be a strong factor when considering the strength and position in frequency of these higher order resonances, so a technique was developed for filtration of powders into subgrades with different particle size distributions and average particle sizes. The results of this investigation displayed that the emergence of higher order magnetic absorption modes in carbonyl iron is heavily dependent on the average size and distribution of sizes for the powder used. The filtration technique developed is able to be used for filtration of spherical particles in the single micron size regime and uses only the flow of air through a set of stainless steel tubing and glass bottles. This experimental method is not only cheap, but is simple to assemble and achieves filtration of powders smaller than most mechanical sieves are capable of filtering.

Finally, an investigation into the behaviour of these higher order modes under externally applied magnetic bias fields was performed. Samples were subject to a DC magnetic field during characterisation and the complex refractive index of composites was extracted as a field dependent value across the frequency range 0.2 - 30 GHz. The results showed that the primary absorption mode of these composites, at low GHz frequencies, was strongly affected by the application of a DC bias field, changing in both intensity and position in frequency. The higher order modes showed a less strong dependence on DC bias field strength until saturation fields were reached, and the modes were suppressed. The higher order modes not being supported at high DC bias fields is indicative of the vortex domain structure being necessary for higher order spherical modes to exist in magnetic powders.

Acknowledgements

I would like to acknowledge my supervisors, Roy and Al, for providing me much needed support and input throughout the duration of my thesis. They have been a great source of motivation as well as a wealth of knowledge. I would also like to acknowledge the entire workshop team in our physics department. Nick Cole and Peter Savage have tirelessly worked to produce increasingly fiddly samples and have enthusiastically approached any problem I've presented to them to help me arrive at an effective solution.

I dedicate this thesis to my mother, for providing me with the upbringing that has allowed me to follow my aspirations and be happy whilst stressing that my mind isn't to go to waste. Also I dedicate this thesis to my grandfather, for instilling the desire to understand the workings of life around me. Without these two people in my life, I would not have made it to where I am today.

Thanks.

Contents

Abstract **iii**

Acknowledgements **v**

1 Introduction **1**
1.1 Research Objectives 1
1.1.1 The Frequency Response of Magnetic Materials 1
1.2 Thesis Outline 3
1.2.1 The Broadband Frequency Response of Spherical Magnetic Particle – Dielectric Composites 3
1.2.2 The Properties of Carbonyl Iron Powder 4
1.2.3 The Particle Size Dependence of Higher order Spherical Magnetic Modes 4
1.2.4 The Effect of DC Magnetic Bias Field on Higher order Spherical Magnetic Modes 5
1.3 Publications, Presentations and Conferences 6
1.3.1 Peer-Reviewed Publications 6
1.3.2 Presentations 6
1.3.3 Poster Presentations 7
1.3.4 Collaborations/ Industry Contributions 7

2 Background **9**
2.1 Introduction 9
2.2 Permeability 9
2.3 Magnetism 10
2.3.1 Diamagnetism 10
2.3.2 Paramagnetism 10
2.3.3 Ferromagnetism 11
2.3.4 Antiferromagnetism 11
2.3.5 Ferrimagnetism 12

2.3.6 Hysteresis . . . 12
2.3.7 Magnetic Domains . . . 14
Domain Walls . . . 15
2.3.8 Exchange Energy . . . 16
2.3.9 Magnetocrystalline Anisotropy . . . 16
2.4 The Demagnetising Field . . . 18
2.4.1 Skin Depth . . . 18
2.5 The Microwave Frequency Response of Magnetic Materials . . . 19
2.5.1 Snoek's Law . . . 20
2.6 Ferromagnetic Resonance in Thin Films . . . 21
2.7 Spherical Magnetic Particles . . . 23
2.7.1 Spherical Shell Particles . . . 23
2.7.2 Single Domain Particles & Superparamagnetism . . . 24
2.8 Magnetic Composites . . . 25
2.8.1 Carbonyl Iron Powder . . . 26
Production of Carbonyl Iron Powder . . . 27
Properties of CIP . . . 28
2.9 The Scanning Electron Microscope and Focused Ion Beam . . . 28
2.9.1 Scanning Electron Microscope . . . 28
2.9.2 Focused Ion Beam . . . 29
2.10 The Vector Network Analyser . . . 29
2.10.1 VNA Calibration . . . 29
2.11 Transmission Line Techniques . . . 30
Coaxial Transmission Line . . . 31
Waveguide Transmission Line . . . 32
Stripline Transmission Line . . . 32
2.11.1 Scattering Parameters . . . 35
2.11.2 Extraction of Electromagnetic Properties . . . 38
2.11.3 The Nicolson Ross-Weir Method . . . 38
2.11.4 The Three-Layer Sliding Window Fresnel Method . . . 39
2.12 Conclusions . . . 39

3 Methods **41**
3.1 Introduction . . . 41
3.2 Composite Fabrication . . . 41
3.2.1 Cold-press Technique . . . 42

3.2.2 Wet-cast Technique 42
3.3 Particle Size Filtration 44
3.3.1 Mechanical Sifting 44
3.3.2 Air Elutriation 44
3.4 Stripline Tranisition Region Optimisation 47
3.5 Parameter Extraction 48
3.5.1 T-Matrix Formulation 48
3.5.2 Short-measurement Calibration of the Stripline 50
3.5.3 Offset Sample Correction 56
3.6 Particle Cross-section Analysis 58
3.6.1 Focused Ion Beam Sectioning 58
3.6.2 Sectioning by Polishing 60
3.7 Particle Size Analysis 62
3.7.1 Laser Light Diffraction Analysis 62
3.7.2 SEM Analysis 62
3.8 List of Materials 64
3.9 Conclusions 64

4 An Improved Stripline Technique for the Electromagnetic Characterisation of Composite Materials 67
4.1 Introduction 67
4.2 Method 68
4.2.1 Electromagnetic Modelling of Stripline Transmission Lines 68
4.2.2 Upper Cut-off of Stripline 69
4.2.3 Optimization of the Stripline Conductor Geometry . . 70
4.2.4 Sample Fabrication 75
4.2.5 Measurement Process 77
4.3 Results 78
4.3.1 Dielectric Composites 78
4.3.2 Sample Placement in the Stripline 82
4.3.3 Frequency Dependent Expression of Relative Permittivity 84
4.3.4 Magnetic Composite Parameter Extraction 89
4.4 Broader Frequency Characterisation of Composites 94
4.5 Chapter Summary 98

5 Broadband Characterisation of Carbonyl Iron Powder – Polyurethane Composites **101**
5.1 Introduction . . . 101
5.2 Method . . . 103
5.2.1 Particle Cross-section Analysis . . . 103
5.2.2 Particle Size Analysis . . . 103
SEM Analysis . . . 103
5.2.3 Sample Preparation . . . 104
5.3 Results . . . 104
5.3.1 Cross-section Analysis . . . 105
5.3.2 Particle Size Analysis . . . 107
Laser Light Diffraction . . . 107
SEM Analysis . . . 108
5.3.3 Electromagnetic Properties Comparisons . . . 113
"Hard" vs. "Soft" . . . 113
"Hard" Particle Size Effect . . . 114
Coating Effect . . . 115
5.3.4 Particle Size Effect on Refractive Index . . . 117
5.3.5 Volume Fraction Dependence on Higher Order Modes 120
5.4 Nanoparticle Composite Characterisation . . . 120
5.5 Chapter Summary . . . 125

6 Particle Size Filtration by Air Elutriation **127**
6.1 Introduction . . . 127
6.2 Method . . . 128
6.3 Results . . . 129
6.3.1 Particle Size Filtration . . . 129
Removal of Eluate . . . 129
Collection of Eluate . . . 130
6.3.2 Electromagnetic Characterisation . . . 134
6.4 Chapter Summary . . . 137

7 Effect of DC Magnetic Bias Field on Spherical Magnetic Modes **141**
7.1 Introduction . . . 141
7.2 Method . . . 142
7.3 Results . . . 143

7.3.1 Filtered Particles 145
7.3.2 Compared Volume Loading 148
7.4 Chapter Summary 150

8 Conclusions and Future Work **151**

Bibliography **159**

List of Figures

2.1 Hysteresis curves for hard and soft magnetic materials where the initial and maximum susceptibilities are given by the gradient of the virgin curve at low and high magnetic fields, respectively, shown by the red lines. The width or area of a hysteresis loop is representative of the materials magnetic loss associated with the force required to rotate magnetic moments 13

2.2 This figure shows the reduction in stray field when splitting a simple geometry magnetic material into domains. As can be seen, the stray field around the material is reduced and confined closer to the surface when more domains are added. This lowers the magnetostatic energy of the system but eventually the cost of adding domain walls will outweigh the reduction in magnetostatic energy, at which point a stable domain structure is formed. 14

2.3 This figure demonstrates the motion of domain walls in the presence of an applied magnetic field. As the external field is increased in strength, domains with components pointing in the direction of field increase in size, while those opposing the field shrink. Once domains only exist that are pointing in the direction of the field, a final domain is formed that, upon saturation, is completely aligned with the applied field. The field at which saturation occurs is referred to as the saturation magnetisation, H_S. 15

2.4 This figure shows the magnetic moments across domain walls that are narrow and wide. The rotation in magnetic moments across the sample will have a width that is dependent upon the magnetocrystalline and exchange energies. This rotation of magnetic moments through 180° can occur in the plane of magnetisation, as in Néel walls, or out of the plane of magnetisation as in Bloch walls. 16

2.5 Diagrams showing **(a)** the typical magnetisation curve for a magnetic material along the easy and hard axes of magnetisation and **(b)** The crystal structure of bcc iron, showing easy, intermediate and hard axes of magnetisation. *Replicated from Magnetic Materials: Fundamentals and Applications[47].* 17
2.6 Schematics showing the B-Field lines, **(a)**, and induced H-field lines, **(b)**, for an anisotropic magnetic material, magnetised along the long axis. The H-field outside of the material is the stray field, H_{Stray}, while the H-field inside the material is named the demagnetising field, H_d. 19
2.7 Schematic showing the magnetic moments in a circular thin film with vortex domain state. magnetic moments circulate in the plane of the thin film, with a singularity at the centre that has a magnetic moment pointing out of the plane. 22
2.8 SEM micrograph showing an example section of CIP, indicating the onionlike microstructure of "hard" grade powders. The lighter boundaries of the structure are the iron carbide, whilst the darker regions are iron rich regions. *Image taken at University of Exeter* 27
2.9 Diagram showing the electric and magnetic field lines in a coaxial transmission line. 31
2.10 Diagram showing the electric and magnetic field lines in a rectangular waveguide transmission line. 32
2.11 **(a)** Schematic showing the cross section of the stripline transmission line, with metal being indicated by solid black lines. **(b)** Diagram showing the electric and magnetic field lines in a stripline transmission line. This sample is insterted into the stripline above the cntral conductor, and a second inverted sample is placed beneath such that the steps of each sample are on either side of the conductor. 33
2.12 Schematic showing a possible sample geometry for use in stripline transmission lines. The sample has a step along the width that is for accomodating the central conducting strip. Pairs of these samples are made with the same value of l_{Sam} such that the whole cross section of the stripline may be filled with sample. 33

2.13 Schematic showing the design for the stripline assembly. A brass housing is produced that can accomodate coaxial adaptors at either end. SMA adaptors are soldered to a copper conducting strip such that the strip may be suspended between the top and bottom ground planes by the adapters. . . . 34
2.14 Schematic showing the typical transition region from coaxial input to stripline field applicator. A 20° taper is used for the transition region from coaxial line to stripline. 35
2.15 **(a)** Diagram showing the reflected and transmitted signals for a wave incident upon a sample in free-space, at perpendicular incidence, and **(b)** Graph showing the typical model amplitudes of S-parameters when using a dielectric sample, with $\epsilon_r = 2.05 + 0.03i$, $\mu_r = 1.0 + 0.0i$ and a length of 5 mm. These values are calculated from Equation (2.7). 36
2.16 Diagram showing the signal flow diagram for reflected and transmitted signals when using a transmission device. 37
2.17 Graph showing the typical amplitudes of S-parameters when using a dielectric sample, with $\epsilon_r = 2.05 + 0.03i$, $\mu_r = 1.0 + 0.0i$ and a length of 5 mm in between two unknown lossy reflection boundaries. The oscillations in the data cannot be accounted for without knowing the S-parameters of the reflection boundaries. 37

3.1 Figure displaying the Teflon mould used for wet-casting samples. 43
3.2 Schematic showing how a glass bottle may be used for the air elutriation experiment. 45
3.3 Schematic showing the experimental setup for air elutriation with a second collection chamber attached in series to the filtration chamber. This second chamber collects the particles filtered from the bulk. 47
3.4 Signal flow diagram showing the positions at which shorting bars are placed in order to gain information on the S-parameters for the transition regions. 52

3.5 Extracted sample S-parameters for a set of S-parameters measured for the stripline geometry with a 5 mm polyurethane sample inserted. The sample S-parameters have been extracted using short calibration measurements with maximum spacings of **(a)** 9.3 mm, **(b)** 6.2 mm, and **(c)** 3.3 mm. 54
3.6 Phases of the S_{11} measurement for the shorted stripline with shorts placed at average distances from eachother of **(a)** 4.6 mm,
(b) 3.1 mm, and **(c)** 1.7 mm. 55
3.7 Graphs showing for a 5 mm polyurethane sample from the measured stripline geometry, the extracted sample S-parameters extracted using measurement of all previous short readings together with measurements of the empty stripline with and without calibration standards attached at each end. 56
3.8 Schematic showing the three-layered system that is considered when fitting to de-embedded sample S-parameters. The model assumes that the sample is not centrally placed, and the position of the sample must be determined from analysing the phases of the reflected signals. 57
3.9 Figures comparing the uncorrected **(a)** and corrected **(b)** phases for the reflected signals for a test sample that is offset by a distance d from the centre of the sample region. 57
3.10 Figure demonstrating the process for attempting to image the section of a carbonyl iron particle by use of a dualbeam system. **(a)** First the particle is imaged and an area chosen to be cut by focused ion beam (FIB). **(b)** The FIB is used to section the particle, etching until all of the material has been removed. **(c)** Image the newly sectioned particle by scanning electron microscope. All images taken using SEM with acceleration voltage of 10.0 kV and beam current of 0.54 nA. 59

3.11 Schematic showing a method used in an attempt to inspect the internal structure of a carbonyl iron particle by use of a SEM-FIB dualbeam system. **(a)** First the particle is sectioned with the focused ion beam. **(b)** The particle is rotated such that the newly exposed section is perpendicular to the FIB. **(c)** FIB is used to polish the surface of the section. **(d)** Rotate sample and tilt such that the section is perpendicular to the SEM objective and image section. 60
3.12 This figure displays two high-contrast SEM images of the resultant section when using the dualbeam system with an additional polishing step applied by the FIB to etch the surface of the newly sectioned particle. Images taken with SEM using 5.0 kV acceleration voltage, beam current of 1.6 nA and through-lens-detection of secondary electrons. 61
3.13 **(a)** SEM micrograph example for particle size analysis of CIP HQ. **(b)** Processed image for use in particle detection and area extraction. The image has had a binary function applied to convert the image to purely black and white pixels, and a watershed function has been applied to separate regions of joined particles. 63

4.1 Comparison of modelled and measured S-parameters for an empty stripline geometry. 69
4.2 Comparison of modelled and measured S-parameters for a stripline geometry with a 5 mm Teflon sample inserted. 70
4.3 Figure showing the absolute S-parameters for a stripline device with single angle taper transition, height of 3 mm and strip width of 3.86 mm. The cavity lengths for each model were **(a)** 20 mm and **(b)** 50 mm. 71
4.4 (a) Schematic showing the stripline geometry. Coaxial adapters screw into the walls of a brass housing, and the center conducting strip is connected using coaxial pins. (b) Close-up schematic of the transition region from coaxial pin to central strip shape. (c) Photograph of the stripline device. (d) Schematic showing the sample placement in the stripline. Samples are placed above and below the central conductor such that the step in each sample is either side of the line. 72

4.5 Graph showing the modelled S-parameters for the optimised stripline 73
4.6 Graphs showing the measured S-parameters for the optimised stripline. 73
4.7 Graph showing the modelled S-parameters for the optimised stripline geometry with a cavity length of 50 mm. 74
4.8 Measured densities of CIP ES – Polyurethane (red) and $BaTiO_3$ – Polyurethane (blue) composites for each percentage volume loading. Dashed lines show the predicted densities with ρ_{CIP}=7800 kg/m^3 and ρ_{BaTiO_3}=6080 kg/m^3 76
4.9 Magnitude **(a)** and phase **(b)** for the measured S-parameters of the stripline transmission line with a 5.04 mm pure polyurethane sample inserted. 78
4.10 Magnitude **(a)** and phase **(b)** for the extracted sample S-parameters for a 5.04 mm pure polyurethane sample, extracted from the measured S-parameters for the combined system. 78
4.11 Relative permittivity and permeability **(a)** with the characteristic impedance and refractive index **(b)** for the 5.04 mm pure polyurethane sample, extracted by fitting to S-parameters with Fresnel's equations and ϵ_r, μ_r as free variables. 79
4.12 Characteristic impedance of the polyurethane sample, directly calculated from Equation (4.2) (Black), compared with the characteristic impedance inferred from the fitted index (Red). 80
4.13 Relative permittivity **(a)** with the characteristic impedance and refractive index **(b)** for the 5.04 mm pure polyurethane sample, extracted by fitting to S-parameters and imposing $\mu_r = 1$. 81
4.14 Relative complex permittivity for $BaTiO_3$ – Polyurethane composites with increasing percentage volume of $BaTiO_3$. 81
4.15 Schematics showing erroneous sample placements that were modelled **(a)** Mismatch in sample positioning **(b)** Mismatch in sample propagation lengths **(c)** Chamfered sample interface **(d)** Sample rotation mismatch. 82

4.16 Graphs showing extracted relative permittivities for sample measurements with the following placement errors **(a)** Mismatch in sample positioning **(b)** Mismatch in sample propagation lengths **(c)** Chamfered sample interface **(d)** Sample rotation mismatch. 83
4.17 Graph showing the measured S-parameters for a pure polyurethane sample (Black) compared with the fitted S-parameters using Equation (4.4) to model the frequency dependent permittivity inserted into Fresnel equations. 85
4.18 Relative permittivity **(a)** with the characteristic impedance and refractive index **(b)** for the 5.04 mm pure polyurethane sample, extracted by fitting to S-parameters when imposing $\mu_r = 1$ and assuming that the permittivity has the frequency dependence, given by Equation (4.4). 86
4.19 Relative permittivity for $BaTiO_3$ samples, extracted using the Debye model of frequency dependent permittivity. Samples had volume loadings from 0%vol. - 25%vol. in 5%vol. increments. 87
4.20 Natural log of the real part of relative permittivity at 200 MHz for $BaTiO_3$ – Polyurethane composites with increasing percentage volume of $BaTiO_3$. The dashed line shows a linear fit to the data. 88
4.21 Relative complex permittivity for CIP ES – Polyurethane composites with increasing percentage volume loading of CIP. . . 90
4.22 Relative complex permeability for CIP ES – Polyurethane composites with increasing percentage volume loading of CIP. . . 90
4.23 Natural log of the real parts of relative permittivity and permeability at a frequency of 200 MHz, as a function of percentage volume loading for CIP – Polyurethane composites. The dashed lines show the results of a least squares, straight line fit to the data. 91
4.24 Refractive index for CIP ES – polyurethane composites with volume loading across the range 10%vol. - 40%vol. in 10%vol. increments. 92
4.25 Impedance for CIP ES – polyurethane composites with volume loading across the range 10%vol. - 40%vol. in 10%vol. increments. 92

4.26 Cole-Cole plot of the refractive index for CIP ES – polyurethane composites with volume loading across the range 10%vol. - 40%vol. in 10%vol. increments.. 93
4.27 Graphs showing the measured S-parameters for **(a)** a 4 mm PTFE sample and **(b)** a 3.9 mm pure polyurethane sample. . . 95
4.28 Graph showing the relative permittivity for polyurethane and PTFE across the frequency range 0.2 - 210 GHz. 96
4.29 Graphs showing the measured (Black) and fitted (Red) S-parameters for polyurethane samples measured across the frequency ranges **(a)** 0.2 - 50 GHz and **(b)** 150 - 210 GHz. 96
4.30 Graphs showing the measured (Black) and fitted (Red) S-parameters for PTFE samples measured across the frequency ranges **(a)** 0.2 - 50 GHz and **(b)** 150 - 210 GHz. 97

5.1 SEM micrographs of the cross section for CIP EW-I particles taken using the mechanical polishing technique. By comparing these images taken for the same grade, it is seen that there is great variation in the particle structure across the same powder. Images **(a-b)** show the anticipated onion ring structure, only with a variation in the way this structure has manifest itself. **(a)** shows a more defined boundary between layers and **(b)** shows a less explicit divide. Images **(c)**, and **(d)** show polycrystalline spheres with large and small grain sizes, respectively. 106
5.2 Typical SEM micrographs for the cross-sections of 800 nm particles obtained from a 3rd party supplier. 107
5.3 **(a)** Particle Size distribution and **(b)** cumulative sum of particle size distribution for CIP grades HS, ES and EM taken by Oxford using laser light diffraction equipment. The cumulative sum is taken by sequentially summing the value of volume percentage for each particle size until all data has been summed. 109

5.4 **(a)** Cumulative sum of the size distributions for CIP EM measured by Johnson Matthey using laser light diffraction techniques, comparing the results for a raw batch of powder (Black) with those for a sonicated batch (Red) **(b)** Cumulative sums of the particle size distributions for CIP EM measured in 3 different instances. One set are results from SEM imaging techniques at University of Exeter, and the two others are independently measured by Oxford and JM by laser light diffraction. 110
5.5 Particle size distribution (black) and cumulative sum of particle size distribution (red) for **(a)** CIP CM **(b)** CIP SM **(c)** CIP EW **(d)** CIP EW-I. Each of the distributions has been fitted to with a skewed Gaussian curve. From these curves, a full width at haf maximum (FWHM) is taken to give a numerical representation of the spread of data. 111
5.6 Particle size distribution (black) and cumulative sum of particle size distribution (red) for **(a)** CIP EM **(b)** CIP ES **(c)** CIP HS **(d)** CIP HQ and **(e)** 800 nm Fe. Each of the distributions has been fitted to with a skewed Gaussian curve. From these curves, a FWHM is taken to give a numerical representation of the spread of data. 112
5.7 **(a)** Complex relative permittivity and **(b)** relative permeability for CIP grades SM, EW, ES and CM. CIP grades SM and CM are both described as "soft" powders, possessing a polycrstalline internal structure, whereas CIP grades EW and ES are "hard", possessing the onion-like internal structure. 114
5.8 **(a)** Refractive index loss tangent and **(b)** refractive index Cole-Cole plot for CIP grades SM, EW, ES and CM in composites at 30%vol. loading for CIP. CIP grades SM and CM are both described as "soft" powders, possessing a polycrstalline internal structure, whereas CIP grades EW and ES are "hard", possessing the onion-like internal structure. 115
5.9 **(a)** Complex relative permittivity and **(b)** relative permeability for CIP grades EM, ES, EW and HQ in composites at 30%vol. loading for CIP. Each of these powder grades are "hard", possessing onion-like internal structure. 115

5.10 **(a)** Refractive index loss tangent and **(b)** refractive index Cole-Cole plot for CIP grades EM, ES, EW and HQ in composites at 30%vol. loading for CIP. Each of these powder grades are "hard", possessing onion-like internal structure. The plots are displayed in order of decreasing average particle size. 116
5.11 **(a)** Complex relative permittivity and **(b)** relative permeability for CIP grades EW and EW-I. These two grades are expected to be similar in size and internal structure, with the only difference between them being the existence of a coating on CIP grade EW-I, whereas CIP EW has not been coated. . . . 117
5.12 **(a)** Refractive index loss tangent and **(b)** refractive index Cole-Cole plot for CIP grades EW and EW-I. These two grades are expected to be similar in size and internal structure, with the only difference between them being the existence of a coating on CIP grade EW-I, whereas CIP EW has not been coated. . . . 117
5.13 **(a)** Size distributions as percentage volume and **(b)** cumulative sum of size distributions for CIP grades EM, EW-I, HS, HQ and 800 nm spherical iron powder. 118
5.14 **(a)** Real and **(b)** imaginary parts of index for CIP grades EM, EW-I, HS, HW and 800 nm Fe particles. Index is displayed across the frequency range 200 MHz - 30 GHz for composites containing 30%vol. CIP loading. 119
5.15 **(a)** Refractive index loss tangent and **(b)** refractive index Cole-Cole plot for CIP grades EM, EW-I, HS, HW and 800 nm Fe particles. Index is displayed across the frequency range 200 MHz - 30 GHz for composites containing 30%vol. CIP loading. 119
5.16 Loss tangent of refractive index for **(a)** CIP EM, **(c)** CIP EW-I, **(e)** CIP HS and Cole-Cole plot of complex parts for refractive index for **(b)** CIP EM, **(d)** CIP EW-I, **(f)** CIP HS. 121
5.17 Graphs showing preliminary results for the refractive index, **(a)**, and loss tangent of refractive index, **(b)**, of composites comprising 100 nm iron powder in polyurethane. 123
5.18 Graph comparing the refractive index loss tangents for composites comprising 100 nm Fe particles in polyurethane (Black) and 800 nm Fe particles in polyurethane (Red). Both composites are made with 30% volume loading of Fe powder. 123

6.1 **(a)** Particle size distribution for a sub-batch of CIP EM created by filtering at a volume flow rate of 0.6 LPM to remove particles. A skewed Gaussian fit is also plotted. **(b)** Cumulative sum of the histogram data normalised to total 100%. Dashed lines show the expected cutoff for maximum size of particles to be filtered from the bulk and in black is shown the particle size distribution and cumulative sum of the distribution for the raw, unfiltered CIP EM powder. 129
6.2 SEM micrographs showing particle sizes for **(a)** particles collected in the second chamber using a volume flow rate of 0.8 LPM, **(b)** particles collected in second chamber when using a volume flow rate of 1.5 LPM, **(c)** particles collected in the second chamber when using a volume flow rate of 2.5 LPM and **(d)** the particles left in the first chamber after all volume flow rates had been used. All images taken with an acceleration voltage of 10 kV and beam current of 0.13 nA, detecting secondary electrons at 5000x magnification. 131
6.3 **(a)** Particle size distribution for each batch of powder, displayed as a histogram scatter plot with a skewed Gaussian fit to each dataset. These Gaussian curves were used to calulate the FWHM for each curve, allowing an uncertainty to be provided. Dashed lines indicate the expected mean size for each batch, calculated as the midpoint between the cutoffs of the first and second chambers. **(b)** Cumulative sum of the particle size distribution for each batch of powder. Dashed lines again indicate the expected size for this batch, calculated from the midpoint between the cutoffs for the chambers at each volume flow rate. 132
6.4 **(a)** Particle size distribution and **(b)** cumulative sum of size siztribution for sub-batches of particles filtered from CIP EM in a repeated experiment. 133
6.5 Comparisons of the particle size distributions for 3 sub-grades of powder filtered from bulk batches of powder when using elutriation volume flow rates of **(a)** 0.8 LPM and **(b)** 1.5 LPM. . 134
6.6 Real, **(a)**, and imaginary **(b)** parts of refractive index for composites of polyurethane and the first set of sub-grades for CIP EM, filtered by the elutriation technique. 136

6.7 Real, **(a)**, and imaginary **(b)** parts of refractive index for composites of polyurethane and the second set of sub-grades for CIP EM, filtered by the elutriation technique in a repeated experiment. 136
6.8 Direct comparison of imaginary refractive index for each subgrade of CIP EM filtered through different experiments. 137
6.9 Refractive index loss tangent for composites formed from polyurethane and carbonyl iron powder CIP EM that has been split into sub grades by an elutriation technique. **(a)** shows the results for a first attempt of the experiment while **(b)** shows that for a repeated filtration. 137
6.10 Refractive index Cole-Cole plot for composites formed from polyurethane and carbonyl iron powder CIP EM that has been split into sub grades by an elutriation technique. **(a)** shows the results for a first attempt of the experiment while **(b)** shows that for a repeated filtration. 138

7.1 Schematic showing the positioning of the stripline device between two poles of an electromagnet for the experiment. DC magnetic bias field is applied perpendicular to wave propagation. 143
7.2 Absolute S-parameters for the empty stripline device with and without a magnetic DC bias field applied. 144
7.3 Refractive index for a 30%vol. composite containing 800 nm particles as a function of applied DC magnetic bias field, extracted using calibration parameters that were calculated only for the zero-field case. 144
7.4 Refractive index for a 30%vol. composite containing 800 nm particles as a function of applied DC magnetic bias field, extracted using calibration parameters that were calculated for each applied DC bias field. 145
7.5 Real **(a)**, and imaginary **(b)** parts of refractive index for composites comprising Batch #1 of the filtered particles from CIP EM, plotted with increasing DC magnetic bias field from 0 mT - 330 mT 146

7.6 Real **(a)**, and imaginary **(b)** parts of refractive index for composites comprising Batch #4 of the filtered particles from CIP EM, plotted with increasing DC magnetic bias field from 0 mT - 330 mT 147
7.7 Real part of static permeability for each composite formed from the filtered particles plotted as a function of applied DC magnetic bias field strength. 147
7.8 Real **(a)**, and imaginary **(b)** parts of refractive index for composites comprising 30%vol. loading of 800 nm iron particles, plotted with increasing DC magnetic bias field from 0 mT - 330 mT 148
7.9 Real **(a)**, and imaginary **(b)** parts of refractive index for composites comprising 40%vol. loading of 800 nm iron particles, plotted with increasing DC magnetic bias field from 0 mT - 330 mT 148
7.10 Real part of static permeability for each composite formed from the 3rd party 800 nm particles, plotted as a function of applied DC magnetic bias field strength. 149

8.1 Diagram showing a possible improvement to the current air elutriation experiment. A cup would be used to allow a powder to be fed into the system, and the low volume air flow rate will be able to lift the input powder into a dust cloud. . . 155

List of Tables

4.1 Table showing the values for static permittivity, ϵ_s, and relaxation time, τ, that were converged upon when fitting to material S-parameters for $BaTiO_3$ – polyurethane composites. 87

5.1 A table showing the expected mean size and measured mean size for all grades of CIP investigated. The stated size is given by BASF and corresponds to the size below which 50% of the particles fall. The measured size was given by the same definition, and the distribution was inferred from the FWHM of each curve fitted to the measured data. 113

6.1 Table showing the predicted and measured size ranges for particles filtered from a batch of CIP EM. This size range is compared with that measured for a raw, unfiltered batch of CIP EM. d10, d50 and d90 correspond to the diameters below which 10%, 50% and 90% of measured particles fall. 129

6.2 Table showing values for the predicted particle size range of each batch of powder filtered using the 2-bottle elutriation filter. Size distributions were determined by SEM analysis, with error given by the FWHM of a skewed Gaussian curve that has been fitted to the size distribution. 132

6.3 Table showing values for the predicted particle size range of each batch of powder compared with the results for a repeated filtration of CIP EM particles. 133

6.4 Table showing the masses for each sub-grade of CIP EM used in each sample batch with the mass of polyurethane used also. See Table 6.2 for the size ranges of each CIP EM sub-grade and Table 6.3 for the size ranges of sub-grades of CIP EM that were filtered using a repeat of the same experiment. Corresponding volume percentage loadings for each batch of samples are also given. 135

List of Abbreviations

SEM	**S**canning **E**lectron **M**icroscopy
EM	**E**lectro**M**agnetic
CIP	**C**arbonyl **I**ron **P**owder
DC	**D**irect **C**urrent
AC	**A**lternating **C**urrent
S-parameters	**S**cattering-parameters
VNA	**V**ector **N**etwork **A**nalyser
FMR	**F**erro-**M**agnetic **R**esonance
SD	**S**ingle **D**omain
VHF	**V**ery **H**igh **F**requency
UHF	**U**ltra **H**igh **F**requency
FIB	**F**ocused **I**on **B**eam
SOLT	**S**hort **O**pen **L**oad **T**hrough
LRL	**L**ine **R**eflect **L**ine
TEM	**T**ransverse **E**lectric (and) **M**agnetic
DUT	**D**evice **U**nder **T**est
NRW	**N**icholson **R**oss-**W**eir
PTFE	**P**oly**T**etra**F**louro**E**thylene
IPA	**I**so**P**ropyl **A**lcohol
T-matrix	**T**ransfer-matrix
TLD	**T**hrough-**L**ens-**D**etection
JM	**J**ohnson **M**atthey
FWHM	**F**ull **W**idth (at) **H**alf **M**aximum
PU	**P**oly**U**rethane
FEM	**F**inite **E**lement **M**ethod
MSDS	**M**aterials **S**afety **D**ata **S**heet
LPM	**L**itres **P**er **M**inute

Chapter 1

Introduction

1.1 Research Objectives

1.1.1 The Frequency Response of Magnetic Materials

The aim of the work presented in this thesis was to provide an investigation into the relative permittivity and permeability of composite materials comprising small spherical magnetic particles in a dielectric matrix. The results for permittivity and permeability were compared with physical properties of the powders such as average particle size and size distribution, microstructure, or surface coating to ascertain which design factors in the fabrication of spherical magnetic powders can be tuned to give specific electromagnetic (EM) properties that may be carried over to composite materials when mixed into a dielectric matrix.

The utility of this research is to provide insight into materials with non-unity permeability at frequencies higher than the typical low-GHz response of magnetic materials. Such materials would allow high frequency antennas to be miniaturised and impedance matching to free space may be improved [1, 2]. Magnetic composite materials have been investigated extensively in recent years for the purpose of developing improved EM absorbers and antennas. For example, ferrite materials have been of interest due to their high permeability at low radio frequencies [3–6]. The high permeability in ferrites is due to grain boundaries restricting the intra-particle conductivity of the powders, preventing the reduction of permeability due to eddy current losses as well as the crystal structure that causes spin moments in electrons to be preferentially aligned in a specific direction [7]. The high permeability for ferrite composites allows the fabrication of broadband impedance

matched materials in the kHz - MHz regime. Ferromagnetic spherical powders have a significantly lower relative permeability at low frequencies compared with ferrite materials. However, such powders have attracted interest in recent years since Aharoni theorised spherical higher order magnetic absorption modes in 1991 [8]. These modes were theorised to have a $\frac{1}{R^2}$ relationship between the frequency of resonance and the radius of magnetic particle. Later, in 1997, Toneguzzo et al. produced work in confirming the existence of these higher order spherical absorption modes in sub-micron sized ferromagnetic particles, but suggesting that the relationship between resonant frequency and radius was not of the order of $\frac{1}{R^2}$ [9]. The discrepancy in theory and experiment is likely due to the omission of surface anisotropy in Aharoni's original theory [10]. Soon after spherical modes had been theorised in solid ferromagnetic spheres, Aharoni also presented theory for the existence of spherical-shell modes in hollow magnetic spheres [11]. The higher order modes seen in both ferromagnetic solid spheres and spherical shells are believed to be a result of the magnetic domain structure which is most likely a vortex state [12, 13]. The full description of these higher order spherical modes has not yet been attained and an independent research project has been undertaken at the University of Exeter to model these modes explicitly [14].

Carbonyl iron powder has been available commercially for many years and has been of use in powder metallurgy as the micron-sized, 99% pure-iron spheres caused injection moulding to become more viable for small, intricate parts [15–18]. Carbonyl iron powder has been of use in the medical industry for hyperthermic treatment of tumours as well as enhanced drug delivery [19, 20] and as a supplement for treatment of iron deficiency anaemia [21, 22]. The interest in the EM properties of CIP is because these powders are known to have two possible microstructures, depending on the way they have been fabricated. The powder may have a concentric spherical shell structure or polycrystalline solid sphere structure [23], which means investigation into both spherical and spherical-shell modes may well be performed.

1.2 Thesis Outline

Chapters 2 and 3 contain details on the experimental background and experimental methods used throughout the thesis, respectively. Chapters 4, 5, 6 and 7 are experimental chapters containing results for the work done throughout this project, while chapter 9 presents conclusions and the future work that may be performed to extend this work.

1.2.1 The Broadband Frequency Response of Spherical Magnetic Particle – Dielectric Composites

Research into the frequency response of spherical magnetic particle – dielectric composites was extensively performed in the late 1990s with submicron sized monodisperse particles [9, 24, 25]. These results showed the existence of higher order modes above the FMR mode that were dependent on the size of particles. The results were only presented up to maximum frequencies between 10 and 14 GHz so it is possible that other modes exist at even higher frequencies and have not yet been observed. The work presented in chapter 4 demonstrates a technique for characterising materials across the frequency range 100 MHz – 40 GHz, which would be sufficient for investigating higher order modes in spherical magnetic powders that are in the single-micron size regime and below. Chapter 4 presents results for the relative permittivity alone of dielectric composites, and the relative permittivity and permeability for magnetic composites comprised of CIP in polyurethane. The stripline technique presented in this thesis utilises an extra calibration step that has been adapted from [26], as well as an improved geometry for the central conducting line of the stripline which provides better impedance matching than the standard single-angle taper transition seen in previous works [27–29]. The results presented here demonstrate a viable method for the investigation of higher order spherical magnetic modes in composite materials. This technique is valuable for a fast and reliable method of characterising the electromagnetic properties of materials across an unprecedented broadband frequency range without the need for large amounts of material or complex sample geometries.

1.2.2 The Properties of Carbonyl Iron Powder

Chapter 5 presents results for the electromagnetic characterisation of multiple different grades of carbonyl iron powders that were mostly obtained from *BASF*, as well as a second batch acquired from *SS-nano*. Results for the comparisons of different grades of carbonyl iron powders have been compared before but are mostly taken with the assumptions that the specifications provided by the supplier are accurate [30–33]. This work presents the electromagnetic characterisation of different grades of CIP alongside particle size analysis for the grades that was performed in-house by SEM image analysis. Laser diffraction methods for particle size analysis have been performed for obtaining the particle size distribution of CIP grades before [34]. However, it is possible that this analysis technique is misrepresenting the actual size distribution of the CIP grade so results for the laser diffraction method are compared with those produced using the SEM technique [35]. This chapter also presents a comparison of the internal microstructure between individual CIP particles, highlighting that the concentric shell or, 'onion-ring', structure occurs with a varying degree of contrast between domains as well as different spacing of dielectric and magnetic domains for individual particles in the same CIP grade. This result indicates that there is much improvement to be made in the fabrication of carbonyl iron powders if they are to be used for the investigation of spherical magnetic modes and concentric spherical magnetic modes as the dispersion in size as well as structure hinders the ability to make direct comparisons between the physical properties of different carbonyl iron powders and their electromagnetic properties.

1.2.3 The Particle Size Dependence of Higher order Spherical Magnetic Modes

The particles fabricated in [24] were polymetallic ferromagnetic spheres comprising cobalt, nickel and iron. As stated in Section 1.2.1, the particles exhibited higher order modes as the particles were reduced in size, until the smallest particles were shown to exhibit only a single mode that is assumed to be the ferromagnetic resonance mode at an adjusted frequency due to the particles being single domain in nature. Image analysis of the particles was used to give results for the mean particle sizes as 25 nm, 220 nm and 2 μm.

These powders had been fabricated with specific size ranges, so a particle size filtration technique was not required. For the purpose of a particle size investigation into the higher order spherical modes that may be supported in carbonyl iron powders, a filtration technique would be required, or a set of grades of powders directly available in narrow size ranges would be required. It was not possible to fabricate monodisperse particles in-house, so a comparison of different sized carbonyl iron powder grades that were directly available from *BASF* was to be performed. The size dependence of higher order modes specifically in carbonyl iron powders has previously been presented in [33], where the relative permeability for composites containing different sized grades of carbonyl iron powder were compared. This work, however, did not isolate the size of the particles alone, as different carbonyl iron powder grades may well have been fabricated under different conditions, giving a variety of differences possible between grades such as variations in microstructure or composition. Chapter 6 presents a technique for filtering sub-grades of carbonyl iron powders from a master grade that have reduced size distributions and specific mean sizes. This technique is particularly useful for filtration of particles in the single-micron size regime, as this size is too small to easily fabricate sieve meshes for mechanical sifting and too large to be able to exploit diffusive filtration techniques [36]. The elutriation technique presented in Chapter 6 is viable for processing batches of powder on the order of 30 g in mass, giving enough yield from a single experiment to produce composites for testing. Compared with other techniques, this volume of attained filtrate is significant.

1.2.4 The Effect of DC Magnetic Bias Field on Higher order Spherical Magnetic Modes

Chapter 7 presents results for the relative permittivity and permeability of CIP composites as a function of applied DC bias field. Although investigations into the FMR response to external magnetic fields have been performed previously for thin films of magnetic materials using coplanar waveguide (CPW) transmission lines [37, 38], the explicit results for relative permittivity and permeability of bulk composite materials has not yet been presented. Typically measurements of the FMR response to an external magnetic field are presented in terms of a change in measured S-parameters

for the combined transmission line - sample system. Chapter 7 presents results for the de-embedded S-parameters of magnetic composites when subject to an external magnetic DC bias field, from which frequency dependent values for relative permittivity and permeability may be inferred. Little research has been undertaken into the behaviour of higher order spherical magnetic modes when subject to an external field so this work provides a valuable insight into the response of both the FMR and higher order spherical magnetic modes in CIP composites when subject to an external magnetic DC bias field. In this chapter, a strong DC magnetic bias field is shown to suppress the higher order modes in composites, supporting the hypothesis that the vortex domain state is indeed required for supporting the higher order modes seen in spherical magnetic particles.

1.3 Publications, Presentations and Conferences

1.3.1 Peer-Reviewed Publications

- “Exploring Carbon Nanotubes / BaTiO3 / Fe3O4 Nanocomposites as Microwave Absorbers", D. Bychanok, G. Gorokhov, D. Meisak, A. Plyushch, P. Kuzhir, A. Sokal, K. Lapko, A. Sanchez-Sanchez, V. Fierro, A. Celzard, C. Gallagher, A. P. Hibbins, F. Y. Ogrin, C. Brosseau, Progress in Electromagnetics Research C, Vol. 66, pp. 77-85, (2016).

- “Investigating the nature of chiral near-field interactions", L. E. Barr, S. A. R. Horsley, I. R. Hooper, J. K. Eager, C. P. Gallagher, S. M. Hornett, A. P. Hibbins, E. Hendry, Physical Review B, Vol. 97, no. 15, 155418, (2018).

- “A Broadband Stripline Technique for Characterizing Relative Permittivity and Permeability" C. P. Gallagher, N. Cole, P. P. Savage, C. McKeever, J. R. Sambles and A. P. Hibbins, IEEE Transactions on Microwave Theory and Techniques, Vol. 67, no. 1, pp. 231-238, (2018).

1.3.2 Presentations

- “Magnetic Composites: Improved Material Characterisation Techniques for Materials in the Microwave Region", E. A. Burgess, L. Parke, C. P.

Gallagher, S. A. R. Horsley, C. McKeever, A. P. Hibbins and J. R. Sambles, Presented to the Research Institude for Nuclear Problems Belarusian State University, during collaboration, (2016).

- “Stripline Measurements of Spherical Iron - Polyurethane Composites" C. P. Gallagher, C. McKeever, A. P. Hibbins, J. R. Sambles, F. Y. Ogrin and M. Aziz, Presented at IET Novel RF Materials and Manufacturing Techniques for Antennas conference, (2018).

- Several presentations have been given to industry, detailling the works undertaken throughout this project.

1.3.3 Poster Presentations

- “The Broadband Extraction of Relative Permittivity and Permeability for Dielectric and Magnetic Composites", C. P. Gallagher, A. P. Hibbins and J. R. Sambles, Presented at Cranfield Defence Symposium (2017)

- “Particle Size Filtration and High GHz Characterisation of Spherical Iron nano-powder – Polyurethane Composites", C. P. Gallagher, A. P. Hibbins and J. R. Sambles, Presented at IEEE International Conference on Microwave Magnetics, (2018).

1.3.4 Collaborations/ Industry Contributions

- Collaboration with Research Institude for Nuclear Problems Belarusian State University,

- Several stripline devices have been manufactured for industrial use.

Chapter 2

Background

2.1 Introduction

This section will cover general magnetics background as well as outlining the theory involved in this project, examining the extraction of the electromagnetic (EM) properties of magnetic composites by use of scattering parameters (S-parameters) measured with a vector network analyser (VNA). From these S-parameters, values for relative permittivity and permeability may be obtained. Various transmission lines that are already used for this method will be discussed alongside two methods by which the extraction of EM parameters from S-parameters may be deduced.

2.2 Permeability

The magnetic permeability, μ, of a material is representative of its response when subject to a magnetic field. The permeability relates the induced magnetic field, B, to an external field, H. In magnetic materials, there is another contribution to the induced magnetic field that is due to the magnetisation of the material, M, this is also dependent upon the applied field. The induced magnetic field is given in terms of the susceptibility by Equation (2.1) [39]

$$\mathbf{B} = \mu_0(\mathbf{H} + \mathbf{M}) = \mu_0(1 + \chi)\mathbf{H}. \tag{2.1}$$

Here μ, the permeability, is given by the product of the relative permeability, μ_r, and the permeability of free space, $\mu_0 = 4\pi \times 10^{-7}$ NA^{-2}. The static, DC value of χ may be extracted from hysteresis loops, discussed in section 2.3.6. This induced magnetic field is caused by the alignment of spin

moments in the material, the combined effect of which causes an enhancement of the applied magnetic field. The number of spins aligned as well as the extent to which they have been aligned to this field will correlate with the resultant measured induction.

2.3 Magnetism

Magnetism is a property of materials that arises from the magnetic moment produced primarily by the electrons in a material. By considering the surface charge of a spinning electron, a current loop is seen to exist that will produce a magnetic moment that is pointing up or down, depending on the direction of the spin of the electron. One must consider not only the angular spin moment of the electron but also the orbital angular momentum of the electron that will contribute again to the magnetic moment of a single atom. The interaction of the many spin moments in a material gives rise to the overall magnetisation, as the spins may be oriented such that the magnetic moments enhance or compensate for each other, giving a net magnetisation. The way in which these spins interact and align defines the type of magnetism that the material possesses. Different types of magnetism are discussed in this section.

2.3.1 Diamagnetism

All electron orbital shells in constituent diamagnetic atoms, such as Helium, are filled so there are no unpaired electrons to contribute a magnetisation. When subjected to a magnetic field, a negative magnetisation is produced. Diamagnetic materials have a value for susceptibility that is small and negative [40]. When the applied magnetic field is reduced to zero, this negative magnetisation also goes to zero. This negative and small susceptibility leads to materials that have a relative permeability less than one.

2.3.2 Paramagnetism

Paramagnetic materials have electron orbital shells that are unfilled, allowing for a net magnetisation to be produced. However, thermal effects mean that the magnetic moments arising from these unpaired electrons are randomly oriented, resulting in a net magnetisation of zero in zero field. When

subject to a magnetic field, these orbitals are partially aligned with the field and produce a net magnetisation that is in the direction of the applied field and proportional to it. The exchange interaction between magnetic moments in paramagnetic materials is very weak, so thermal randomising of the moments can dominate [41]. This means the susceptibility of paramagnetic materials is heavily temperature dependent, with net magnetic moment being lower at higher values of T. This relationship between susceptibility and temperature is known as the Curie Law and will be discussed in the next subsection.

2.3.3 Ferromagnetism

Ferromagnetic materials have atoms with unfilled orbitals, again resulting in a net magnetic moment when subject to a magnetic field. However, the spins are also able to interact with each other, causing them to be aligned even without the presence of a magnetic field - this gives ferromagnetic materials a net magnetic moment at zero applied field. This net magnetisation in the absence of an applied field is referred to as the remament magnetisation, which will be discussed in section 2.3.6. The interaction between electrons in ferromagnetic materials is referred to as the exchange interaction, which is a quantum mechanical process that causes the spins of neighbouring electrons to be either aligned or anti-aligned, depending upon the value of the exchange energy. Exchange energy is to be discussed further in section 2.3.8. Similarly to paramagnetic materials, the magnetic moments in ferromagnetic materials are perturbed by randomising thermal effects which results in a reduction of the net magnetisation with increased temperature. There is a maximum temperature at which the magnetisation of a magnetic material will become zero. This temperature is referred to as the Curie Temperature [42].

2.3.4 Antiferromagnetism

Antiferromagnets again have atoms with unfilled electron orbitals but the exchange interaction between electrons in neighboring atoms is such that electrons in neighboring atoms will have moments that are anti-aligned. The anti-alignment of magnetic moments is usually a result of superexchange interactions, where an intermediate non-magnetic atom site causes

an interaction to result in the next magnetic site to be anti-aligned [41, 43]. This results in an ordered structure of spins that will give a full compensation of magnetic moments, leading to a net magnetisation of zero and a remanent magnetisation of zero also. It is possible, however, for spins in the atoms not to be aligned completely parallel and to be canted. This results in a small net magnetisation that is referred to as canted antiferromagnetism.

2.3.5 Ferrimagnetism

Ferrimagnetic materials have two sources of magnetic moment, typically at different atomic sites. The two sources of magnetic moments are typically the result of two positively charged metal ions that are different separated by negatively charged divalent oxygen ions [7]. The oxygen ions provide the superexchange interaction that causes the two sources of magnetic moments, as in antiferromagnetic materials, to be opposing. However, the two sources of moments have different magnitudes, so a net magnetisation remains that is smaller than in ferromagnetic materials. Ferrite materials were examined extensively in a previous work at Exeter University, investigating the complex permittivity and permeability for Mn-Zn ferrites and Ni-Zn ferrites [2, 4]. Work was also performed to investigate the particle size dependence of these properties for ferrite materials but is yet to be published.

2.3.6 Hysteresis

Hysteresis is a phenomenon that occurs in magnetic materials that is due to the fact that ferromagnetic materials possess subregions of spins that are all aligned with each other, named domains. Depending on the size of the magnetic material, there may be many domains that are oriented in different directions, depending on the crystal grain orientation and the grain size. The theory of domains will be discussed later in section 2.3.7. The existence of domains in a material causes ferromagnets not to always exist in a constant state of saturation, where all magnetic moments are completely aligned in one direction, giving maximum magnetisation, but rather to have a net magnetisation that is the sum of all domain contributions. As a field is applied, domain walls, discussed in section 2.3.7, will shift such that domains oriented in the direction of the applied field will grow and those opposing the direction of the field will shrink. This produces an increase in

the magnetisation. At high enough fields, domains begin to merge together, until a single domain exists that is then finally re-oriented in the direction of the field which results in saturation and a maximum magnetisation. Hysteresis loops for magnetic materials are produced in order to characterise their magnetic properties by increasing an applied field from zero to the saturation field, H_s and then reducing this field down to zero and applying a field in the opposite direction until again saturation is reached. This allows one to establish if a magnetic material, after saturation and reduction of the field to zero, will have a magnetisation that exists in the absence of a field. The magnetisation that exists after this process is named the remanent magnetisation, M_r. In order to reduce this remanent magnetisation back to zero, an opposing field must be applied and is referred to as the coercive field, H_c Figure 2.1 [39, 44].

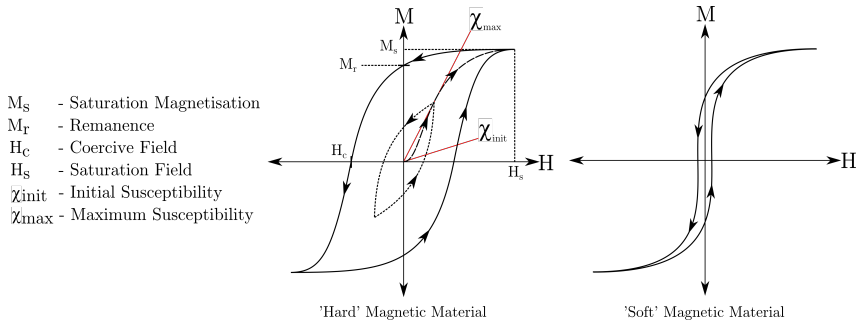

Figure 2.1: Hysteresis curves for hard and soft magnetic materials where the initial and maximum susceptibilities are given by the gradient of the virgin curve at low and high magnetic fields, respectively, shown by the red lines. The width or area of a hysteresis loop is representative of the materials magnetic loss associated with the force required to rotate magnetic moments

Magnetic materials with a high coercive field and remanent magnetisation are referred to as hard magnetic materials, with a wide hysteresis loop, and those with a low remanent magnetisation and coercive field are soft magnetic materials. The total area of the hysteresis loop is representative of the losses associated with domain wall motion in magnetic materials.

2.3.7 Magnetic Domains

Not all of the magnetic moments of the electrons in a material will be aligned in the direction of an applied magnetic field. Grain boundaries and the crystalline anisotropy of a material will also influence the orientation. The moments of spins in a material are actually split into domains in which each of the spins will be aligned. In different domains, the moments are aligned in different directions that are prefferential, dependent upon the microstructure of the material. This is shown in Figure 2.2 where each of the arrows represent the orientation of spins within each domain. Magnetic domains exist in order to reduce the magnetostatic energy of the stray fields around the outside of the material [39]. By splitting the moments of a material into domains this stray field emanating out from the material is able to be more closely confined to the surface of the material, lowering the overall energy of the system, providing the energy cost of creating the domain walls is lower than the reduction in magnetostatic energy. The energy cost of creating domain walls is discussed in the next section.

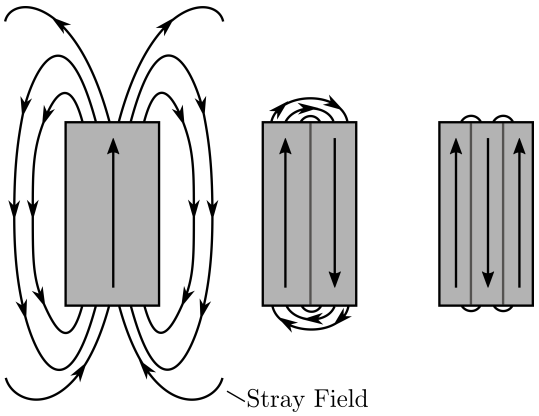

Figure 2.2: This figure shows the reduction in stray field when splitting a simple geometry magnetic material into domains. As can be seen, the stray field around the material is reduced and confined closer to the surface when more domains are added. This lowers the magnetostatic energy of the system but eventually the cost of adding domain walls will outweigh the reduction in magnetostatic energy, at which point a stable domain structure is formed.

When a magnetic field is applied to the material, domains that have moments aligned parallel to the field will grow while those opposing the field will shrink until one single domain exists. At this point, the moments in this single domain will be rotated until saturation is reached where the magnetic moments of the electrons are rotated to be entirely parallel with the applied field as in Figure 2.3 [45].

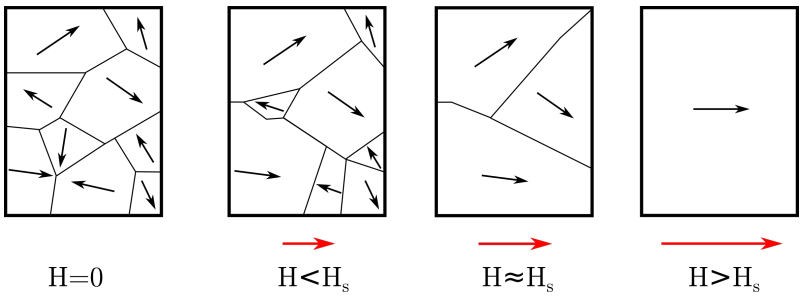

Figure 2.3: This figure demonstrates the motion of domain walls in the presence of an applied magnetic field. As the external field is increased in strength, domains with components pointing in the direction of field increase in size, while those opposing the field shrink. Once domains only exist that are pointing in the direction of the field, a final domain is formed that, upon saturation, is completely aligned with the applied field. The field at which saturation occurs is referred to as the saturation magnetisation, H_S.

Domain Walls

Domain walls exist between adjacent domains whereby the magnetic moments gradually rotate to the new orientation of the adjacent domain. This transition is shown in Figure 2.7, and the thickness of these domain walls is governed by the magnetocrystalline anisotropy of the material, and the exchange energy of the material. A thicker domain wall will have a higher cost in energy from the magnetocrystalline anisotropy, which acts to align moments along axes of magnetisation that are dependent upon the crystalline structure of the material, and a narrower domain wall will have a higher cost in energy due to the exchange energy, which acts to orient magnetic moments parallel to their neighbours [46]. This section will discuss the nature of the mechanisms that affect the creation of domain walls, namely the exchange force, magnetocrystalline anisotropy and the surface anisotropy.

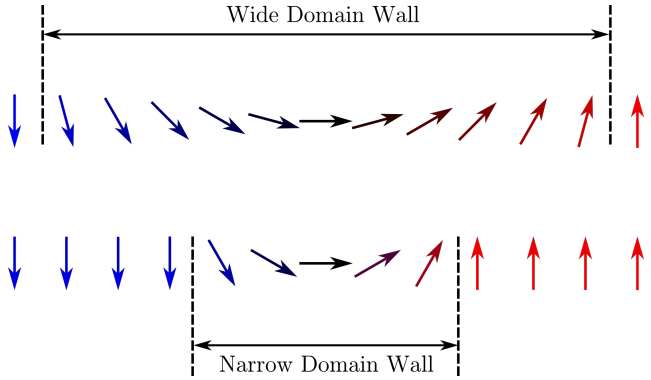

Figure 2.4: This figure shows the magnetic moments across domain walls that are narrow and wide. The rotation in magnetic moments across the sample will have a width that is dependent upon the magnetocrystalline and exchange energies. This rotation of magnetic moments through 180° can occur in the plane of magnetisation, as in Néel walls, or out of the plane of magnetisation as in Bloch walls.

2.3.8 Exchange Energy

The exchange energy is a phenomenon arising from the quantum nature of electrons, which imposes the constraint that electrons in the same space may not possess the same quantum properties. This means that electrons in the same spatial quantum state will have spins that are antiparallel if they are confined to the same space, or it causes orbitals of the electrons to be modified due to the crystal structure. If the exchange energy is negative, it will prove energetically favorable for the electrons to be antiparallel, and if positive the electrons will be parallel. This affects the size of domain wall transition regions as a wide domain wall, as shown in Figure 2.7, will have a smaller contribution to the domain wall energy than a narrow domain wall due to the fact that neighbouring electrons will differ less in alignment. This also enforces electrons to fill orbital shells in a specific order, as Pauli principle will not allow electrons of the same spin to occupy the same orbital, meaning it will be situated in the next neighboring site [43].

2.3.9 Magnetocrystalline Anisotropy

Magnetocrystalline anisotropy arises from the crystal structure of magnetic materials. The crystal lattice of a material will cause electron orbitals to interact differently in different directions, meaning that it will be easier for magnetisation to occur along one axis than another. For example, in bcc

iron there exists an easy, medium and hard axis corresponding respectively to the <1 0 0>, <1 1 0> and <1 1 1> directions in the crystal lattice Figure 2.5b [47]. The typical magnetisation curves for body centered cubic (bcc) iron in different axes of magnetisation, alongside its crystalline structure, are shown in Figure 2.5a. The magnetocrystalline energy is given by the energy required to rotate magnetic domains from the easy axis to the hard axis and acts to reduce the width of domain walls. This is because if a wide domain wall exists, more moments will be aligned along an axis of difficult magnetisation, leading to a higher value for saturation field as opposed to the case concerning narrow domain walls where fewer moments will be aligned along an axis that does not align with the crystal lattice.

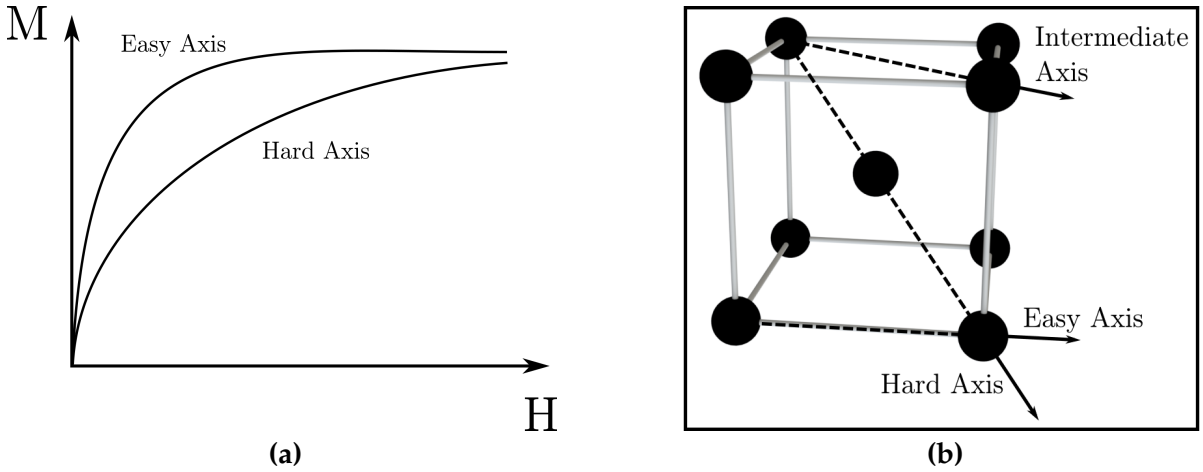

Figure 2.5: Diagrams showing **(a)** the typical magnetisation curve for a magnetic material along the easy and hard axes of magnetisation and **(b)** The crystal structure of bcc iron, showing easy, intermediate and hard axes of magnetisation. *Replicated from Magnetic Materials: Fundamentals and Applications[47].*

2.4 The Demagnetising Field

As well as a stray field outside of magnetic materials, there is a magnetic field that exists inside them. The field inside magnetic materials is referred to as the demagnetising field, and acts in a direction that opposes the magnetisation of the material. Figures showing the B-field and H-field lines for an anisotropic sample that has been magnetised along the long axis is shown in Figure 2.6. By integrating around a closed loop containing the material, and applying Stokes' theorem to the H field along this loop, one may infer that the magnetic field inside this material opposes the stray field outside the material. This is because there are no currents flowing through this material, and by Ampere's law Equation (2.2)

$$\mathbf{j} = \nabla \times \mathbf{H} = \oint H \cdot dl = 0. \tag{2.2}$$

The demagnetising field is heavily dependent on the shape of the material, and causes preferrential magnetisation based on shape. This type of anisotropy is referred to as shape anisotropy, and it may be considered to act as an "effective" external field, that stresses magnetic moments along a preferrential axis. The shape anisotropy is usually neglected for bulk materials, as the shape anisotropy term is not a dominant factor unless the skin depth of the material is comparable to the material's size [48].

2.4.1 Skin Depth

The skin depth of a material is the distance through a conducting material that an electromagnetic wave can permeate before being reduced to a negligible amplitude. The skin depth arises due to surface charges in metal circulating under the effect of the indicent electromagnetic wave, and generating a current loop that induces an opposing magnetic field. As the frequency of incident wave increases, the skin depth is reduced, and as the conduction of the material increases, the skin depth decreases [49].

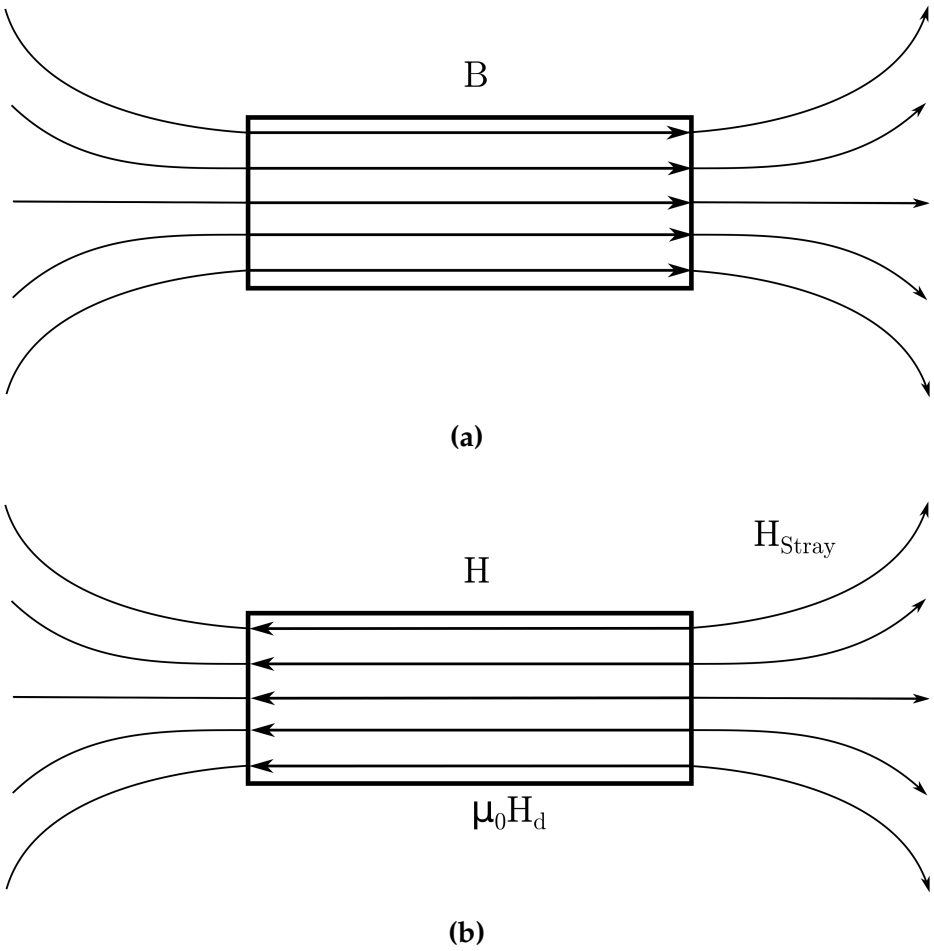

Figure 2.6: Schematics showing the B-Field lines, **(a)**, and induced H-field lines, **(b)**, for an anisotropic magnetic material, magnetised along the long axis. The H-field outside of the material is the stray field, H_{Stray}, while the H-field inside the material is named the demagnetising field, H_d.

2.5 The Microwave Frequency Response of Magnetic Materials

The complex magnetic permeability of a material has a frequency dependence that is a result of the time dependent response of magnetic moments. The magnetic moments in a particle are perturbed by the torque produced by an external driving field. This torque pulls the magnetic moment from its preferred orientation and if the field is removed, the moment of the particle will precess around its preferred orientation for some time and gradually relax back into the original orientation. The frequency of this precession is related to the strength of the applied field, and the gyromagnetic ratio

of the particles. The gyromagnetic ratio contains information on the mass, intrinsic magnetic moment and angular moment of the particles, which is influenced by many of the factors described previously [48, 50, 51].

Because of this time-dependent precession, there is a frequency dependence of the magnetic permeability for materials. When the frequency of an AC driving field matches the precessional frequency of the particles in a material, there is a peak in magnetic absorption. This peak in magnetic absorption is often referred to as the ferromagnetic resonance (FMR) or fundamental mode of a material. In the absence of an external magnetic DC biasing field, the restoring force for the precession of a particle's magnetic moment is dependent on the magnetisation of the particle, which is a result of magnetocrystalline anisotropy, shape anisotropy and domain boundary contributions. The typical frequency of FMR for ferromagnetic materials is between 1 and 5 GHz.

There are other contributions to the absorption response at lower GHz frequencies for these materials, such as domain wall motion and spin components [30, 52]. Eddy current losses also add a frequency dependent loss term to magnetic materials that are conducting. The AC field creates current loops in conducting regions that induce a magnetic field that opposes the magnetic field in the bulk. This eddy current loss term is frequency dependent as the magnitude of the induced current loop is dependent upon the rate of change of the oscillating field. As frequency of driving field increases, the eddy current losses do so too [7].

2.5.1 Snoek's Law

Ferromagnetic materials will possess a complex permeability that has a real value above unity at DC frequencies. As the frequency of driving field is increased, the motion of domain walls becomes too slow to fully rotate during one AC cycle, and the real part of permeability begins to decrease. There is a point at which the domain walls are unable to move quickly enough to give any magnetic response, and the permeability approaches 1. The lagging of domain wall motion as driving frequency is increased is a macroscopic view of the FMR and is the primary source of the frequency dependent absorption in magnetic materials. The position in frequency at which the permeability approaches unity is dependent upon the gyromagnetic ratio and magnetisation of the material. These factors also determine the initial DC

permeability of the material, and there is a resultant correlation between the initial permeability and the frequency of FMR such that the higher the initial permeability, the lower the frequency at which this resonance occurs [53]. This relationship means that there is some limit to how high the frequency response of magnetic permeability may reach when only considering FMR. This limit has been pushed to its limits using materials that have high anisotropy terms, for example in thin films with high shape anisotropy or hexaferrite materials that have a high magnetocrystalline anisotropy [54, 55].

2.6 Ferromagnetic Resonance in Thin Films

The magnetization dynamics of thin ferromagnetic films has become of interest in recent years, and extensive research has been performed on these materials. The magnetic response of thin ferromagnetic films is discussed here as there may be analogies made between the effects seen in these materials and those seen in magnetic powders. A systematic study into the magnetisation dynamics of thin films was not the scope of this project, so is only described as an aid to upcoming explanations.

The frequency at which FMR occurs for materials can be affected by factors other than the intrinsic magnetic properties. For example, thin films of ferromagnetic material will have shape anisotropy such that the magnetic moments in the material will prefer to be aligned along the surface [56]. This preferential alignment of the magnetic moments acts similarly to an applied DC magnetic field. The surface boundary stesses the moments of particles to be in the plane of the film. This effect may be utilised in magnetic powders by ball milling the powders such that they form thin flakes of magnetic material. The thin film effect of straining the magnetic moments in the plane of the flakes allows materials to possess permeabilities at higher frequencies than expected for iron, a result that appears to break Snoek's limit [57]. By choosing the thickness of magnetic films, one can change the internal strain on the magnetic moments, giving a different position in frequency for the FMR mode [58] based on thickness. This ability to tune shape anisotropy terms for increasing the frequency of FMR has also been utilised in nanorods, to achieve FMR absorption modes at frequencies as high as 30 GHz for arrays of Co nanowires, or 10 GHz with Ni nanowires [59].

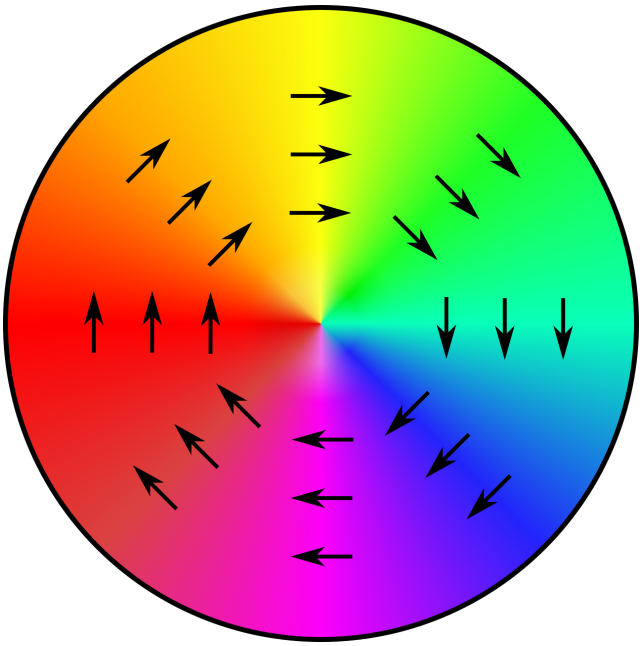

Figure 2.7: Schematic showing the magnetic moments in a circular thin film with vortex domain state. magnetic moments circulate in the plane of the thin film, with a singularity at the centre that has a magnetic moment pointing out of the plane.

The lowest energy domain state for finite thin ferromagnetic films is the vortex domain, where magnetic domains circulate in plane with the film. This vortex structure possesses a singularity at the centre, where the magnetic moments are forced to point out of the plane of the film. Application of an AC electromagnetic field causes this vortex singularity to gyrate around the central point, in a simiar way to the magnetic precession of magnetic moments in single particles. In circular thin films of ferromagnetic material, higher order gyration modes have been observed that are associated with the gyration of this vortex structure [60]. These higher order modes, named vortex flexure modes or vortex gyrotropic modes, have multiple eigenstates at higher frequencies, meaning for specific geometries there is access to magnetic absorptions other than the FMR at higher frequencies. The domain structure of spherical magnetic particles, as well as spherical magnetic shells, is expected to be a vortex also [61]. The moments in these spherical particles circulate around the central axis of the particles and singularities exist at the poles where the moments point in a direction that is normal to the surface at this singularity.

2.7 Spherical Magnetic Particles

Spherical magnetic particles possess higher order magnetic resonances at frequencies above the fundamental mode [9, 30, 33, 62]. These resonances are thought to be a result of the vortex domain structure of spherical particles. The size dependence of these spherical modes is demonstrated in [24, 63]. The frequency of these modes is strongly dependent on particle size. Smaller magnetic particles exhibit resonances at higher frequencies than large particles, until the particles are reduced to the size that they become too small to support a vortex structure, and are only single domain (SD). These single domain particles tend to exhibit only a single mode, indicating that the vortex domain structure is essential for supporting higher order magnetic modes [24, 25].

2.7.1 Spherical Shell Particles

As well as particle size, spherical shell particles have the added variable of magnetic shell thickness. The effect that the thickness of the shell has is similar to that seen in magnetic thin films. By decreasing the shell thickness, it is possible to change the shape anisotropy in the particles as well as the surface anisotropy [10]. This gives a second controllable parameter when examining the fabrication of particles with specific properties. The added shape anisotropy from magnetic spherical shells is thought to enhance spherical magnetic modes and allow even higher order modes to be supported, at frequencies as high as 40 GHz (This is the result of research at University of Exeter that has not yet been published [14]). It is also thought that by reducing the amount of conducting material in the particles, magnetic loss effects such as eddy current losses are reduced, so higher permeabilities may be achieved. By creating particles with a concentric shell structure, the amount of magnetic material may be preserved whilst removing the amount of eddy current losses that can result from a fully connected sphere. It is also necessary to consider the coupling effects between concentric shells of magnetic material. Concentric rings of magnetic films have been investigated and are shown to couple, such that new modes may exist [64]. As well as incorporating new modes, the introduction of concentric shells to particles could well allow electromagnetic waves to permeate deeper into particles. Reducing the concentric shells to be a thickness significantly smaller than the

skin depth means the electromagnetic wave in the spheres will have less reduction due to eddy currents but will also mean that the incident electromagnetic wave may be able to permeate further into the particles. The electromagnetic wave passing further into particles means that more of the magnetic material in the sphere will be 'of use' for increasing the permeability of a magnetic composite.

2.7.2 Single Domain Particles & Superparamagnetism

As magnetic particles become smaller, the number of domains in the particle will decrease. This is because the number of domains in a magnetic particle is governed by the cost in energy for creating a domain wall compared with the magnetostatic energy reduction associated with confining the stray field. As particles become smaller, there is a point at which a particle will become single domain (SD) [65, 66]. At this point, a single fully saturated domain in the particle will exist. It is more difficult to rotate all of the moments in a fully saturated particle than it is to shift domain walls. This means that although a higher saturation magnetisation may be achieved for SD particles, the coercive field is higher so a stronger external magnetic field is required to change the magnetisation.

As particles are reduced in size below the threshold for SD particles, the effects of magnetocrystalline energy are also reduced. This can lead to another phenomenon named superparamagnetism where the surface anisotropy and thermal energy can overcome the magnetocrystalline energy, leading to magnetic properties indicative of a paramagnetic material. Superparamagnetic materials have moments that are randomly oriented due to thermal fluctuations but are still interacting to align each other to an extent. This means that when a field is applied, superparamagnetic materials behave as ferromagnets, but with no remanent magnetisation when the field is reduced again to zero [67]. The lack of remanent magnetisation and low switching field for these particles make them ideal for use as functionalised powders in medical applications as they are less prone to agglomeration after removal of an external field but still have a strong response to external fields [68–70].

2.8 Magnetic Composites

By combining metallic magnetic powders with dielectrics to form composites, it has been observed that the magnetic response of materials can be extended higher in frequency compared with bulk materials. This is because the metallic regions are reduced in size, minimising the effects of eddy currents and also due to the fact that metallic regions will have a boundary between particles, again reducing the effective size of particles and minimising eddy currents further. Metallic regions within individual particles may be reduced even further by the incorporation of a microstructure that separates metallic regions from one another with another incorporation of a dielectric layer. Carbonyl iron powder (CIP) is an example of a material that has isolation of metallic regions due to its "onion ring" structure, comprising of alternating layers of iron and an insulating carbide layer. These particles are available with two different microstructures, the aforementioned onion ring structure, and a polycrystalline structure. These two available structures mean it should be possible to make an investigation into both solid spherical magnetic particles and concentric spherical shell particles. The results of investigations into these structures are discussed further in Chapter 5.

Magnetic composites are already being used for antenna applications typically utilising the high permeability of ferrite composites [71–73]. These materials are often for VHF/UHF applications, across the approximate frequency range 150 – 800 MHz as this is where the permeability of the materials is high, being around 6 and above while the magnetic loss is low, with magnetic loss tangents as low as 0.05 [74]. The interest in these magnetodielectric materials has increased since it was reported that the inclusion of permeability into materials not only improves the impedance matching of an antenna, as previously stated before, but also because the bandwidth of artificial magnetic conductors for antenna groundplanes may be increased by adding a permeability to the substrate [1, 75–77]. Although this inclusion of magnetic material allows more broadband antennas to be manufactured with even lower profiles, this often comes with the cost of mass as the magnetodielectric material is signifcantly more dense than most foam fillers for antennas [78].

Ferrite materials have typically been used for antenna applications as their permeability is high in the frequency range of interest. It is necessary

to use materials that also have a low magnetic loss in these regions, so pushing the frequency of primary absorption is necessary such that permeability is constant, and the loss is low is desirable. For magnetic absorbers, it is also necessary to have a material with a high permeability that has a value close to the relative permittivity. If the relative permittivity and permeability are close to eachother, the characteristic impedance of the material will be close to that of air, so little of the incident wave is reflected. Improving the impedance matching of a material to free space allows the fabrication of panels with low reflection that will be ideal for absorber applications. It is also a requirement that the magnetic loss be significant and broadband across the frequency range of interest for the absorber to be efficient and low-profile.

Carbonyl iron powders, with multiple absorption modes that tend to merge and leave a broadband absorption are typically used for absorber applications [79, 80]. Greater underdstanding of the ways in which carbonyl iron powder may be manipulated to give lower loss at UHF/VHF frequencies, or how to tune the broadband absorption of EM radiation in the GHz regime will be invaluable for the development of both antenna devices and absorber materials.

2.8.1 Carbonyl Iron Powder

Carbonyl iron powder, first produced by BASF in 1925, is a powder comprising of spherical particles with diameters in the range of 1 - 10 μm. They are formed from the condensation of gaseous compounds at high temperatures and have a % purity of iron above 97%. Different grades available from BASF will have differing values of average particle size, % composition of iron, a microstructure of either polycystalline or 'onion skin' structure; depending on whether or not the powder was sintered after production, and may also have a phosphate coating [81, 82]. CIP was originally created as a material for use in powder metallurgy as its high iron content and small particle size made it an ideal substance for use in metal injection moulding. In recent years, interest in the EM properties of these particles has arisen due to resonances that may be attributed to the alternating layers of magnetic material in the onion structure. The alternating structure adds a constraint to domain formation, and CIPs are able to be produced with small mean

particle sizes. Both of these effects are thought to contribute to the higher order resonances seen [30].

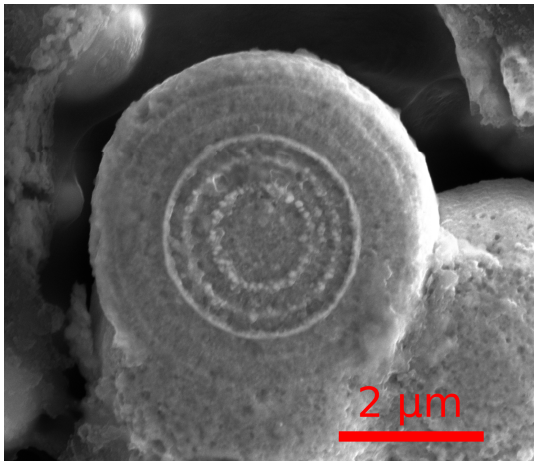

Figure 2.8: SEM micrograph showing an example section of CIP, indicating the onionlike microstructure of "hard" grade powders. The lighter boundaries of the structure are the iron carbide, whilst the darker regions are iron rich regions. *Image taken at University of Exeter*

By forming composites of carbonyl iron powder at different volume fillings, it is possible to create materials with tailored values of permittivity and permeability. A deeper understanding into the mechanisms governing the response of these particles will allow the creation of not only tailored composites based on volume loadings of material, but tailored fillers for producing particles with tuned absorption modes.

Production of Carbonyl Iron Powder

Carbonyl iron powder is formed from the thermal decomposition of gaseous iron pentacarbonyl into spheres of iron-α. This process releases carbon monoxide which, in the enclosed production environment will become in excess. The excess CO allows another reaction to become favorable that produces free carbon [83]. This free carbon is then the reagent in further reactions which result in a carbide layer forming on the iron core. These two sets of reactions go on throughout the process of formation to cause alternating layers of pure iron and iron carbide to be deposited, resulting in spherical particles that possess an "onion ring" structure, with layers of iron separated by insulating layers of iron carbide Figure 2.8 [18].

$$\mathrm{Fe(CO)_5} \longrightarrow \mathrm{Fe} + 5\,\mathrm{CO} \tag{2.3}$$

$$2\,CO \longrightarrow C + CO_2 \tag{2.4}$$

Properties of CIP

Composites formed from CIP require investigation not only into the effect of different volume fractions of particle loadings in composites but also into the microstructure of the particles themselves in order to gain a full understanding of how the size of the particles, number of layers and thickness of alternating layers correlates to the above-unity values for permeability at high frequencies. This will require use of the scanning electron microscope (SEM) to image cross-sections of particles as well as use of a vector network analyser (VNA) connected to an appropriate transmission line for extraction of scattering parameters from which values of relative permittivity and permeability may be inferred. The details of methods for these investigations are to be provided in this text alongside a review of literature available that has presented research into these materials.

2.9 The Scanning Electron Microscope and Focused Ion Beam

2.9.1 Scanning Electron Microscope

Scanning electron microscopy involves the use of a scanning electron microscope (SEM) to image features that would otherwise be too small to observe via optical microscopy. This is achieved by accelerating electrons towards an object. The beam of electrons is rastered along the imaging surface, and the incident electrons excite secondary electrons that are emitted from the surface or just below the surface of the sample. The secondary electrons are detected by an electron collector, and depending on the average energy that the electrons possess at that position, a contrast is allocated to a corresponding pixel on the image.

The mechanisms for providing contrast on an imaging surface are conductivity and topological contrast. The conductivity of the sample affects the contrast of SEM image such that a high conductivity will give a high contrast. The topological contrast is simply associated with the direction in which electrons will be preferentially scattered due to the shape of the imaging surface. At the edge of surfaces, more secondary electrons are able

to escape from the surface, and a higher contrast will be found at these regions of the image.

2.9.2 Focused Ion Beam

A focused ion beam (FIB) works in a similar way to an SEM with ions rather than electrons accelerated towards an object. The ions used in a FIB are typically Ga^+ ions, and since they are significantly more massive than electrons, the focused beam may be used to mill materials. It is also possible to use the FIB for imaging, but the more massive particles will damage the object at a faster rate than an electron beam will, as used in SEM imaging.

SEM and FIB systems are typically combined into a dualbeam system as they synergise well for simultaneously imaging surfaces whilst milling microstructures into them. The dualbeam system used for this project was a *FEI Nova NanoLab 600 DualBeam*.

2.10 The Vector Network Analyser

A vector network analyser (VNA) is a piece of equipment used for investigating the reflection and transmission of electrical devices as a function of frequency. The systems used for this project were the *Anritsu MS4647A* 70 KHz - 70 GHz and *Anritsu MS4644A* 40 MHz - 40 GHz vector network analysers. These systems are comprised of two sources and detectors, at each of the ports 1 and 2. there is a signal generator that produces an AC electromagnetic signal at either of the two ports, at which point the reflected and transmitted parts of the wave are measured, and named as scattering parameters (S-parameters). The subscript of the S-parameter details where the signal was sent from and measured at. For example, S_{11} refers to the wave sent from port 1, measured again at port 1 (reflection). The parameter S_{12} corresponds to a signal sent from port 2, arriving at port 1 (transmission). S-parameters will be discussed in further detail in the following section.

2.10.1 VNA Calibration

In order to take measurements with the VNA that are respresentative of the system under investigation, a calibration must be performed that removes the effects of the internal reflections in the VNA. The calibration also

accounts for the reflections at the connections to the coaxial cables, effectively setting the boundaries of the measurement system to start at the ports of the coaxial cables connected to the VNA. These edge boundaries on the measurement system are referred to as the reference planes, as they are the reference positions used for calculating the phase change associated with wave propagation across the system.

The typical calibration for waveguide or coaxial lines is a SOLT calibration. This involves using measurements of a 'short', 'open', 'load' and 'through' calibration standard attached to each coaxial cable at the ports. These measurements are used to infer the internal reflections, losses and interferences in the VNA. Other calibration methods exist, for example using a sliding load, line-reflect-line (LRL) or triple short method [84]. Each calibration technique provides information on the phase change, as well as reflection loss and transmission characteristics for the transition region from signal generation to region of interest.

For the VNA measurements in this project, a preliminary SOLT calibration was used for coaxial line calibration before applying a second calibration to measurements that is described in Chapter 4.

2.11 Transmission Line Techniques

Here, to electromagnetically characterise a material, the values for ϵ_r and μ_r are deduced. Methods for doing this using a vector network analyser (VNA) involve the utilisation of a transmission line to house the material under test. A transmission line is a conducting line that typically supports a transverse electric and magnetic (TEM) electromagnetic wave. Using this, a wave incident on a sample will have its reflected and transmitted parts recorded. These reflected and transmitted signals are referred to as scattering aprameters (S-parameters), and can be used to infer values for the complex permittivity and permeability of the sample. The extraction of permittivity and permeability from these measurements is discussed later in this section. To ensure that the scattering parameters of the sample alone are recorded, reflections at the device-coaxial line interface must be minimised. This is achieved by matching both the impedances of the lines as well as by matching the incident field with the field supported by the device. Impedance matching is achieved by incorporating an appropriate transition

region from coaxial line to device that allows a gradual change in field shape from that supported in a coaxial line to that which is supported in the device under test (DUT).

Coaxial Transmission Line

A coaxial transmission line is the standard form for transmission of EM waves between most devices. It consists of a cylindrical center conductor, separated from an outer conductor by a dielectric. The inner and outer radii of the cylinders together with the relative permittivity, ϵ_r, and permeability, μ_r of the filler dictate the characteristic impedance of the line, given by Equation (2.5)[85]

$$Z_0 = \sqrt{\frac{\mu}{4\pi^2\epsilon}} \ln \frac{R}{r}. \tag{2.5}$$

Here, R and r are the radii for the outer and inner conductors, respectively. A TEM mode is supported with the electric field being radial from the center conductor to the outer conductor. The magnetic field circulates around the cylinder Figure 2.9.

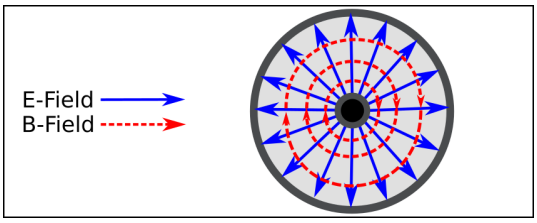

Figure 2.9: Diagram showing the electric and magnetic field lines in a coaxial transmission line.

These transmission lines are somewhat broadband, with most commercially available configurations supporting a TEM mode across the frequency range of 2 - 18 GHz[31, 86, 87]. However,using coaxial lines to electromagnetically characterise a sample has a problem associated with the fabrication of cylindrical toroid samples that are metalised along the surface of the hole accomodating the center conductor. Samples possessing this geometry also present a problem with regarding air gaps between the conductors and sample edges. Recently there has been work demonstrating the ability to compensate for these air gaps by considering the capacitive effects of the system with air gaps [88]. Despite these recent improvements to the coaxial

technique, a transmission line with a much simpler sample geometry was desired for broadband operation.

Waveguide Transmission Line

Waveguide transmission lines consist of a conducting rectangle with one long axis and one short axis. Waveguides support a TEM mode with an electric field oscillating along its short axis, and the magnetic field oscillating along the longer axis Figure 2.10. These transmission lines are useful for characterisation of materials as they require a simple sample geometry. However, there are cutoffs for the minimum and maximum frequency of operation. Below the lower cutoff, an EM wave does not propagate, and above the upper frequency, higher order modes may be supported. This band restriction means that generally, several waveguides are used to characterise samples across different bands of frequency, and several different samples must be created for a wide-band characterisation to be completed. This not only makes the characterisation process time consuming, but also involves the potential problem of inconsistency between different sized samples.

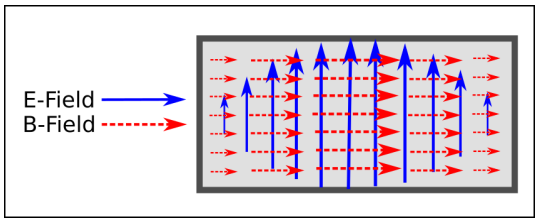

Figure 2.10: Diagram showing the electric and magnetic field lines in a rectangular waveguide transmission line.

In addition, characterisation of samples at low frequencies will require a substantial amount of material to produce large samples, which fit into the inevitably large waveguides at low frequencies. This is an issue for investigations into materials that are not available in large quantities.

Stripline Transmission Line

Stripline transmission lines consist of a rectangular center conductor situated half-way between two ground conductors above and below. Figure 2.11 shows a cross-section of this transmission line, with the associated field shape of the fundamental TEM mode supported. The impedance of this line is dictated by the height between the ground planes, thickness of

center conductor, as well as the width of center conductor and electromagnetic parameters of the dielectric filler used. The stripline geometry has a magnetic field that is circulating around a central conductor, as with a coaxial transmission line. This means that stripline transmission lines may operate at low frequencies without needing to be large structures. The simple shape of the cross section means simple sample geometries are also used. Figure 2.12 shows the geometry for a single part of an identical pair of samples used for characterisation.

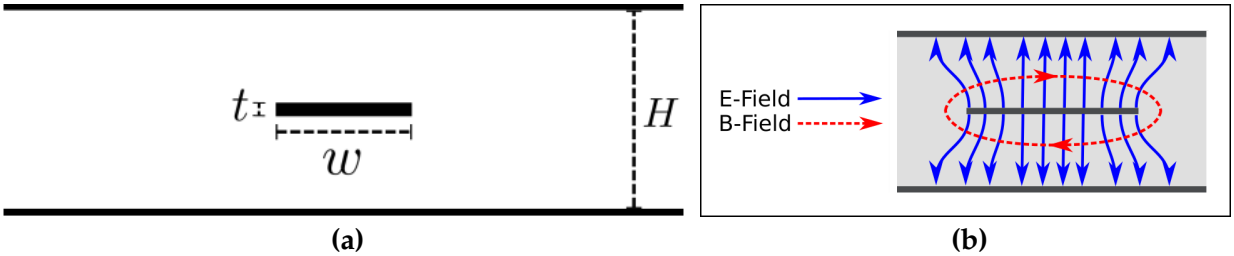

Figure 2.11: **(a)** Schematic showing the cross section of the stripline transmission line, with metal being indicated by solid black lines. **(b)** Diagram showing the electric and magnetic field lines in a stripline transmission line. This sample is insterted into the stripline above the cntral conductor, and a second inverted sample is placed beneath such that the steps of each sample are on either side of the conductor.

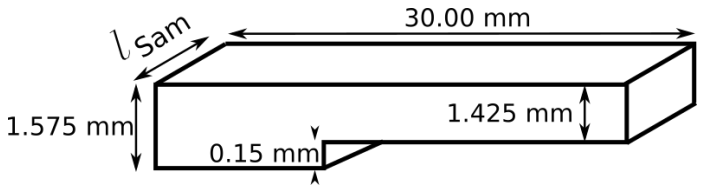

Figure 2.12: Schematic showing a possible sample geometry for use in stripline transmission lines. The sample has a step along the width that is for accomodating the central conducting strip. Pairs of these samples are made with the same value of l_{Sam} such that the whole cross section of the stripline may be filled with sample.

Although there is not a perfect analytical description of the relationship between impedance and the stripline parameters, researchers have attempted to provide direct equations from considering a stripline of zero thickness theorised from conformal transformation of a coaxial line [89], and for a stripline of finite thickness Equation (2.6) [90], assuming that the filler was dielectric with μ_r =1.

$$Z_0 = \frac{60}{\sqrt{\epsilon}} \ln \frac{3.8H}{0.8(w+t)} \tag{2.6}$$

Here H is the distance between upper and lower ground planes, w the width of center conductor, and t the thickness of conductor. This equation is accurate typically to an order of 6%. Others attempted to improve the determination of stripline impedance based on theory [91]. A figure showing how the stripline assembly is comprised is shown in Figure 2.13. The stripline is comprised of a brass housing that has been machined such that coaxial adapters may screw into the side walls. SMA pins are soldered to a copper central conducting line such that the strip will connect into the coaxial adaptors on assembly. The stripline is designed such that the top lid can be removed and placed back when samples require inserting.

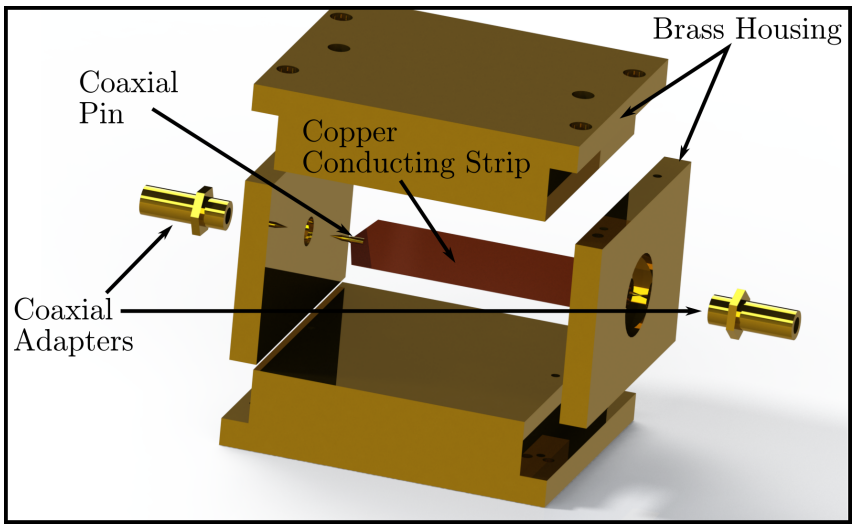

Figure 2.13: Schematic showing the design for the stripline assembly. A brass housing is produced that can accomodate coaxial adaptors at either end. SMA adaptors are soldered to a copper conducting strip such that the strip may be suspended between the top and bottom ground planes by the adapters.

In order to achieve impedance matching between stripline transmission lines and the coaxial lines used for experiment, a geometry that has an impedance of 50 Ω was chosen. An appropriate transition region between coaxial input and strip geometry is required such that the waves incident on the device are able to be modified gradually without reflection. This mode conversion is typically achieved by adding a 18°-20° taper to the strip from the coaxial pin to the final strip width as in Figure 2.14[27].

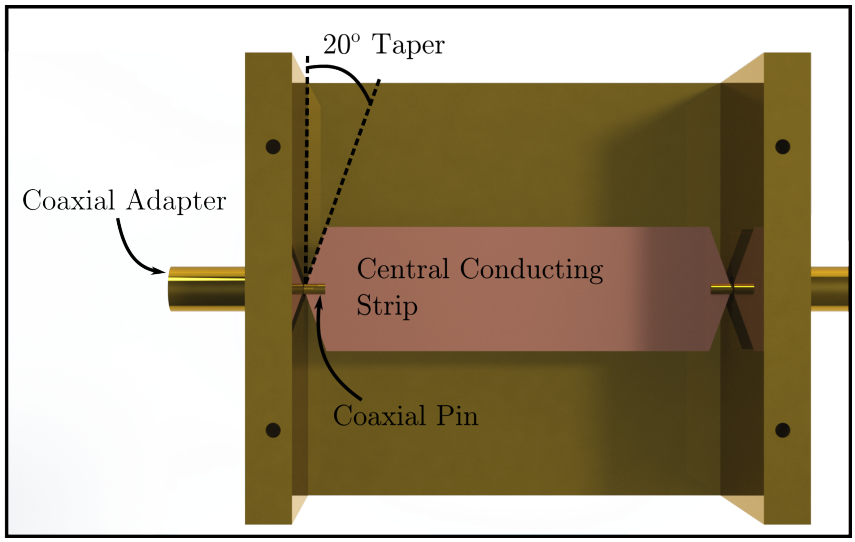

Figure 2.14: Schematic showing the typical transition region from coaxial input to stripline field applicator. A 20° taper is used for the transition region from coaxial line to stripline.

This type of transmission line, improved as described in Chapter 3 and Chapter 4, is used throughtout this work. An outline of how the data recorded with this device was analysed is now described,

2.11.1 Scattering Parameters

In free space, an incident Transverse Electric and Magnetic (TEM) wave will have an amount of its incident power reflected at the air-sample interface depending on the impedance mismatch between air and the sample under test, with the rest being transmitted into the sample. A secondary reflection will then occur at the sample-air interface resulting in a total reflected signal, and a transmitted signal Figure 2.15a. The evaluation of these waves is given by Fresnel's equations for transmission and reflection of a TEM wave at 0° incidence Equation (2.7). The reflected and transmitted signals, when measured by VNA, are referred to as S-parameters. S_{11} and S_{22} refer to the reflected signals at ports 1 and 2, respectively while S_{21} refers to the transmitted signal from port 1 to port 2 and S_{12} vice versa. For any reciprocal system, $S_{21} = S_{12}$. That is, the two transmitted signals from either side

through a system will always be identical, provided the end boundaries either side of the system are the same.

$$S_{11} = \frac{(1-T^2)R}{1-R^2T^2} \quad S_{21} = \frac{(1-R^2)T}{1-R^2T^2} \tag{2.7a}$$

$$R = \frac{Z_2 - Z_1}{Z_2 + Z_1} \qquad T = e^{-ink_0 d} \tag{2.7b}$$

$$Z = \sqrt{\frac{\mu_r}{\epsilon_r}} \qquad n = \sqrt{\epsilon_r \mu_r} \tag{2.7c}$$

An example of the expected S-parameters for a non-dispersive dielectric material in free space are shown in Figure 2.15b. S-parameters are complex, with the magnitude relating to the amplitude of wave, and phase relating to the phase delay of the wave as a result of propagation through the material.

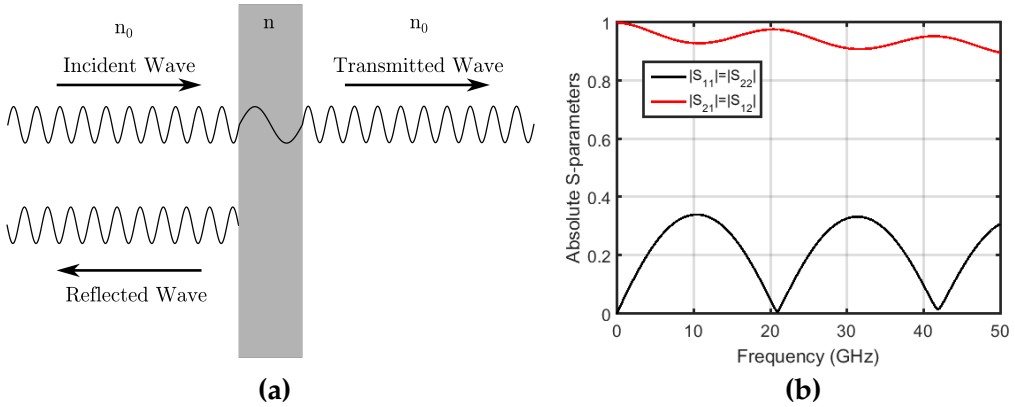

(a) **(b)**

Figure 2.15: (a) Diagram showing the reflected and transmitted signals for a wave incident upon a sample in free-space, at perpendicular incidence, and **(b)** Graph showing the typical model amplitudes of S-parameters when using a dielectric sample, with $\epsilon_r = 2.05 + 0.03i$, $\mu_r = 1.0 + 0.0i$ and a length of 5 mm. These values are calculated from Equation (2.7).

In order to obtain a representative set of data for the reflection and transmission of the composites under test, it is imperative to achieve impedance matching of the device being used to transmit the TEM mode incident on the sample. If impedance matching is not achieved, additional reflections shown by S_{11}^{A}, S_{11}^{B}, S_{22}^{A} and S_{22}^{B} in Figure 2.16 will give artefacts in the data from which erroneous values for the relative permittivity and permeability of the composite will be inferred. An example of model S-parameters that

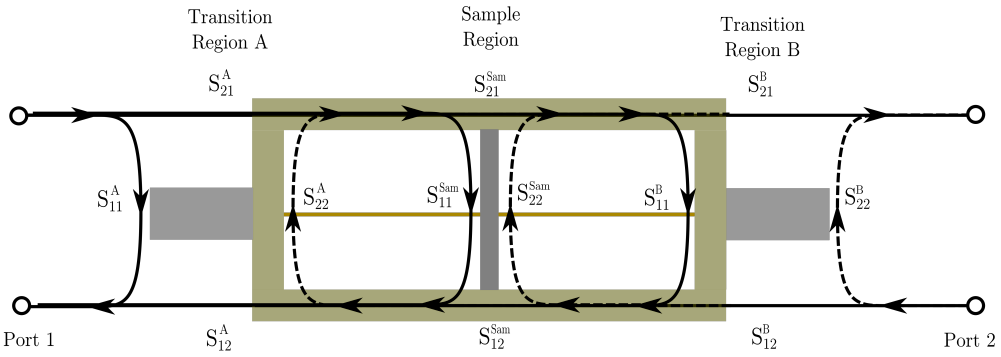

Figure 2.16: Diagram showing the signal flow diagram for reflected and transmitted signals when using a transmission device.

will be measured for a system with a sample in an air region with reflecting boundaries either side is shown in Figure 2.17. If these reflecting boundaries are unknown, an extraction of permittivity and permeability from the sample S-parameters will not be possible. A method for determining these reflecting boundaries before measurement is described in [26] and improvements to this method are detailed in Chapter 4.

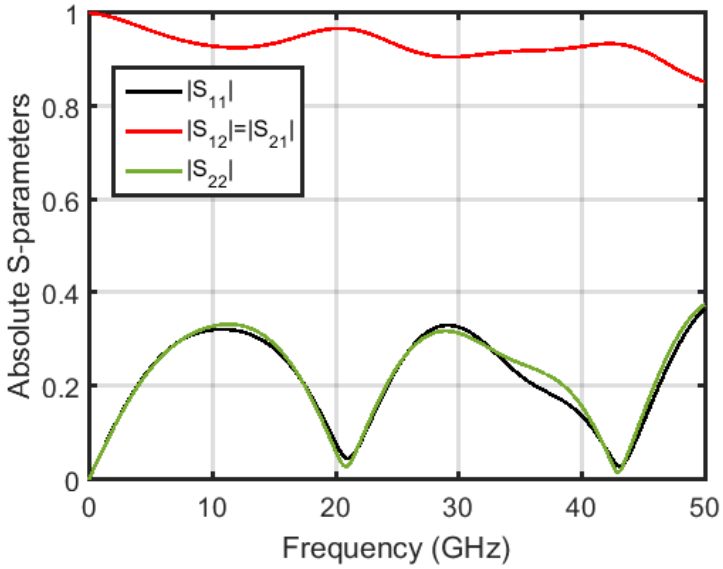

Figure 2.17: Graph showing the typical amplitudes of S-parameters when using a dielectric sample, with $\epsilon_r = 2.05 + 0.03i$, $\mu_r = 1.0 + 0.0i$ and a length of 5 mm in between two unknown lossy reflection boundaries. The oscillations in the data cannot be accounted for without knowing the S-parameters of the reflection boundaries.

2.11.2 Extraction of Electromagnetic Properties

This section will discuss two methods by which the EM properties of a sample may be extracted from measured S-parameters in experiment, based on Fresnel theory. The first, the Nicolson Ross-Weir method (NRW), was an extention from A. M. Nicolson's work to produce a method by which S-parameters may be recorded in the time domain that may be Fourier transformed into the frequency domain for analysis [92]. Nicolson then worked with G. F. Ross in 1970 to produce a method for extraction of EM properties from these readings [93]. In 1974, W. B. Weir provided an addition to the formulation that incorporated analysis of the phase data recorded in order to improve the data processing technique [94].
The second technique, the Three-Layer Sliding Window Fresnel fitting technique, will then be discussed which has been formulated by I. Hooper, and utilised by L. Parke and T. Campbell[5, 95, 96]. This involves again the use of Fresnel's equations but with a fitting regime to infer results for relative permittivity and permeability that correspond to recorded S-parameters.

2.11.3 The Nicolson Ross-Weir Method

The EM properties of samples may be inferred from the measured S-parameters of the device by use of the Nicolson Ross-Weir method, which uses a reformulation of Fresnels's equations to relate the real and imaginary components of S_{11} and S_{21} to the real and imaginary components of ϵ_r and μ_r. The NRW approach fails to extract accurate values for permittivity and permeability for frequencies corresponding to a $\frac{\lambda}{2}$ Fabry-Perot resonance in the propagation length of the sample. This may be avoided by choosing sample lengths that are either small enough that this resonance occurs outside the frequency range of measurement, or by characterising more than one sample with differing lengths, such that these resonances occur at different frequencies. Multiple datasets are then combined for a continuous set of data.

The source of this failure in the NRW procedure arises from the fact that at a Fabry-Perot resonance for a low-loss material, $|S_{11}|$ will approach zero, as seen in Figure 2.15b, which shows the absolute values of reflected and transmitted signals considering Fresnel's equations Equation (2.7) for a dielectric sample of permittivity $\epsilon_r = 2.05 + 0.03i$ that is 5 mm long, with a $\frac{\lambda}{2}$

resonance occurring at ∼21 GHz. At this point the values for permittivity and permeability that correspond to a zero reflection term are degenerate. Work has been undertaken for various methods of determining permittivity and permeability at these positions in frequency, however most require the assumption that the sample is non-dispersive over the range of concern [97]. A different method by which broadband datasets can be reliably analysed for extracting both permittivity and permeability is therefore required.

2.11.4 The Three-Layer Sliding Window Fresnel Method

Another method by which the EM properties of a material may be inferred from measured S-parameters is by utilisation of a Sliding-Window Fresnel fit. This method involves a sample frequency range of the measured S-parameters to be fit to with the use of Fresnel theory, from which values for permittivity and permeability may be extracted over this range. This value is then used as the initial guess for a fit to the next frequency 'window' of measured S-parameters to be fit to and so on until the entire data set is fitted. This method is reasoned to allow better accuracy in fitting to S-parameters when $|S_{11}|$ approaches zero at Fabry-Perot resonances as more data is being incorporated into the fit, reducing uncertainty in the extraction.

2.12 Conclusions

The primary factors in magnetism that affect the frequency response of magnetic materials have been discussed in this chapter, namely the shape and magnetocrystalline anisotropies, as well as the exchange energy term. It is necessary to consider all of these terms when investigating the primary FMR mode of magnetic materials. It has been demonstrated that these factors may be modified to tune the position in frequency that this FMR mode occurs. By tuning the frequency at which this primary absorption mode occurs, as well as the quality of the resonance, it is possible to tune the absorption properties of composites. This is imperative for either enhancing the low-frequency permeability of materials for broadband impedance matching and antenna miniaturisation or for broadening the resonance to provide EM absorbers.

The existence of higher order spherical magnetic modes has also been discussed for carbonyl iron powders, or other ferromagnetic spheres that

have diameter of the order of 1 μm. These higher order modes exist at frequencies above the FMR. These modes may be used to extend the working frequency range of magnetic materials without the loss of low frequency response as it is possible to incorporate these modes into materials without changing the shape anisotropy. The investigation into these higher order modes is necessary for tailoring materials to have sharp absorption modes at specific frequencies above 10 GHz and for providing non-unity permeability at these high frequencies.

The transmission line method for electromagnetic characterisation of composite materials has also been introduced, and potential obstacles in experiment have been outlined. The primary obstacle in experiment is related to achieving broadband measurement of the S-parameters that are accurate and do not include artefacts that are a result of the transmission line used. The technique developed in this work is useful for the characterisation of materials across frequency ranges that have been unprecedented for single measurements of samples. The next chapter discusses methods by which obstacles in measurement have been overcome, as well as other experimental methods used throughout this project.

Chapter 3

Methods

3.1 Introduction

In this chapter, the experimental methods that are used throughout this project are presented alongside a list of the materials used in the work. Two methods of sample fabrication for the production of composites comprised of a dielectric filler loaded with material to be investigated is first described, then the technique for filtration of powders based on particle size is covered. A brief introduction to the stripline transition region optimisation is then discussed before the theory of electromagnetic characterisation of samples from S-parameter measurements is presented. Lastly, imaging and sectioning techniques for using the SEM and FIB to characterise physical properties of the particles such as size and internal structure are introduced.

3.2 Composite Fabrication

Composites were required for analysis of the properties of CIP. These composites needed to be homogeneous, non-conducting, and required accurate dimensions for fitting into the transmission line used. Originally, stock material was made from these composites before being milled to shape. This processing was compatible with both methods of sample fabrication, wet-casting and cold-pressing. Two different dielectric matrices were tested for composite manufacture, Polytetraflouroethylene (PTFE or Teflon), and polyurethane. PTFE powder was used for the cold-press technique and polyurethane was used for the wet-cast technique.

3.2.1 Cold-press Technique

The cold-press technique involves dry mixing of PTFE powder with the loading material before pouring into a cylindrical mould. Three average particle sizes for PTFE powder were used, ~ 1 μm, $\leq$12 μm and $\sim$35 μm, all sourced from *Sigma-Aldrich*. There was little difference in the quality of samples prepared with each of these powders. The mixed material was placed into a cylindrical mould and was pressed in a pneumatic press at 600 kgcm^{-2} for 300 s before removing a 30 mm diameter cylindrical disc for milling to shape. This technique was originally used for dry mixing of irregularly shaped ferrite powders rather than spherical carbonyl iron powders, and volume loadings as high as 70%vol. were reached [4]. However, with spherical powders, this high volume loading was not attainable. Samples comprising 30%vol. CIP were found to be difficult to mill to shape for measurement without breaking and also began to conduct by percolation, making them unsuitable for the investigation of spherical magnetic modes.

3.2.2 Wet-cast Technique

Wet-casting samples involved the use of a 2 part polyurethane fast cure kit named *Xencast P2 Fast Cast Polyurethane Casting Resin* from *Easy Composites*. The polyurethane parts mixed at a 1:1 ratio, and were both low viscosity, with part A having a viscosity of $\sim$90 mPa·s and part B having a viscosity of $\sim$65 mPa·s, as given on the technical data sheet. The low viscosity of the polyurethane parts allowed high volume loading of material before the mixture became too viscous to pour into a mould. Samples were fabricated by first weighing out the desired amount of Part A for the polyurethane mixture, and adding the correct amount of magnetic or dielectric loading. This mixture was stirred until an even consistency was reached before adding an equal amount of Part B to the mixture and stirring thoroughly again. This mixture was then poured into a mould and left for $\sim$ 40 min. For loadings above 40%vol. loading, each of the parts of the polyurethane mixture were mixed with one half of the total powder to create part A and part B "putties" that were able to be mixed by working together by hand. This combined putty was then pressed into a mould rather than poured. When making samples with these higher volume loadings the resulting samples

were much more brittle than samples with loadings $\leq$30%vol. The risk of air bubbles and cracked samples was also greater.

Originally samples were being cast as stock to be milled after curing. Later, to save time in sample preparation, a sample mould specifically designed for the stripline was created. This produced samples that were 1.575 mm tall with a 0.15 mm step half way along to accomodate the central conducting strip of the line. A schematic of this mould is displayed in Figure 3.1.

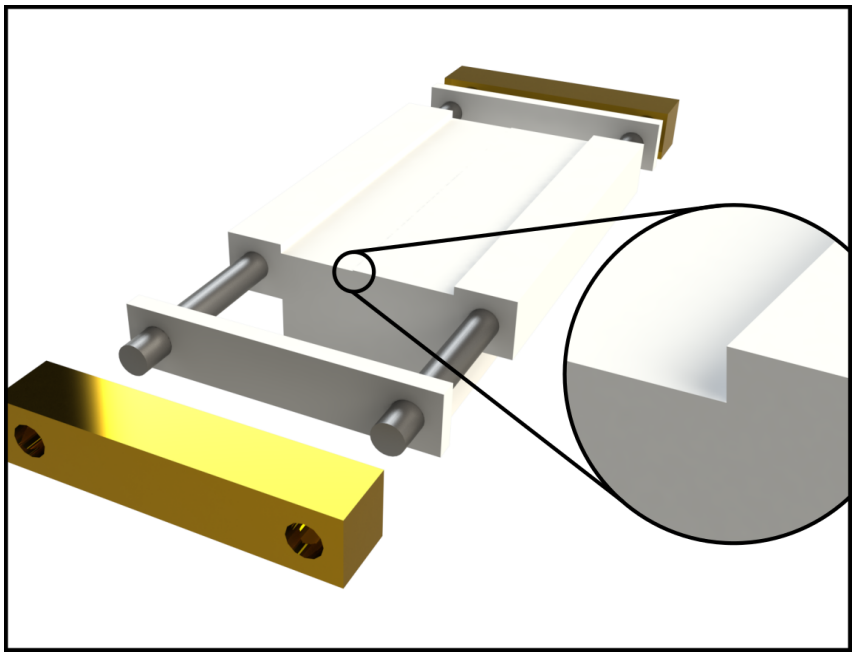

Figure 3.1: Figure displaying the Teflon mould used for wet-casting samples.

The sample stock made in this mould was cut into pairs of strips with equal widths to enable multiple samples of different propagation thicknesses to be made in a single batch. By making the mould from Teflon, samples could be removed with little difficulty.

3.3 Particle Size Filtration

The need to separate powders into separate sub-grades based on particle size distribution required a technique for filtering powders that were in the single-micron size range and smaller. Works have been published where nano-sized powders have been extracted from CIP grades by the use of a sieve and then using a sedimentation technique in IPA [98]. However, this technique is shown to be both laborious and low-yield, with only milligrams of powder being extracted at a time. This technique also requires drying filtered powders from the IPA solution. The effect of this step on the properties of the powder are not fully known, but agglomeration is a likely issue. Ideally a technique should be useful for batch processing carbonyl iron powders without needing to wet the particles.

3.3.1 Mechanical Sifting

Due to the particles of these powders being so small, sieves with fine enough apertures to sift the powders are both sparse and expensive. Methods for mechanically sifting powders smaller than a few microns in size without wetting the powders do exist, for example using a sonic sifter separator such as *Advantech L3P Sonic Sifter Separator*. However, the equipment is again too expensive, meaning another method needed to be explored.

3.3.2 Air Elutriation

Air elutriation is a technique that has long been used for particle size separation [99, 100]. In its simplest form, air elutriation involves the use of a laminar air flow at a known volume flow rate to lift a dust cloud of particles through a chamber against gravity. The volume flow rate can be tuned by either selecting the diameter of the chamber, or the volume rate of flow for the air input. This flow will lift particles smaller than a cutoff determined by the density of particles and the volume flow rate in the chamber. See Figure 3.2.

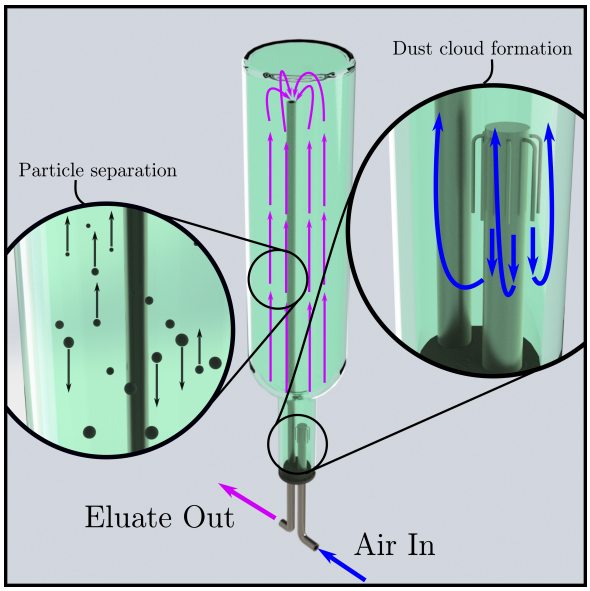

Figure 3.2: Schematic showing how a glass bottle may be used for the air elutriation experiment.

The theory for predicting the average volume flow rate required to lift CIP particles of different sizes is derived from the Navier-Stokes equation when considering a Reynolds number that is low. The Reynolds number for Stokes flow is a dimensionless term that quantifies the relative size of the particles with respect to the flow speed and density of the fluid. The Reynolds number for the system of micron-sized iron powders in air with a flow speed on the scale of mm/s is on the order of 10^{-5}. This means we may consiuder the elutriation of CIP in air to be a low Reynolds number system. The drag force of a fluid on a spherical particle is given by Stokes' drag equation [101];

$$F_{\mathrm{D}} = 6\pi\mu R u. \tag{3.1}$$

Here, R is the radius of the particle, u is the velocity of the fluid given by relating the fluid volume flow rate and the area of the chamber and μ the dynamic viscosity of the fluid. The force on the powder due to gravity and bouyancy are;

$$F_{\mathrm{Grav}} = g(\rho_{\mathrm{p}} - \rho_{\mathrm{f}}) \cdot \frac{4}{3}\pi R^3 \tag{3.2}$$

where g is the gravitational constant and ρ_{p} , ρ_{f} are the particle and fluid densities, respectively. At the point of being able to lift a particle with fluid flow, these two forces balance, leading to the equation relating fluid velocity

and maximum particle radius. We may then simply add a conversion from fluid velocity to volume flow rate, considering the diameter, d, of the bottle to give a final equation relating maximum particle radius to input volume rate of flow, Q.

$$u = \frac{2}{9\mu} g(\rho_{\mathrm{p}} - \rho_{\mathrm{f}}) R^2 \tag{3.3}$$

$$Q = \frac{10\pi g}{3\mu} \cdot (\rho_{\mathrm{p}} - \rho_{\mathrm{f}}) d^2 R^2 \tag{3.4}$$

Two glass bottles were used for the final setup of this experiment, one with an inner diameter of $\sim$ 65 mm and a second with inner diameter $\sim$ 180 mm. The ratio of these two diameters allows particles that have been lifted from the first bottle to settle in the second bottle for collection. The bottles were connected in series by 6 mm diameter stainless steel tubing, and a constant volume flow rate was pumped through the whole system. Glass bottles were used due to their ease in availability. These bottles are also easy to clean, and the transparency allows inspection of dust cloud formation. The neck of the bottle gives a funnel for the air flow, meaning a high airflow in the neck can cause turbulence and form a dust cloud before it settles into a laminar flow by the maximum diameter section of the bottle. The shoulder of the bottle also funnels settled powder back into the neck of the bottle for recirculation. Some particles that would be small enough to pass through the chamber will likely settle at the sides of the bottle due to static, so recirculating these particles is essential for ensuring all particles below the cutoff size are removed from the bulk.

Powder is added to the first bottle chamber, and the bottle is inverted such that the powder sits in the neck of the bottle. Then air flow is passed through the nozzle in the neck of this bottle. The nozzle was made by first cutting slots into the end of a 6 mm diameter stainless steel tube. Into each of these slots, a syringe needle was inserted and bent such that the air exiting the tube could be redirected downwards. A schematic of this nozzle is shown in the inset of Figure 3.2. This creates jets of air whose turbulence encourage the formation of dust clouds from the settled powder. This was further enhanced by adding a vibrational motor to the system, causing powder to be constantly agitated as well as knocking settled powder back from the sides of the bottle into the bulk. Once this method had been shown to

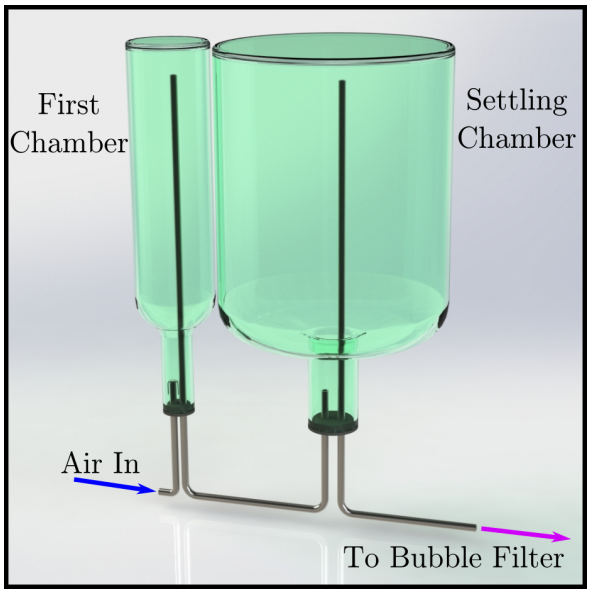

Figure 3.3: Schematic showing the experimental setup for air elutriation with a second collection chamber attached in series to the filtration chamber. This second chamber collects the particles filtered from the bulk.

work for the removal of small particles, a second chamber was connected in series to the first bottle by 6 mm diameter stainless steel tubing, as in Figure 3.3. This additional bottle has a significantly wider diameter. This was to allow the flow speed to be reduced such that the particles in the eluate from the first chamber could settle for collection. A bubble filter was added after this collection chamber to safely capture any particles that had passed through the entire system.

3.4 Stripline Tranisition Region Optimisation

In order to optimise the impedance of the stripline, a genetic algorithm was added to HFSS modelling to optimise the shape of the transition regions from coaxial pin to final strip width. The shape of the transition region was defined by 10 evenly spaced strips in the propagation direction with unknown widths. These widths were able to be freely chosen by the genetic algorithm. This genetic algorithm was applied to optimise values for each of these 10 widths and run the model of the new geometry to determine S_{11} and S_{21}. The objective function of the genetic algorithm was to maximise $|S_{21}|$ and minimise $|S_{11}|$. Once a rough geometry had been converged upon,

simpler geometries were chosen that matched the general shape of the transition regions while being defined by fewer terms. This allowed a second optimisation to be run and ensure a global minimum had been found. The final geometry converged upon is discussed further in Chapter 4

3.5 Parameter Extraction

This section covers the calibration method required for stripline characterisation of materials, beginning with the T-matrix formulation used for analytically modelling the experimental setup. After this, the procedure used to find the position of samples in the stripline transmission line for accurate analysis of the S-parameters recorded experimentally is presented.

3.5.1 T-Matrix Formulation

The T-matrix formulation is used for providing a model of wave propagation through layered media. From T-matrices, it is possible to make a model set of S-parameters for a layered system. The T-matrix formulation comprises 2 matrices; a transfer matrix, which evaluates the reflection and transmission at a boundary, and a propagation matrix which adjusts the phase for propagation through a medium, depending on the refractive index and thickness of the material.

These two transfer matrices have the following form;

$$\left[T^{\text{Transfer}}\right] = \frac{1}{\tau}\begin{bmatrix} 1 & \rho \\ \rho & 1 \end{bmatrix} \tag{3.5}$$

$$\left[T^{\text{Propagation}}\right] = \begin{bmatrix} \phi & 0 \\ 0 & \phi^{-1} \end{bmatrix} \tag{3.6}$$

where

$$\phi = e^{ik_0 Ln}, \qquad k_0 = \frac{2\pi f}{c},$$

$$\rho = \frac{Z-1}{Z+1}, \qquad \tau = \frac{2Z}{Z+1},$$

$$Z = \sqrt{\frac{\mu_r^*}{\epsilon_r^*}}, \qquad n = \sqrt{\epsilon_r^* \mu_r^*},$$

$$\epsilon_r^* = \epsilon_r' + i\epsilon_r'', \quad \mu_r^* = \mu_r' + i\mu_r''.$$

Here, ϕ is a phase term, dependent upon the distance propagated through the sample, L, the refractive index, n, and free-space wavenumber, k_0. f is the frequency, c is the speed of light, ρ is the reflection coefficient and τ the transmission coefficient. Z is the characteristic impedance of the material. Using these equations, it is possible to derive the S-parameters for a slab of material with known permittivity and permeability across a given frequency range. A sample with length L, relative permittivity, ϵ_r*, and relative permeability, μ_r*, would have its transfer matrix described by multiplication of the following matrices:

$$\left[T^{\text{Total}}\right] = \frac{1}{\tau}\begin{bmatrix} 1 & \rho \\ \rho & 1 \end{bmatrix} \cdot \begin{bmatrix} \phi & 0 \\ 0 & \phi^{-1} \end{bmatrix} \cdot \frac{1}{\tau'}\begin{bmatrix} 1 & -\rho \\ -\rho & 1 \end{bmatrix} \tag{3.7}$$

where

$$\tau' = \frac{2}{Z+1}$$

Multiplying these transfer matrices through, and using the common S-parameter relations to T-parameters:

$$\begin{gathered} S_{11} = \frac{T_{21}}{T_{11}} \qquad S_{21} = \frac{1}{T_{11}} \\ S_{22} = \frac{-T_{12}}{T_{11}} \quad S_{12} = \frac{\text{Det}|T|}{T_{11}} \end{gathered} \tag{3.8}$$

this returns S-parameters of:

$$S_{11} = \frac{\rho\phi - \rho\phi^{-1}}{\phi - \rho^2\phi^{-1}} \tag{3.9}$$

$$S_{21} = \frac{\tau\tau'}{\phi - \rho^2\phi^{-1}} \tag{3.10}$$

In the case of a single slab of material, $S_{11} = S_{22}$ and in all cases, $S_{21} = S_{12}$. The only case when transmission in each direction will not be equal is if the system is non-reciprocal. This means the impedances that are on either port are not the same, so the fields have not been matched to the same external media on each side of the material. In all cases here, the S-parameters are given when matching the material to ports that are considered to be air, meaning all indices, impedances, permittivities and permeabilities are relative to air. When describing a system comprising multiple layers of material, it is possible to calculate the T-matrix for each individual material before simply multiplying them together in the order that the materials occur in the system. Then one can convert into S-parameters again for the description of the full system. This means a set of T-matrices may be used to describe the stripline system before converting back into S-parameters to compare with experimental measurements. T-matrix formulation was used to model the stripline system for the short-measurement calibration applied throughout the project.

3.5.2 Short-measurement Calibration of the Stripline

The stripline may be considered to be comprised of three sections; two transition regions, A and B, as well as a sample region in the middle that is the section of stripline with constant strip width. Each of these sections may be described by a T-matrix, which can be converted into S-parameters by the previously described relations.

$$\left[T^{\mathrm{A}}\right] = \begin{bmatrix} T_{11}^{\mathrm{A}} & T_{12}^{\mathrm{A}} \\ T_{21}^{\mathrm{A}} & T_{22}^{\mathrm{A}} \end{bmatrix} \quad \left[T^{\mathrm{B}}\right] = \begin{bmatrix} T_{11}^{\mathrm{B}} & T_{12}^{\mathrm{B}} \\ T_{21}^{\mathrm{B}} & T_{22}^{\mathrm{B}} \end{bmatrix}$$

$$\left[T^{\mathrm{Sam}}\right] = \begin{bmatrix} T_{11}^{\mathrm{Sam}} & T_{12}^{\mathrm{Sam}} \\ T_{21}^{\mathrm{Sam}} & T_{22}^{\mathrm{Sam}} \end{bmatrix}$$

The sample region is described by a T-matrix that is dependent upon the content of the sample region. This will either be an empty air region, in which case the T-matrix is simply a propagation matrix for the length of the constant width region of the stripline. If the sample region contains a

sample for characterisation, it is then described by a three-layer model with air either side of a material of unknown permittivity and permeability.

In the case of a measurement of the stripline with a short inserted, the sample region is described by

$$\left[T^{\text{Sam (Short)}}\right] = \begin{bmatrix} \phi & 0 \\ 0 & \phi^{-1} \end{bmatrix} \cdot \frac{1}{\tau} \begin{bmatrix} 1 & -1 \\ -1 & 1 \end{bmatrix} \cdot \begin{bmatrix} \phi_{\text{Short}} & 0 \\ 0 & \phi_{\text{Short}}^{-1} \end{bmatrix} \cdot \frac{1}{\tau'} \begin{bmatrix} 1 & 1 \\ 1 & 1 \end{bmatrix} \cdot \begin{bmatrix} \phi' & 0 \\ 0 & \phi'^{-1} \end{bmatrix}. \tag{3.11}$$

Here, the propagation matrices containing ϕ and ϕ' depend on the position of the short bar.

Multiplying these T-matrices through gives the final T-matrix:

$$\left[T^{\text{Tot}}\right] = \frac{1}{\tau\tau'} \begin{bmatrix} (T_{11}^{\text{A}} - T_{12}^{\text{A}}\phi^{-1})(T_{11}^{\text{B}}\phi' - T_{21}^{\text{B}}\phi'^{-1}) & (T_{11}^{\text{A}} - T_{12}^{\text{A}}\phi^{-1})(T_{12}^{\text{B}}\phi' - T_{22}^{\text{B}}\phi'^{-1}) \\ (T_{21}^{\text{A}} - T_{22}^{\text{A}}\phi^{-1})(T_{11}^{\text{B}}\phi' - T_{21}^{\text{B}}\phi'^{-1}) & (T_{21}^{\text{A}} - T_{22}^{\text{A}}\phi^{-1})(T_{12}^{\text{B}}\phi' - T_{22}^{\text{B}}\phi'^{-1}) \end{bmatrix}. \tag{3.12}$$

By using this analytical model of the total system, and the conversion from T-parameters to S-parameters, an expression for the reflection at Port 1 may be given in terms of transition region A and the position of the 'short' bar.

$$S_{11}^{\text{Short}} = \frac{T_{21}^{\text{A}}\phi - T_{22}^{\text{A}}\phi^{-1}}{T_{11}^{\text{A}}\phi - T_{12}^{\text{A}}\phi^{-1}}. \tag{3.13}$$

By using this equation, it is possible to fit to reflection measurements of the stripline with a shorting bar inserted. By inserting a shorting bar at more than 3 positions, measurements will provide enough information to extract the T-matrix for each transition region.

It is not possible to infer an expression for S_{22} from this model, as the determinant of the final T-matrix is zero. Instead, transition region 2 is described by (3.14) and the S-parameters are defined by (3.15).

$$S_{22}^{\text{Short}} = \frac{T_{21}^{\text{B}}\phi' - T_{22}^{\text{B}}\phi'^{-1}}{T_{11}^{\text{B}}\phi' - T_{12}^{\text{B}}\phi'^{-1}} \tag{3.14}$$

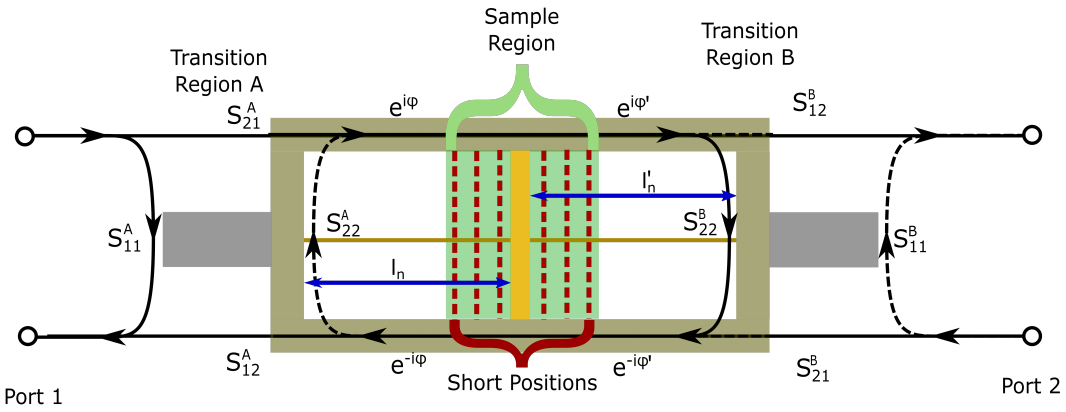

Figure 3.4: Signal flow diagram showing the positions at which shorting bars are placed in order to gain information on the S-parameters for the transition regions.

$$S^B_{11} = \frac{-T^B_{12}}{T^B_{11}} \quad S^B_{21} = \frac{\mathrm{Det}|T^B|}{T^B_{11}}$$
$$S^B_{22} = \frac{T^B_{21}}{T^B_{11}} \quad S^B_{12} = \frac{1}{T^B_{11}} \tag{3.15}$$

Essentially, this mathematical definition is the same as treating the stripline as though it has been connected to the VNA from the opposite side, so $S_{11} \rightarrow S_{22}$ and $S_{21} \rightarrow S_{12}$.

Once the transition regions for the stripline have been characterised, it is then possible to de-embed sample S-parameters from the S-parameters measured for the stripline with the sample inserted. This is acheived by converting the measured S-parameters into a T-matrix, and simply multiplying the converted T-parameters by the inverse matrices of the transition regions. The resulting T-matrix is then converted back into a set of S-parameters for the sample alone.

$$\left[T^{Total}\right] = \left[T^{\mathrm{A}}\right] \cdot \left[T^{\mathrm{Sam}}\right] \cdot \left[T^{\mathrm{B}}\right]$$
$$\left[T^{Sam}\right] = \left[T^{\mathrm{B}}\right]^{-1} \cdot \left[T^{\mathrm{Tot}}\right] \cdot \left[T^{\mathrm{A}}\right]^{-1}$$

A set of 3 or more short readings is sufficient information for the characterisation of transition regions. When using only 3 measurements of the stripline with shorting bars at different positions, there is a degeneracy in

the solution to the transition regions that occurs at a point in frequency corresponding to the distance between the first and final short reading. For example, if the distance to each n short reading is l_n, the frequency of calibration failure will be $\frac{2*3\times10^8}{l_n-l_1}$ Hz. Examples of the extracted S-parameters for a 5 mm polyurethane sample are displayed in Figure 3.5. In each of these extractions, a different distance between short readings had been used. The phases for the reflected signals at Port 1 for each of these sets of short merasurements are shown in Figure 3.6. As can be seen from Figure 3.6, the phase of the three short readings coincides at frequencies that are related to the greatest distance between short readings. These points where the phases coincide are the same points that transition region characterisation fail in Figure 3.5. There is also error in extraction at low frequencies, when the short readings again become too similar to be distinguished against electrical noise.

The results for extracted S-parameters have errors in extraction at $\sim$16 GHz, $\sim$24 GHz and $>$30 GHz for Figures 3.5a, 3.5b and 3.5c respectively. These extractions were made using shorts readings that had maximum distances between each other of 9.3 mm, 6.2 mm and 3.3 mm respectively. It is possible to provide even more data to fit by attaching a calibration standard to each end of the stripline and measuring the reflection that results. In this case the measurement system is modelled by the total stripline T-matrix multiplied by that for the calibration standard chosen, as in (3.16) and (3.17). The calibration standards used for experiment were Short and Open calibration standards from *Anritsu Network Analyzer V Calibration Kit Model 3654D*. Measurements of the S-parameters for the empty stripline were also taken to fit to.

$$\left[T^{\text{Open}}\right] = \left[T^{\text{Stripline}}\right] \cdot \begin{bmatrix} \phi_{\text{Standard}} & 0 \\ 0 & \phi_{\text{Standard}}^{-1} \end{bmatrix} \cdot \begin{bmatrix} 1 & \rho_{\text{Open}} \\ \rho_{\text{Open}} & 1 \end{bmatrix} \tag{3.16}$$

$$\left[T^{\text{Short}}\right] = \left[T^{\text{Stripline}}\right] \cdot \begin{bmatrix} \phi_{\text{Standard}} & 0 \\ 0 & \phi_{\text{Standard}}^{-1} \end{bmatrix} \cdot \begin{bmatrix} 1 & \rho_{\text{Short}} \\ \rho_{\text{Short}} & 1 \end{bmatrix} \tag{3.17}$$

There is an extra term in these equations which relates to the electrical

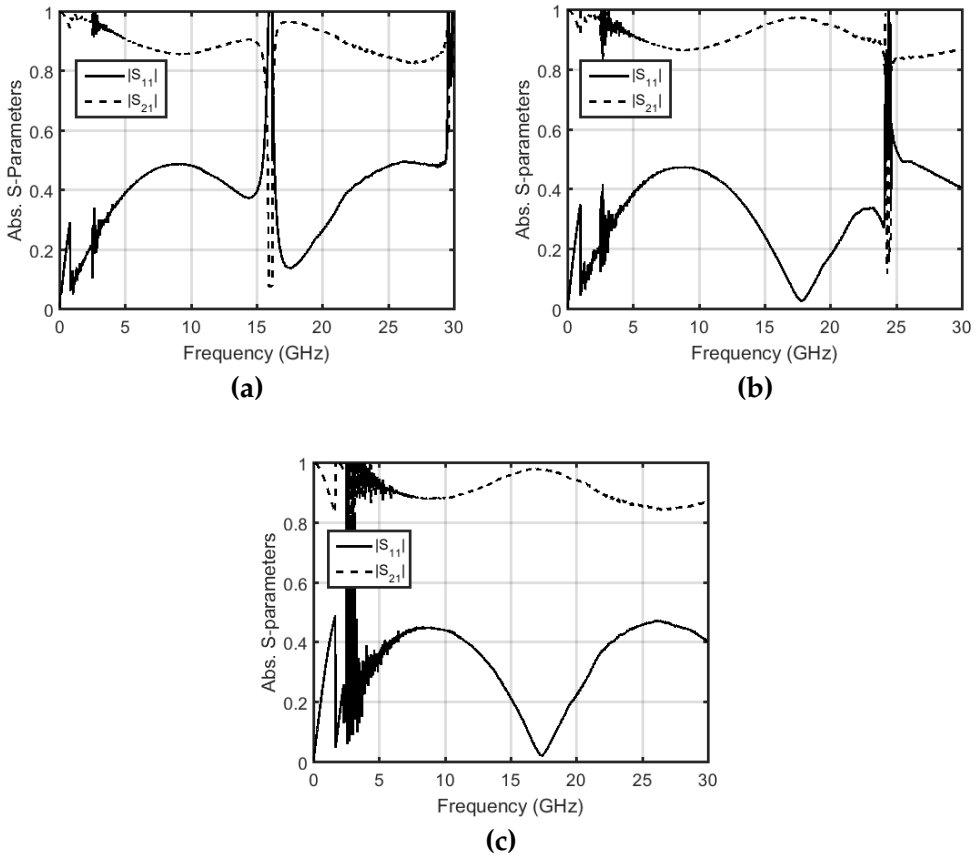

Figure 3.5: Extracted sample S-parameters for a set of S-parameters measured for the stripline geometry with a 5 mm polyurethane sample inserted. The sample S-parameters have been extracted using short calibration measurements with maximum spacings of **(a)** 9.3 mm, **(b)** 6.2 mm, and **(c)** 3.3 mm.

length of each standard. This must be taken from the calibration kit specification to accurately describe the system. It would be possible to define the sysem more accurately by also taking reflection terms from an elecrical model of the standards based on capacitance and inductance values. The assumption that these reflection terms were ρ_{Open}=1 and ρ_{Short}=-1 was sufficient for characterisation of the transition regions.

At low frequencies, the difference in phase of the short measurements become so small that they are masked by noise so solutions again become degenerate. Having measurements of the S-parameters for the empty stripline and measurements of the reflections from each side of the empty stripline with calibration standards attached gives greater reliability in the characterisation of the transition regions at low frequencies as the phase gradient

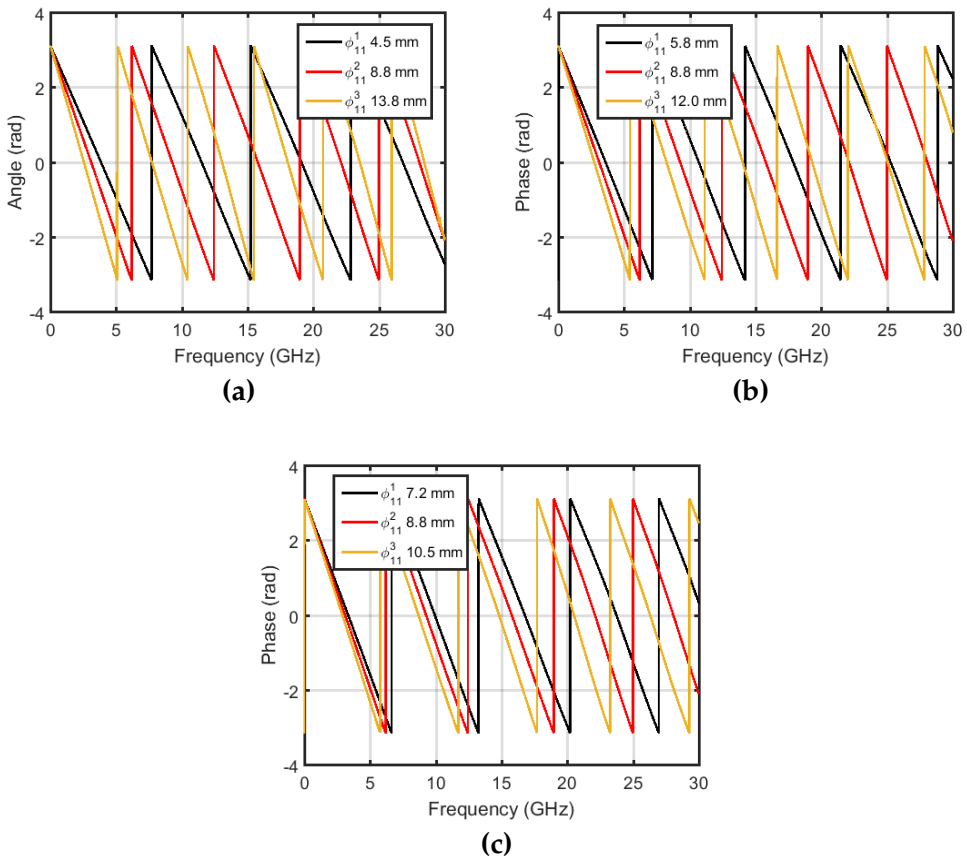

Figure 3.6: Phases of the S_{11} measurement for the shorted stripline with shorts placed at average distances from eachother of **(a)** 4.6 mm, **(b)** 3.1 mm, and **(c)** 1.7 mm.

of these signals is greater than that for the shorted readings. The result of extracting sample S-parameters for a 5 mm polyurethane sample in the stripline using transition regions inferred from these additional measurements is shown in Figure 3.7.

The results above show that the extraction of sample S-parameters when fitting to a set of 7 short readings, as well as S-parameter measurements of the empty stripline with and without calibration standards has significantly better extraction at low frequencies, as well as no errors at frequencies corresponding to the distance between each short reading. The erroneous point at $\sim$3 GHz is due to an equipment fault.

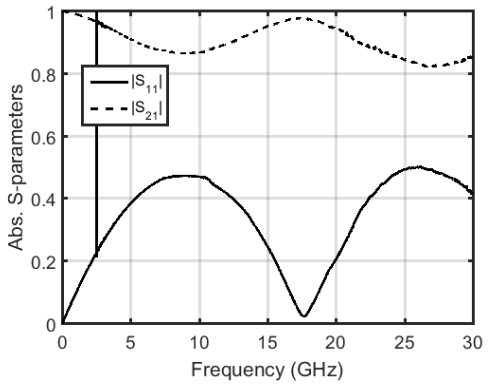

Figure 3.7: Graphs showing for a 5 mm polyurethane sample from the measured stripline geometry, the extracted sample S-parameters extracted using measurement of all previous short readings together with measurements of the empty stripline with and without calibration standards attached at each end.

3.5.3 Offset Sample Correction

The position of the sample in the stripline may be determined from the phases of the reflected signals from either side of the sample. This will allow ϕ^{A} and ϕ^{B} to be determined directly from measurement. If the sample is placed centrally in the stripline, the phases of the reflections will match, as the distance travelled by the reflected signals is the same. If the sample is off-center, the signals will have a discrepency in phase. By adjusting the offset of the sample in the model until the de-embedded phases coincide, it is possible to determine the necessary offset correction for off-center placement of the sample.

In order to perform this correction, a code is written that takes the phase of the corrected S_{11} and S_{22} signals with a guessed phase factor. The code then adjusts the phase factor that corresponds to the distance, d, from the beginning of the sample region to the sample – air interface until $\phi_{11}^{\mathrm{Corrected}} = \phi_{22}^{\mathrm{Corrected}}$.

$$\phi_{11}^{\mathrm{Corrected}} = \phi_{11}^{\mathrm{Measured}} + 2k_0 d$$

$$\phi_{22}^{\mathrm{Corrected}} = \phi_{22}^{\mathrm{Measured}} + 2k_0(L - l_{\mathrm{Sam}} - d).$$

Here, L is the length of the sample region, l_{Sam} is the length of the sample, and d is the distance to the first face of the sample. The offset factor, d, is found when the corrected phases, $\phi_{11}^{\text{Corrected}}$ and $\phi_{22}^{\text{Corrected}}$ coincide.

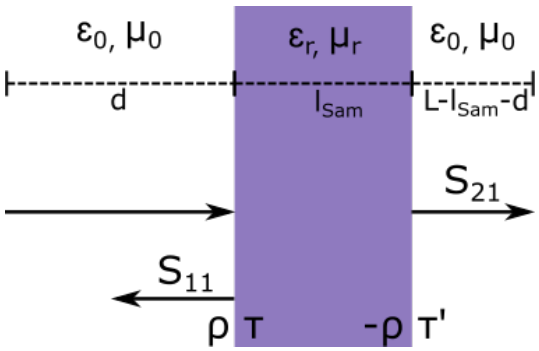

Figure 3.8: Schematic showing the three-layered system that is considered when fitting to de-embedded sample S-parameters. The model assumes that the sample is not centrally placed, and the position of the sample must be determined from analysing the phases of the reflected signals.

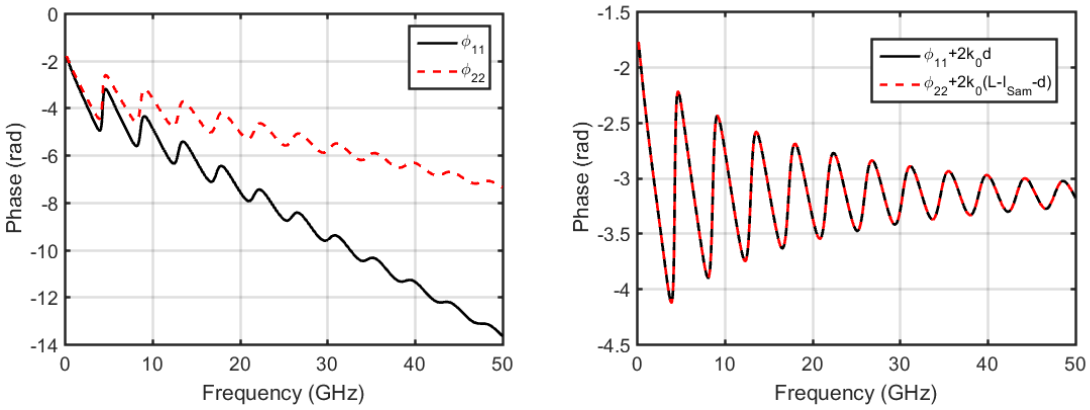

Figure 3.9: Figures comparing the uncorrected **(a)** and corrected **(b)** phases for the reflected signals for a test sample that is offset by a distance d from the centre of the sample region.

Examples of the uncorrected and corrected phases of reflected signals for a modelled set of S-parameters with an offset sample are shown in Figure 3.9. This technique for finding the position of samples was also applied for finding the positions of each short reading for the stripline.

3.6 Particle Cross-section Analysis

In order to investigate the internal structure of particles, scanning electron microscope (SEM) analysis of the cross-sections for these particles was necessary. In order to achieve these images, a method for cutting particles into hemispheres was required. First a particle-by-particle approach was attempted, using a FIB to cut each particles. Then, a technique for sectioning mulitple particles at once by polishing a composite comprising CIP particles in a hard-set epoxy was employed.

3.6.1 Focused Ion Beam Sectioning

Initially a focused ion beam (FIB) was used to section particles for individual assessment. The focused ion beam was configured for etching Si and was set to run an etch of the bounded box in Figure 3.10a to a depth of 100 nm with a beam current of 0.3 nA. The working distance was 4.3 mm, as this was the eucentric height, so tilting of the sample stage does not change the point of sample surface being imaged.

This program was run repeatedly until the particle had been cut through entirely, as in Figure 3.10b. Imaging of the cross-sections performed by this process did not show an internal structure Figure 3.10c. This could be from the ion beam causing carbon deposition onto the section surface, causing issues in imaging the structure [102].

It could also be possible that the structure is not being seen due to the materials of each layer being similar/ electrically connected, giving little contrast between the layers. In order to test this, the surface of a particle already cut in half was etched with the FIB. This was done by rotating the dualbeam stage after sectioning such that the face of the particle section was now perpendicular to the beam. The FIB was then used to perform a 50 nm deep etch of the entire surface before rotating back to view the newly polished section with the SEM Figure 3.11. The SEM was used for these images with an acceleration voltage reduced to 5.0 kV and beam current of 1.6 nA. The acceleration voltage for electrons was reduced as this gave a better contrast between regions at the cost of resolution. The improvement in contrast due to reduction of acceleration voltage is likely the result of incident electrons penetrating less deep into the surface of the section, meaning the images were more representative of the surface itself rather than any other

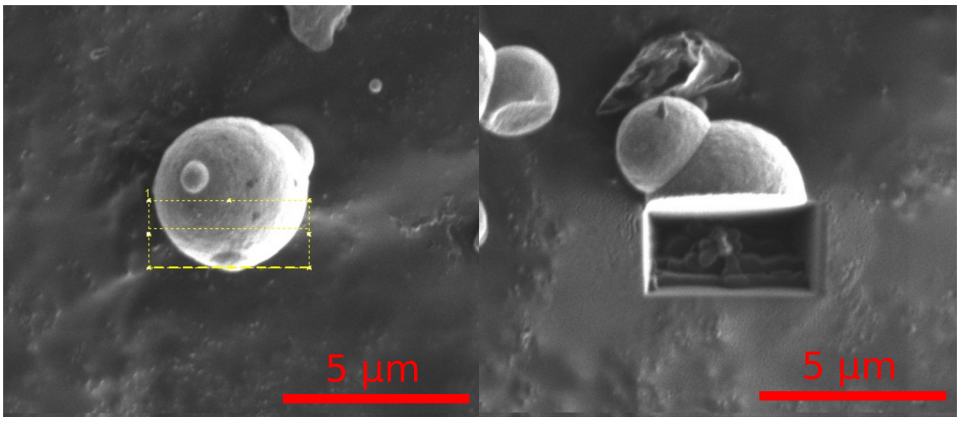

(a) (b)

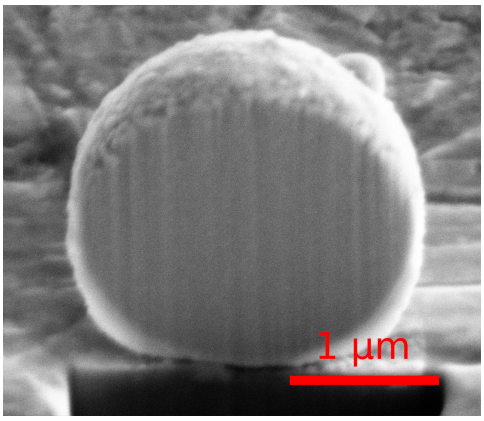

(c)

Figure 3.10: Figure demonstrating the process for attempting to image the section of a carbonyl iron particle by use of a dualbeam system. **(a)** First the particle is imaged and an area chosen to be cut by focused ion beam (FIB). **(b)** The FIB is used to section the particle, etching until all of the material has been removed. **(c)** Image the newly sectioned particle by scanning electron microscope. All images taken using SEM with acceleration voltage of 10.0 kV and beam current of 0.54 nA.

material below. For a structure that varies with depth, it is crucial to have an image of the section that is most representative of the surface whilst still having a high enough resolution to see features of interest. The detection mode for secondary electrons was also changed to through-lens-detection (TLD) as this detection method should allow a higher magnification for secondary electron detection, further improving the quality of image [103]. The secondary FIB polishing etch was intended to provide a topological difference between layers, rather than discerning by secondary electron energy alone; the two phases of the structure were expected to etch at different rates

under the ion beam meaning that after this process it should be possible to infer a structure Figure 3.12.

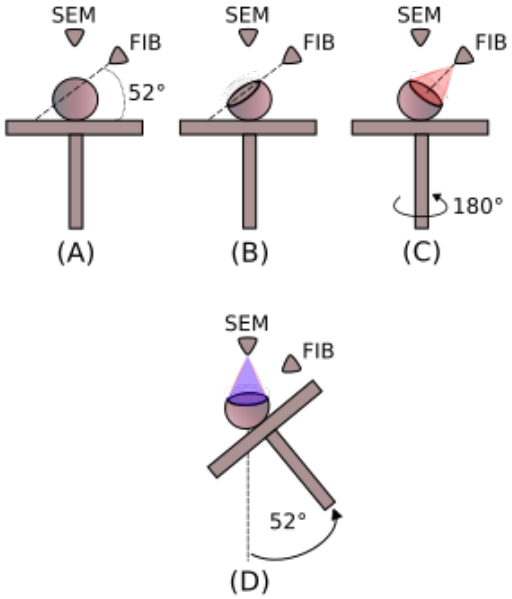

Figure 3.11: Schematic showing a method used in an attempt to inspect the internal structure of a carbonyl iron particle by use of a SEM-FIB dualbeam system. **(a)** First the particle is sectioned with the focused ion beam. **(b)** The particle is rotated such that the newly exposed section is perpendicular to the FIB. **(c)** FIB is used to polish the surface of the section. **(d)** Rotate sample and tilt such that the section is perpendicular to the SEM objective and image section.

Although this method appears to be viable for imaging the concentric ring structure of these particles, the process is laborious, only providing a single particle analysis per iteration of sectioning. The method also returned a low success rate, with particles often being lifted off the adhesive carbon tape before the section could be completed.

3.6.2 Sectioning by Polishing

The next method for producing cross-sections was by polishing the particles when set in a hard polymer matrix. Particles were enclosed in *Deluxe Materials Speed Epoxy II* epoxy resin before being sanded down to the region of loading. Once the region of loading was reached, the surface was then polished using *Hypres Five-Star* diamond compound emery paste loaded onto glass slides. The samples were polished with emery pastes with decreasing

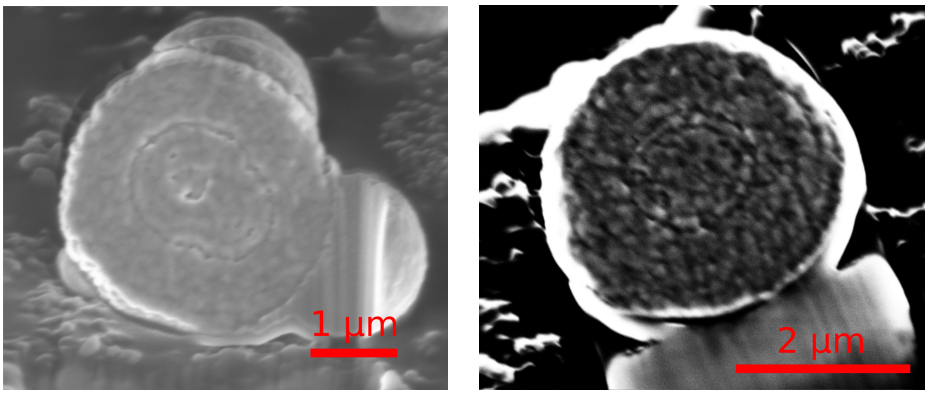

(a) **(b)**

Figure 3.12: This figure displays two high-contrast SEM images of the resultant section when using the dualbeam system with an additional polishing step applied by the FIB to etch the surface of the newly sectioned particle. Images taken with SEM using 5.0 kV acceleration voltage, beam current of 1.6 nA and through-lens-detection of secondary electrons.

particle sizes until a paste with 0.1 μm inclusions was used. The sample face was then cleaned in IPA for SEM imaging.

Imaging of this surface again proved ineffective for observing the internal structure, highlighting the issue that the entire structure of the particles is electrically conductive or the constituent parts of the internal structure are all too similar to be distinguished by SEM. A second process, described in [23] was then utilised. Nital, a metal etchant comprising 2%vol. nitric acid in IPA, was applied to the surface of the mechanically polished section. This etchant allows grain boundaries to be exposed topologically, as the etchant will etch different materials at different rates. This is applicable for exposing the onion ring structure of the particles, as the iron-carbide and pure iron layers will etch at different rates. This is the method predominantly used for obtaining the cross-section of CIP particles.

3.7 Particle Size Analysis

The particle size distributions for CIP grades were taken multiple times using two methods. The first attempt, by laser light diffraction was performed at Oxford, the second by Johnson Matthey (JM) using laser light diffraction again, and a third at The University of Exeter which was performed by directly imaging the particles by SEM. The SEM images were used to analyse the areas of the particles to infer a radius for each particle of a sample set.

3.7.1 Laser Light Diffraction Analysis

The analyses performed at Oxford and Johnson Matthey both utilised a *Malvern Instruments Mastersizer 2000* particle size analyser. The powders were mixed into a water suspension and ultrasound sonication was applied to the suspension to break agglomerates and ensure a good dispersion of particles. To obtain reliable, measurements of the particle sizes from this method it is necessary to make a solution that does not have too much powder as the more particles are in the solution, the less laser light will pass through the solution to give data on particle sizes. It is also possible to have extra scattering terms when the amount of particles is too high. The loss of signal due to scattering and absorption will cause the data to be unreliable, as multiple scattering terms cause erroneous extraction of particle size, while a low transmitted light level will lead to increased uncertainty. The optimum loading for small particles (less than 4 μm in size) corresponds to a percentage of obscured light of around 10% [104]. Once this amount of obscuration had been reached, the analysis was run.

3.7.2 SEM Analysis

SEM analysis of particle sizes was performed by taking a sample of each grade and adhering them to a strip of carbon tape before blowing the surface with compressed air. This allowed particles to be reasonably well dispersed, without areas that were too dense in particles for the image processing software to be able to recognise them as individual particles. It is also necessary to ensure particles are not too sparse on the imaging surface to avoid an excessive amount of images needing to be processed for a complete analysis. An example image for particle size analysis is shown in Figure 3.13a.

Particles were imaged using the SEM/FIB dual beam system described in Chapter 2. The acceleration voltage for imaging was 10.0 kV with an emission current of 0.13 nA. The working distance between electron source and sample was 5.0 mm.

Once particles had been imaged, a 3rd party imaging software, *ImageJ*, was utilised for particle size analysis. First, images are converted into binary format, with particles shown as solid black on a white background, as in Figure 3.13b. Once images had been converted to binary format, a watershed function was applied to automatically split particles that were touching, allowing individual particles to be detected. The particle analysis function was then applied, looking only for particles with a diameter greater than 0.03 μm and below 100 μm with a circularity greater than 0.6. The circularity for the image of a particle is defined by the ratio of the area of image occupied by the particle, and the perimeter of the image of the particle squared (3.18). This ratio is normalised such that a circularity of 1 corresponds to a 1:1 ratio circle. Once particles had been detected and their sizes taken as an area of pixels, the data was analysed to infer a particle radius in μm.

$$\text{Circularity} = 4\pi \cdot \frac{\text{Area}}{\text{Perimeter}^2} \tag{3.18}$$

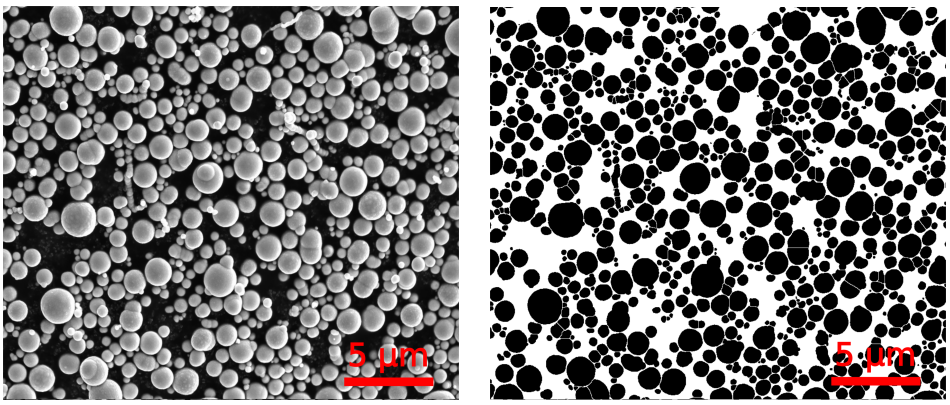

(a) **(b)**

Figure 3.13: **(a)** SEM micrograph example for particle size analysis of CIP HQ. **(b)** Processed image for use in particle detection and area extraction. The image has had a binary function applied to convert the image to purely black and white pixels, and a watershed function has been applied to separate regions of joined particles.

3.8 List of Materials

- CIP ES obtained from *BASF*
- CIP HQ obtained from *BASF*
- CIP HS obtained from *BASF*
- CIP EW obtained from *BASF*
- CIP EW-I obtained from *BASF*
- CIP EM obtained from *BASF*
- CIP CM obtained from *BASF*
- CIP SM obtained from *BASF*
- 800 nm spherical Fe powder obtained from *S S nano*
- 100 nm spherical Fe powder obtained from *S S nano*
- Xencast P2 Fast Cast Polyurethane Casting Resin obtained from *Easy Composites*
- Speed Epoxy II obtained from *Deluxe Materials*
- 2% Nital Etchan obtained from *Vickers Laboratories*
- PTFE powder obtained from *Sigma-Aldrich*
- $BaTiO_3$ powder obtained from *Sigma-Aldrich*

3.9 Conclusions

In this chapter, a method for fabrication of composite samples is discussed, alongside another experimental technique for the preparation of composites with filtered particle size distributions. The optimisation routine for the stripline transition region is discussed and S-parameters for the optimised stripline, as well as the final geometry converged upon are discussed in the next chapter. The optimised stripline geometry presented in Chapter 4 is that which has been used for the entirety of this project. The calibration

technique developed in this project has been detailed, alongside the analytical theory representing this calibration technique and the improvements in measurement that have been applied. The calibration technique has been adapted from previous literature, and improvements to the technique are presented. These improvements allow the characterisation of transition regions across an unprecedented broadband frequency range of 200 MHz - 50 GHz. The method for imaging the size and structure of CIP particles is also presented here, and the results of the particle size distributions for each CIP grade investigated are presented in Chapter 5.

The following chapters will detail experiments performed using this improved stripline measurement technique.

Chapter 4

An Improved Stripline Technique for the Electromagnetic Characterisation of Composite Materials

4.1 Introduction

To provide a full investigation into CIP-PU composites, a method for quickly and easily characterising multiple samples with different volume loadings of material was required. This technique needed to be viable for use with small samples as not to create unnecessary waste of constituent materials and also required a sample geometry that was able to be readily produced in bulk for validation of repeatability. As described in Chapter 2, most other techniques require multiple samples for different frequency bands of characterisation and often require samples whose geometry makes it difficult for bulk amounts of samples to be produced easily (for example, toroidal samples for coaxial line require metalisation of the inner hole that may not be easily achieved in bulk). The optimised stripline technique presented in this chapter, and used throughout the rest of this work, is viable for the characterisation of dielectric and magnetodielectric materials across an unprecedented frequency range of 200 MHz – 50 GHz for single samples. The samples are cut from a stock with a total volume of only 3.2 cm^3 that can be cut into a minimum of 5 sample pairs with different propagation lengths for characterisation. For comparison, a similar characterisation by waveguide across the significantly narrower frequency range 12.4 – 18 GHz, would require a volume of stock that is 8.7 cm^3 to produce the requisite sample set.

This chapter contains results for the optimised stripline geometry when modelled in a finite difference time domain electromagnetic modelling software. The final solution converged upon is presented, alongside comparisons of the modelled and measured S-parameters for this proposed stripline geometry. The results for extraction of sample S-parameters from measurements of the stripline geometry with dielectric and magnetic composites is then presented. From these measured S-parameters, the relative permittivity and permeability is extracted. This chapter also provides an outline of different methods that may be used for the extraction of relative permittivity for dielectric materials that allow either a fit to the full frequency range of measured S-parameters for samples or a point-by-point approach, analysing narrower "windows" of frequencies.

The results for extraction of relative permittivity and permeability of magnetic composite materials containing carbonyl iron powder in polyurethane are also presented. This chapter also contains a discussion of the typical errors associated with the stripline technique when measuring dielectric and magnetic samples, and is the technique that has been utilised for the extraction of material parameters that are presented throughout the rest of this work.

4.2 Method

4.2.1 Electromagnetic Modelling of Stripline Transmission Lines

Stripline geometries were electromagnetically modelled using a finite difference time domain simulation software. The stripline geometry was first modelled and the S-parameter results compared to a standard 20° taper stripline. The stripline that was modelled had dimensions of $H = 7$ mm, $W = 10.66$ mm and $L_{\mathrm{Cav}} = 10$ mm. The modelled S-parameters, displayed in Figure 4.1, matched closely with results measured experimentally, confirming the validity of this model. There are extra oscillations in the measured S-parameters of the stripline, which are a result of impedance mismatch between the coaxial cables and the coaxial adaptors of the stripline. This mismatch is not incorporated into the model of the striplines so these oscillations are not present in the model output. Once the stripline model

had been verified, different geometries were able to be chosen in order to increase the working range of the device.

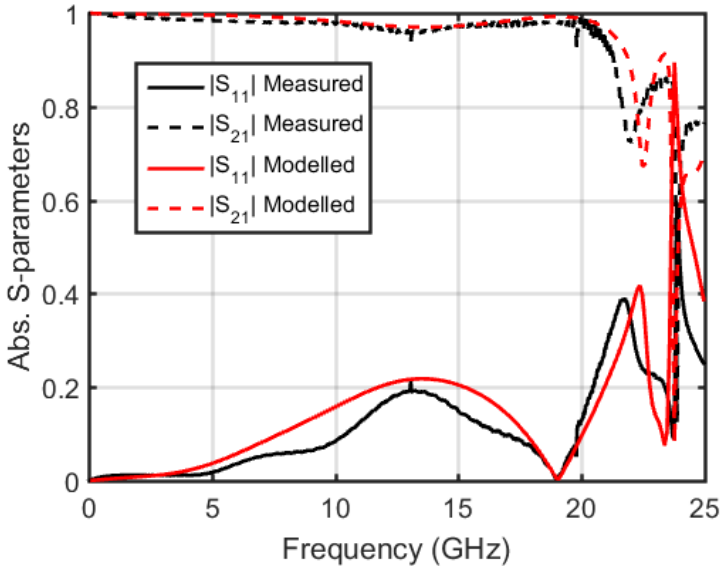

Figure 4.1: Comparison of modelled and measured S-parameters for an empty stripline geometry.

4.2.2 Upper Cut-off of Stripline

There exists an upper cut-off for the stripline above which non-TEM modes exist. These modes corrupt S-parameter data such that Fresnel theory may no longer be applied to determine permittivity and permeability of samples. The upper cutoff of the stripline appears to be a result of the height discontinuity of the line at the coaxial to strip transition. This frequency at which cutoff occurs is dependent on both the height and length of the stripline, meaning when high index materials are used in the stripline, this cutoff can unfortunately be brought down into the frequency range of interest. For these reasons it was important to design a stripline with a cutoff that is high in frequency, such that adding high index materials will not bring the unwanted resonance down to the frequency range of interest.

Figure 4.2 shows the measured and modelled S-parameters for a 7 mm tall stripline with a 5.54 mm Teflon sample inserted. There is a non-TEM mode at around 22 GHz for the empty stripline, which is brought down to a frequency of 17 GHz when the Teflon sample is inserted. This mode

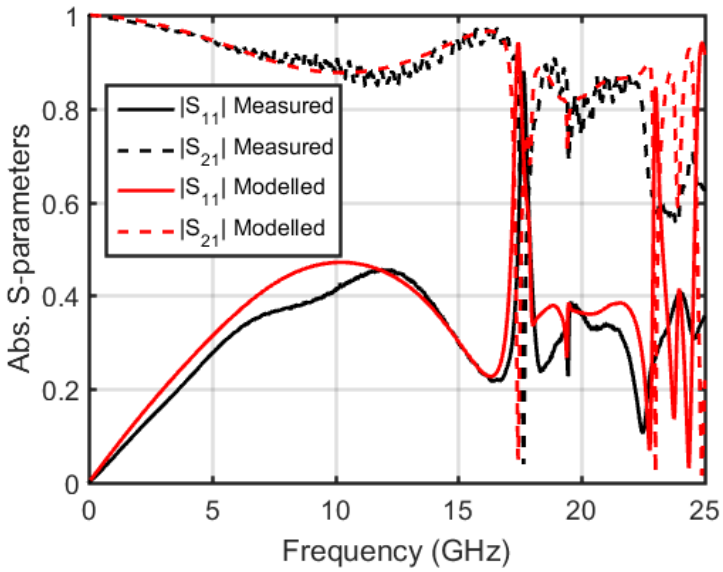

Figure 4.2: Comparison of modelled and measured S-parameters for a stripline geometry with a 5 mm Teflon sample inserted.

cannot be accounted for by Fresnel theory, so extraction of permittivity and permeability for a sample is not possible at the frequency of resonance.

By reducing the propagation length of the line, as well as the cavity height, the frequency of this mode is pushed higher. However, it was recognised that once the height of the cavity matched the diameter of coaxial adaptors, this mode was suppressed, and an upper cut-off that was not dependent on the propagation length of the cavity was left. The stripline cavity height used was 3 mm, with a strip width of 3.86 mm and thickness 0.15 mm. The single angle taper transition of the strip width was set to 20°. The modelled S-parameters of this stripline are shown below and the observed cut-off for this stripline was at $\sim$ 49 GHz.

A second optimisation was performed to produce a new transition region geometry that allowed better impedance matching than a simple 20° taper. The process for this optimisation is discussed next.

4.2.3 Optimization of the Stripline Conductor Geometry

The impedance of the improved stripline was optimized by adjusting the shape of the center strip transition regions. Using an electromagnetic model of the ends of the stripline with a general shape comprising 10 vertices, a genetic algorithm was used with HFSS modelling software to minimize the

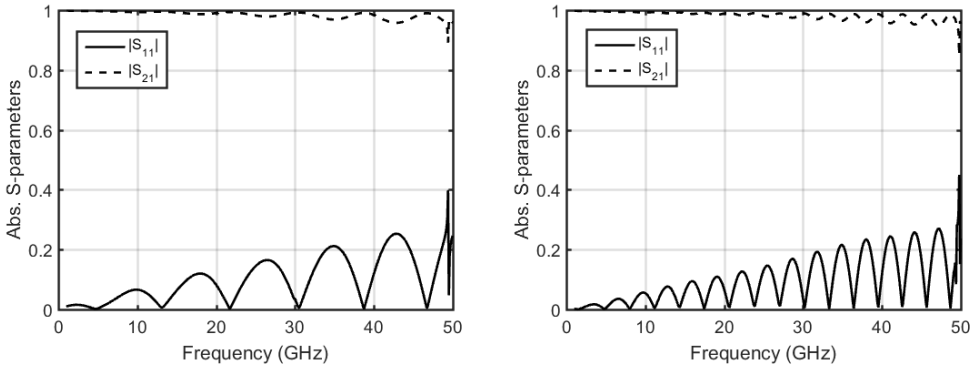

Figure 4.3: Figure showing the absolute S-parameters for a stripline device with single angle taper transition, height of 3 mm and strip width of 3.86 mm. The cavity lengths for each model were **(a)** 20 mm and **(b)** 50 mm.

reflection, S_{11}, and maximize transmission, S_{21}. A finite element method (FEM) analysis was utilised for this optimisation, and an in-built optimisation utility was used for applying a genetic algorithm to the objective function. The final geometry converged upon was approximated with a smooth curve that gives the relationship between width, w, of the line, and distance along the line, x. This transition region ends at a given length, L_{Trans}, and is repeated on the other end of the strip for transition back to the coaxial adapter. The final geometry used is described by Equation (4.1)

$$w = \begin{cases} r_0 & \text{for } x \leq d \\ r_0 + A\sqrt[3]{x-d} & \text{for } d \leq x \leq L_{\text{Trans}} \\ 3.83 \text{ mm} & \text{for } x \geq L_{\text{Trans}} \end{cases} \tag{4.1}$$

Here r_0 is the radius of the coaxial pin, and A is a scaling factor, which when optimised takes a value of 0.01 and x is the distance along the line, in mm. Using a stripline geometry with height, H = 3 mm, and cavity length of L = 20 mm the optimum transition regions begin at a distance, d, from the cavity wall of 0.22 mm and finish at a distance from the cavity wall of L_{Trans} = 2.49 mm. Between the transition regions, the width, w, remains constant at 3.83 mm. Schematics showing the stripline, center strip geometry and sample placement, alongside a photo of the fabricated stripline are shown in Fig. 4.4. The central conductor thickness, t, is 0.15 mm.

The modelled S-parameters for this geometry of stripline are displayed

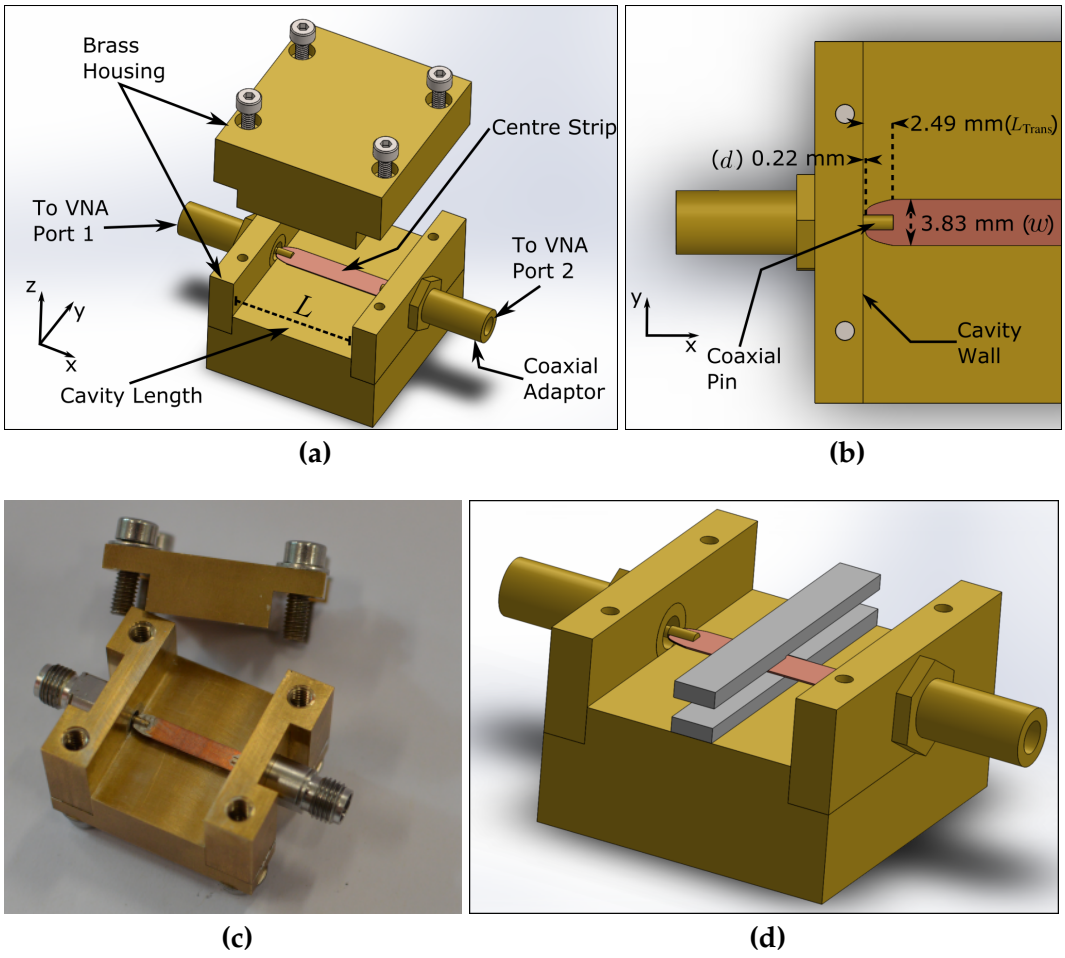

Figure 4.4: (a) Schematic showing the stripline geometry. Coaxial adapters screw into the walls of a brass housing, and the center conducting strip is connected using coaxial pins. (b) Close-up schematic of the transition region from coaxial pin to central strip shape. (c) Photograph of the stripline device. (d) Schematic showing the sample placement in the stripline. Samples are placed above and below the central conductor such that the step in each sample is either side of the line.

in Figure 4.5. The absolute reflected signal, $|S_{11}|$ is seen to remain below 0.1 across the range 70 kHz - 50 GHz. The measured S-parameters for the fabricated stripline are shown in Figure 4.6. As can be seen, there is considerably more reflection for the fabricated line than the model predicts. This is likely due to the characteristic impedance of the coaxial adapters being modified when machining them to be flush with the stripline cavity walls, as damage may be caused to the connectors at this time. It is also possible that there are other imperfections in the fabricated stripline during assembly. The need to

solder coaxial pins to the central conducting strip introduces another possible source of impedance mismatch.

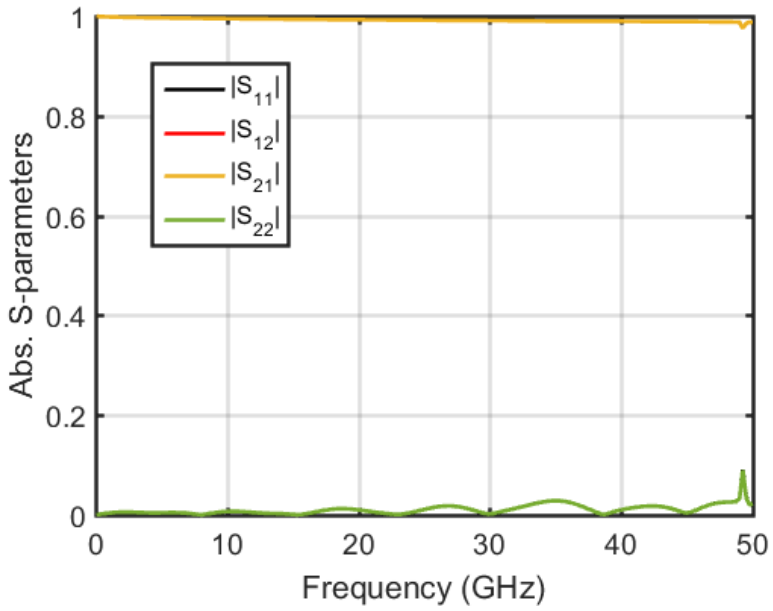

Figure 4.5: Graph showing the modelled S-parameters for the optimised stripline

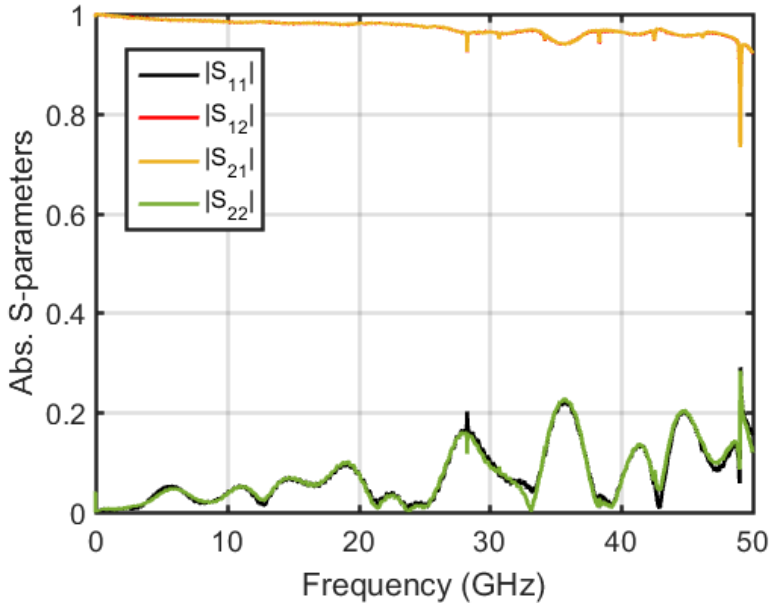

Figure 4.6: Graphs showing the measured S-parameters for the optimised stripline.

To test the transition regions for the stripline cavity were a general solution for any length of cavity, the length of the stripline cavity was changed in

model. When changing the length of the cavity from 20 mm to 150 mm, provided the transition regions were the same, no affect of the S-parameters of the stripline in models were noted any further than an increase in the number of Fabry-Perot modes across the frequency range. This test was used to prove that the transition regions of the stripline were a solution for the height of that line, and that it was independent of the length of the stripline cavity. There is a mode in the modelled stripline at 49 GHz that is also present in the measured S-parameters for the stripline. This mode does not change in position when changing the length of the stripline cavity, as seen in Figure 4.7 where a model of the same stripline transition regions were used with a cavity length of 50 mm. The discrepancy in reflection amplitudes for the manufactured stripline compared with the modelled stripline presents the issue of requiring a calibration technique to account for reflections at the transitions. However, since there are no higher order modes up until 50 GHz, the short calibration technique described in Chapter 3 is applicable.

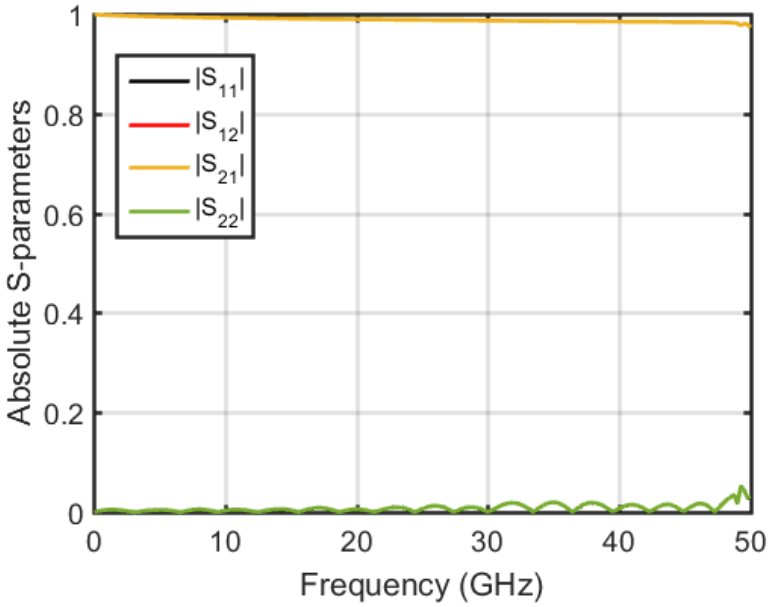

Figure 4.7: Graph showing the modelled S-parameters for the optimised stripline geometry with a cavity length of 50 mm.

The height of the stripline cavity is rather more critical as the 'Short' bars and samples must fit snugly into the stripline. If shorts and samples do not fit snugly into the line, air gaps will cause erroneous data extraction. It was

also found that air gaps between the cavity walls and lid of the stripline allow extra non-TEM modes to be excited. These air gaps may be as small as tens of microns and still cause issue in calibration. To minimise the prevalence of these issues, the joins of the lid to the cavity walls were sealed at the bottom with conductive paste, and where air gaps at the top were persistent, toolmaker's clamps were used for sealing.

Other dimensions for the stripline were changed such as the width of the center conductor and thickness of the conducting line. This will cause the S-parameters for the stripline to become sub-optimal. Provided no non-TEM modes are able to be supported, the secondary 'Short' calibration accounts for these extra reflections caused by impedance mismatch. The inverse relationship between the frequency at which higher order modes appear and the stripline height was investigated by testing extraction of S-parameters for samples inserted into striplines with the same central conductor but different heights. The different heights returned the following result: 3 mm tall stripline operation up to approximately 50 GHz, 10 mm tall operation up to approximately 17 GHz, 15 mm tall operation up to approximately 10 GHz, and 20 mm tall operation up to approximately 5 GHz.

Another source of error in measurement is the incorrect placement of samples or the use of samples that are misshapen. The sensitivity of measurement to sample placement and quality is investigated more thoroughly in the results section of this chapter.

4.2.4 Sample Fabrication

In order to test the design of the proposed stripline, samples were made with increasing index that were either only dielectric, or contained magnetic inclusions for testing simultaneous extraction of permittivity and permeability. Samples were fabricated by mixing dielectric or magnetic powder into a polyurethane resin using the technique described in Chapter 3. Multiple samples with specific values for l_{Sam} were fabricated. Characterisation of samples with different lengths is useful when characterising samples with low loss as by measuring multiple lengths of sample, it is possible to provide more information at frequencies corresponding to Fabry-Perot resonances within the samples.

Dielectric composite samples were formed with percentage volume fillings of $BaTiO_3$ ranging from 0% vol. to 25% vol. in 5% vol. increments.

(The $BaTiO_3$ was obtained from *Sigma Aldrich*, where the given particle size was ≤ 3 μm.) Magnetic composite samples were formed with percentage volume fillings of CIP ranging from 0% vol. to 40% vol. in 10% vol. increments. The carbonyl iron used was grade CIP ES from BASF with a particle size range 3.0 – 4.0 μm, as stated by *BASF*. CIP particles tend to be spherical and have a smaller size distribution, meaning the mixture in resin was less viscous than with $BaTiO_3$ particles, thus a higher percentage volume filling was reached. The densities of these samples as a function of percentage volume filling are shown in Fig. 4.8.

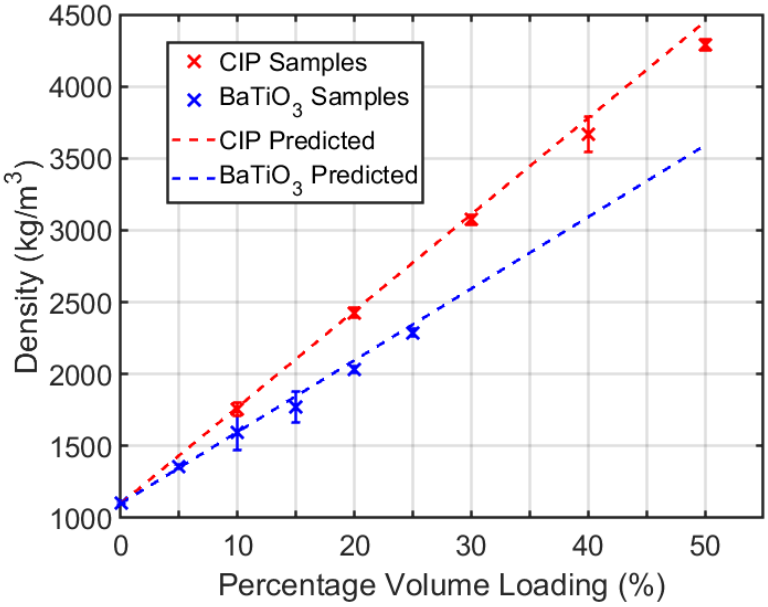

Figure 4.8: Measured densities of CIP ES – Polyurethane (red) and $BaTiO_3$ – Polyurethane (blue) composites for each percentage volume loading. Dashed lines show the predicted densities with ρ_{CIP}=7800 kg/m^3 and ρ_{BaTiO_3}=6080 kg/m^3

The linear relationship between composite density and % volume loading indicates that samples contained negligible amounts of air bubbles. The predicted densities for the samples were calculated by using a density for CIP of ρ_{CIP}=7800 kg/m^3 and for the dielectric samples using a density for $BaTiO_3$ of ρ_{BaTiO_3}=6080 kg/m^3. These are the stated densities of the materials in the MSDS, taken at 25 °C.

4.2.5 Measurement Process

Measurements were taken using the following procedure:

- Perform standard SOLT cable calibration with VNA;
- Take 7 readings of S_{11} and S_{22} with 'shorts' placed at known different positions;
- Measure empty stripline S-parameters with and without calibration standards on each end;
- Fit to all 'short' readings and empty stripline readings to extract transition region S-parameters;
- Measure stripline S-parameters with sample inserted;
- Use transition region S-parameters to extract sample S-parameters;
- Fit to sample S-parameters with Fresnel theory to find values for relative permittivity and permeability.

The cables used to connect the stripline to the VNA were 60 cm long, 2.4 mm (V-Type) cables. The coaxial adapters from circular to stripline geometry were 2.92 mm - 2.4 mm adapters (K-Type to V-Type).

4.3 Results

4.3.1 Dielectric Composites

The measured S-parameters for the 3 mm tall stripline system with a pure polyurethane sample inserted are displayed in Figure 4.9. The polyurethane sample was 5.05 mm in length, and the S-parameters for the sample alone, after de-embedding with the calibration technique, are shown in Figure 4.10. These S-parameters have also had a phase correction applied to set the reference plane of the data to be at the sample interface.

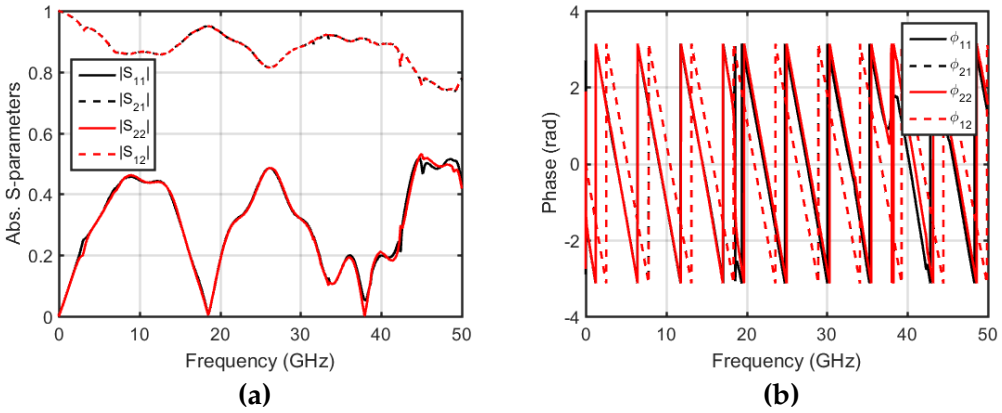

Figure 4.9: Magnitude **(a)** and phase **(b)** for the measured S-parameters of the stripline transmission line with a 5.04 mm pure polyurethane sample inserted.

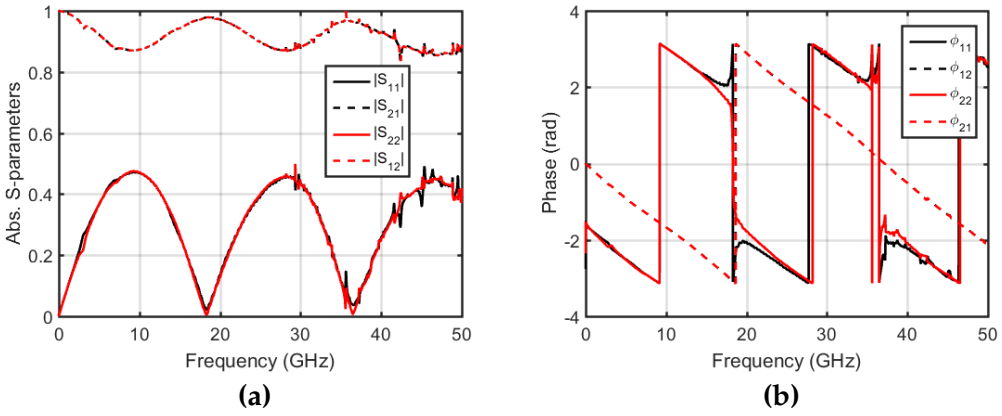

Figure 4.10: Magnitude **(a)** and phase **(b)** for the extracted sample S-parameters for a 5.04 mm pure polyurethane sample, extracted from the measured S-parameters for the combined system.

The comparisons of Figure 4.9 and Figure 4.10 shows that the effects of extra reflections at the transition regions of the stripline have been removed, and the reference positions for the phases of the reflected and transmitted signals have been set to the faces either side of the sample. These S-parameters were fit to by the sliding window Fresnel method described in Chapter 3. The results for relative permittivity and permeability, as well as the corresponding values for refractive index and characteristic impedance are shown in Figure 4.11.

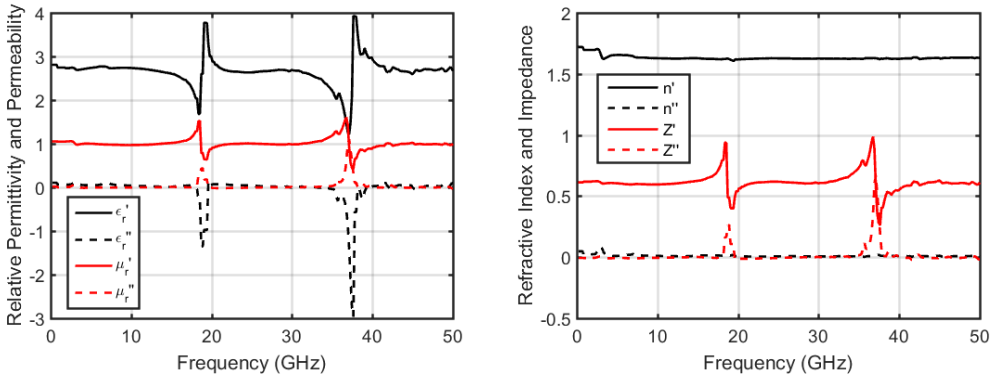

(a) **(b)**

Figure 4.11: Relative permittivity and permeability **(a)** with the characteristic impedance and refractive index **(b)** for the 5.04 mm pure polyurethane sample, extracted by fitting to S-parameters with Fresnel's equations and ϵ_r, μ_r as free variables.

There are spikes in the data that occur at frequencies corresponding to wavelengths where integer multiples of $\frac{\lambda}{2}$ fit into the sample ($\frac{\lambda}{2}$ frequencies). When plotting the refractive index and impedance from this result, it is possible to see that the index remains stable across this frequency range, whereas the impedance contains the spikes. This is because the determined impedance of the sample becomes unstable at frequencies where the reflected signal is low, as there is a higher uncertainty due to noise in measurements. An expression for calculating the impedance explicity from the measured S-parameters is given in Equation (4.2).

$$Z_{\text{Calc}} = \sqrt{\frac{(1+S_{11})^2 - S_{21}^2}{(1-S_{11})^2 - S_{21}^2}} \tag{4.2}$$

By calculating the impedance explicitly and comparing with the impedance

resulting from the fitted parameters, it is seen that this error is still prevalent even when fitting to a range of points. The index, however, remains stable across the entire frequency range. Since the sample is assumed to be a dielectric, it is possible to assume that the impedance is given by Equation (4.3)

$$Z_{\text{Fit}} = \frac{1}{n_{\text{Fit}}} = \frac{1}{\sqrt{\epsilon_r \mu_r}} \tag{4.3}$$

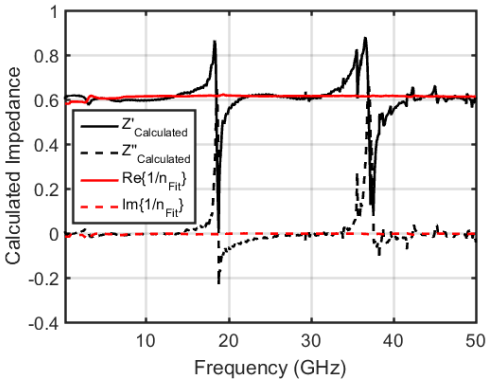

Figure 4.12: Characteristic impedance of the polyurethane sample, directly calculated from Equation (4.2) (Black), compared with the characteristic impedance inferred from the fitted index (Red).

It is also possible to apply the assumption that $\mu_r = 1$ for these samples during the fitting routine. When fitting to the S-parameters with only the permittivity as the free variable, the results in Figure 4.13 are converged upon.

The results for the relative permittivity of $BaTiO_3$ loaded samples, extracted by fitting Fresnel theory to sample S-parameters with the relative permeability fixed at unity, are shown in Fig. 4.14.

There is a weak oscillation in the data, which is associated with the increased error in S-parameter measurements at $\frac{\lambda}{2}$ frequencies. The roughness or shape of sample at one face can also differ from the other side, which adds further to the uncertainty at these points. Much care is taken to ensure sample dimensions are all square but there will inevitably be errors. At higher volume loadings, the impedance and loss of samples is such that the magnitude of S_{21} becomes close to zero at high frequencies, again leading to increased uncertainties at high frequencies.

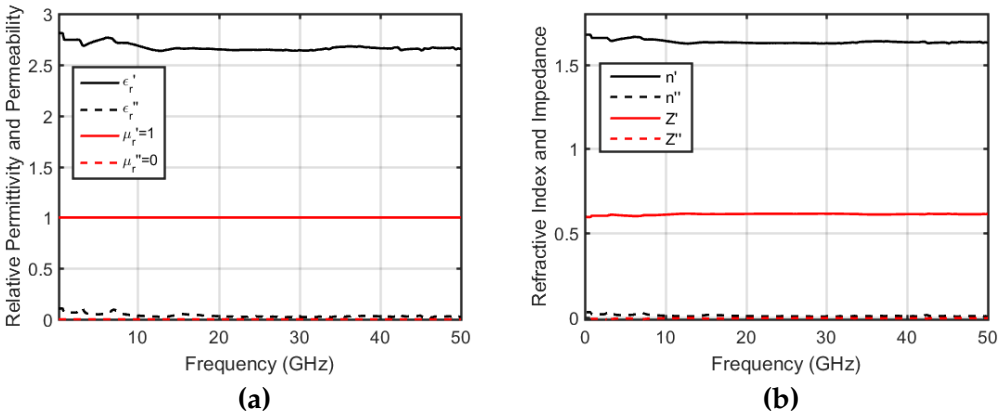

Figure 4.13: Relative permittivity **(a)** with the characteristic impedance and refractive index **(b)** for the 5.04 mm pure polyurethane sample, extracted by fitting to S-parameters and imposing $\mu_r = 1$.

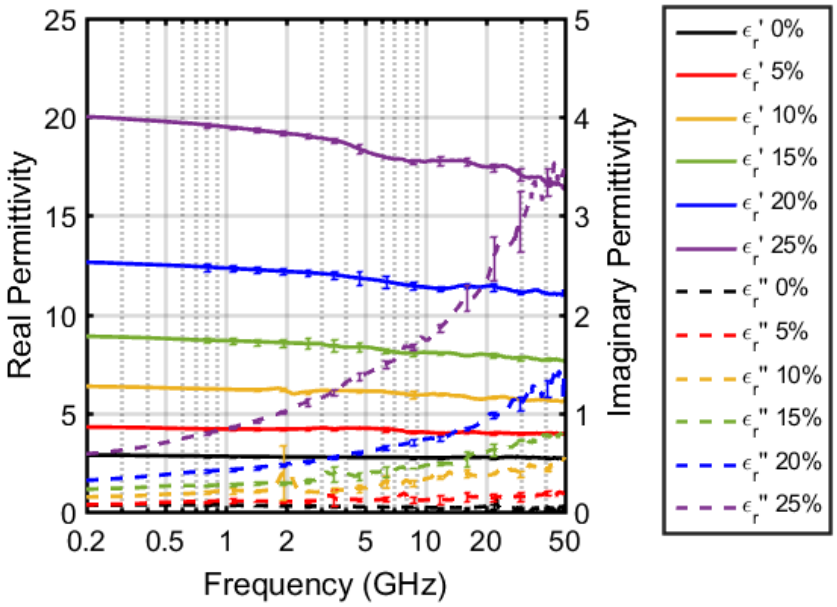

Figure 4.14: Relative complex permittivity for $BaTiO_3$ – Polyurethane composites with increasing percentage volume of $BaTiO_3$.

To test the sensitivity in measurement to these possible errors, models for the measurement of samples that were not ideal were performed. The results of this modelling are discussed next.

4.3.2 Sample Placement in the Stripline

In order to test how robust the stripline measurement technique was with regards to sample placement and sample quality, models were run with samples that had been deliberately placed incorrectly in the stripline. The samples modelled were dielectric samples, with a relative permittivity of ϵ_r=10 + 5i and propagation length of 4.00 mm. Errors in sample placement that were tested were;

- Sample placement mismatch of 0.5 mm, Figure 4.15a
- Sample propagation length mismatch of 0.5 mm, Figure 4.15b
- Samples rotated 1° from parallel, Figure 4.15c
- Sample interface not perpendicular to wave propagation. Figure 4.15d

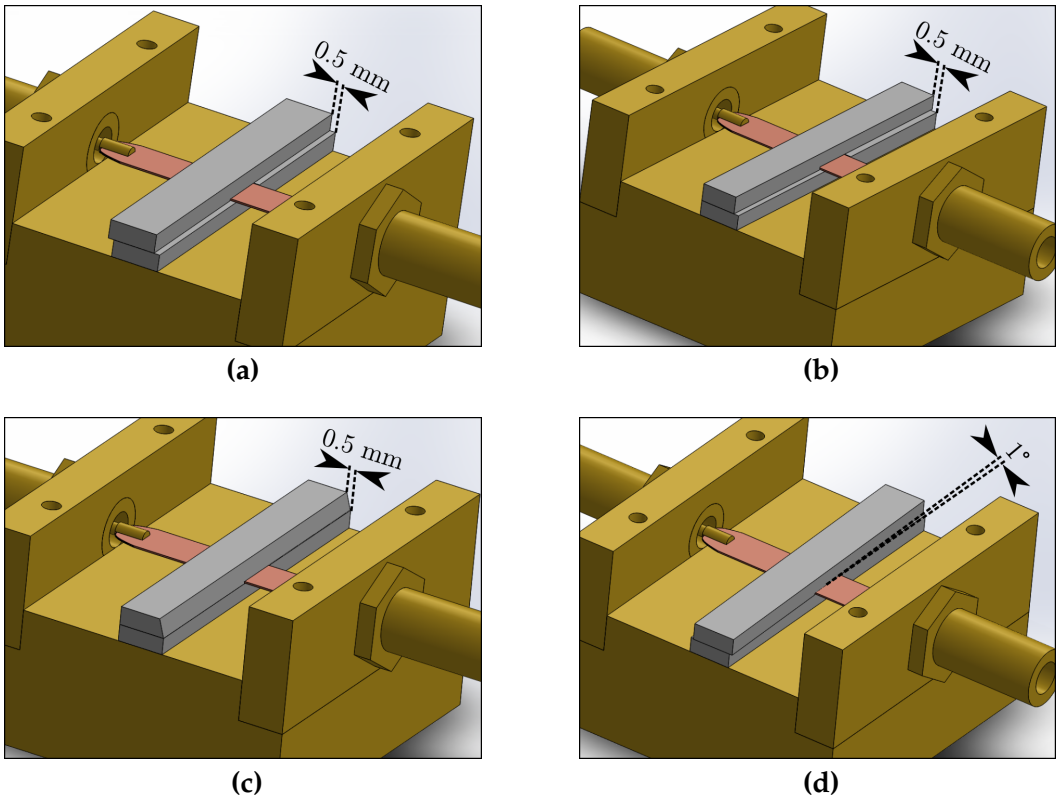

Figure 4.15: Schematics showing erroneous sample placements that were modelled **(a)** Mismatch in sample positioning **(b)** Mismatch in sample propagation lengths **(c)** Chamfered sample interface **(d)** Sample rotation mismatch.

All models were performed using *HFSS*, and a set of short measurements were also modelled for the empty stripline such that an identical S-parameter correction may be applied as in the experiment. The extracted sample S-parameters for these samples are compared with those modelled analytically for an ideal sample in free space. The relative permittivity was extracted from these modelled S-parameters and is displayed in Figure 4.16. There were erroneous extractions at frequencies where Fabry-Perot resonances occur. This is due to the reflection and transmission amplitudes being different from those expected when samples do not have faces that match up perfectly. There is also an error in the phase of these S-parameters, as the effective length of samples is modified by errors in sample placement or manufacture.

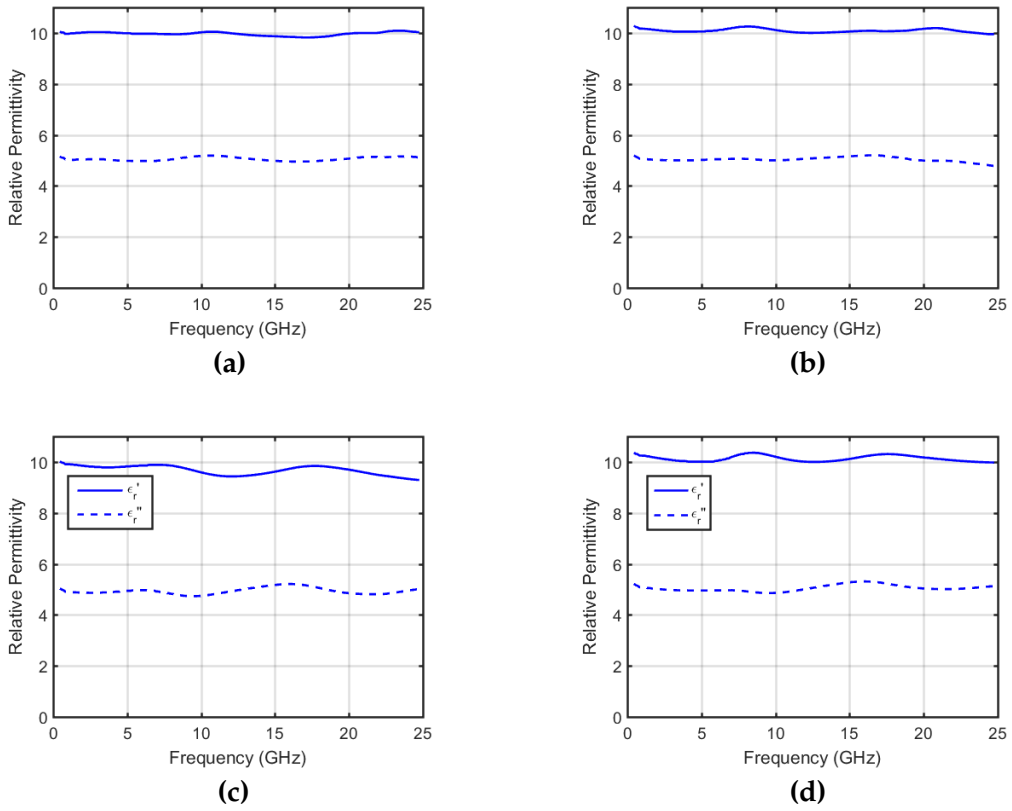

Figure 4.16: Graphs showing extracted relative permittivities for sample measurements with the following placement errors **(a)** Mismatch in sample positioning **(b)** Mismatch in sample propagation lengths **(c)** Chamfered sample interface **(d)** Sample rotation mismatch.

The results of this modelling highlight the need to manufacture samples with accurate dimensions that match within pairs. The error in extraction

associated with samples that have a chamfered interface show the typical error expected when samples have cracked or rough faces. By comparing the S-parameters for an ideal sample with propagation length 3.75 mm to those modelled for a sample propagation length mismatch, it was noted that the effective length of this modelled sample had been reduced to the mean propagation length of the sample pair. However, the reflection amplitude at the mismatched interface differed from that on the opposite, matching side.

4.3.3 Frequency Dependent Expression of Relative Permittivity

In order to give higher reliability to relative permittivity results for dielectric characterisation, a frequency dependent model for the permittivity was assumed. The equation used for relative permittivity as a function of frequency is described as a single Debye resonance, given by Equation (4.4). Here, ϵ_∞ is the permittivity at frequencies that may considered infinite, ϵ_s the permittivity at zero frequency, τ is the relaxation time of the dielectric material [105]. The value for permittivity at infinite frequency was assumed here to be unity.

$$\epsilon_r(F) = \epsilon_\infty + \frac{\epsilon_\mathrm{s} - \epsilon_\infty}{[1 + (iF\tau)]} \tag{4.4}$$

Equation (4.4) was used to fit to the entire frequency range of S-parameters measured for the 5.04 mm pure polyurethane sample. In order to allow better accuracy in the fit, there were extra terms added in the fit that allowed the length of the sample to vary within measurement tolerances to account for error in sample length measurement, as well as the offset position of the sample. Figure 4.17 shows the measured and fitted S-parameters when using this frequency dependent expression for relative permittivity.

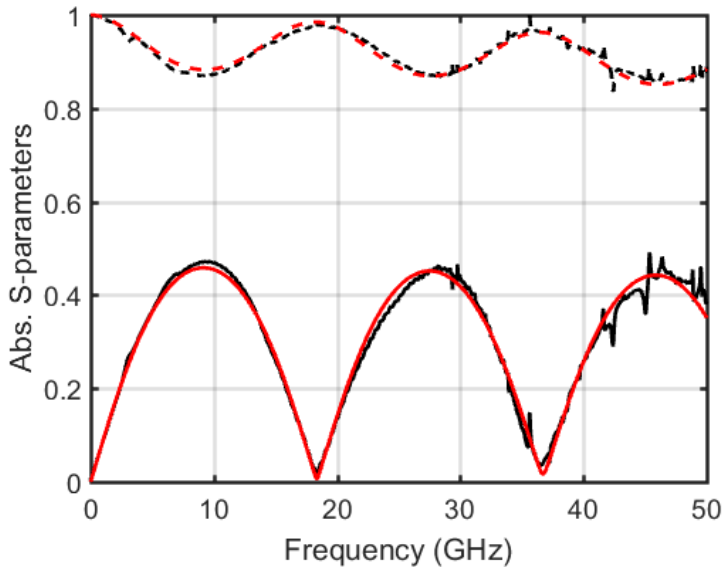

Figure 4.17: Graph showing the measured S-parameters for a pure polyurethane sample (Black) compared with the fitted S-parameters using Equation (4.4) to model the frequency dependent permittivity inserted into Fresnel equations.

The measured and fitted S-parameters shown in Figure 4.17 fit closely across the whole frequency range. The resulting values for fitting parameters are shown below, and the resulting relative permittivity is displayed in Figure 4.18a

- $\epsilon_s = 2.71 + 0.018i$
- $\tau = 1.79 \times 10^{-13}$ s
- $\Delta t = 0.01$ mm
- $\Delta x = -0.09$ mm.

here, Δt and Δx are the fitting parameters to allow a tolerance in the thickness of the sample, as well as the offset of the sample, respectively.

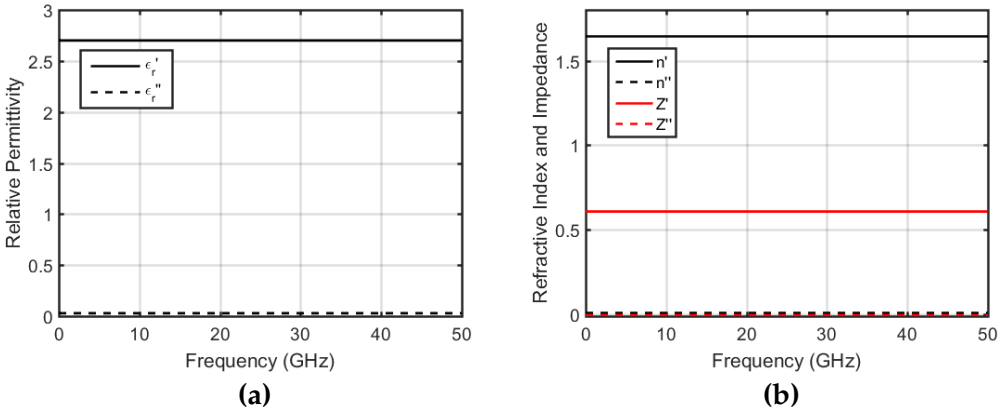

(a) **(b)**

Figure 4.18: Relative permittivity **(a)** with the characteristic impedance and refractive index **(b)** for the 5.04 mm pure polyurethane sample, extracted by fitting to S-parameters when imposing $\mu_r = 1$ and assuming that the permittivity has the frequency dependence, given by Equation (4.4).

The corresponding values for index and impedance when using this fit are shown in Figure 4.18b and it is clear that the issue with impedance being unstable at Fabry-Perot resonances is now resolved.

This method for fitting to dielectric samples was applied to the S-parameters measured for the $BaTiO_3$ samples. The results for extracted relative permittivity are shown in Figure 4.19. The model only assumes a single dielectric resonance for the composite samples, as well as the pure polyurethane sample. This is because the loss of pure polyurethane is so low that it is expected to be negligible compared with the $BaTiO_3$ loading.

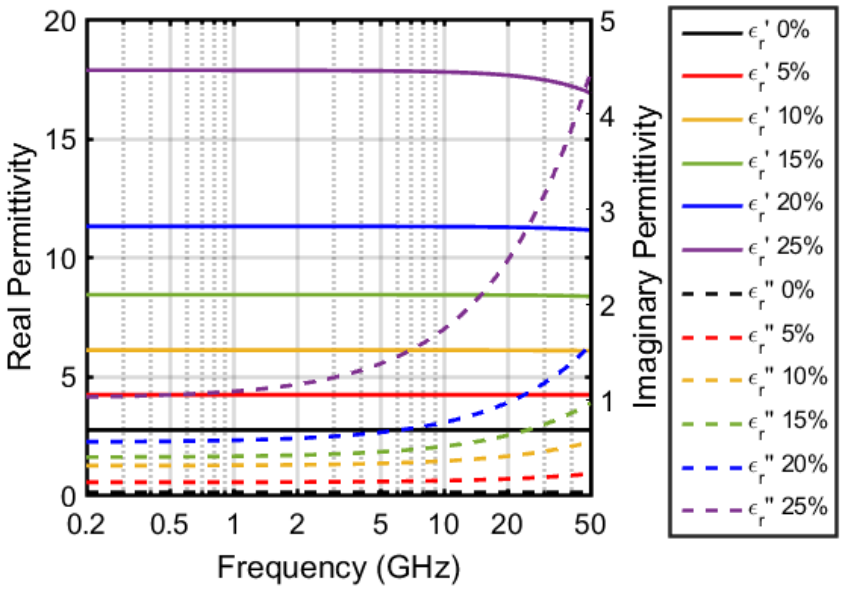

Figure 4.19: Relative permittivity for $BaTiO_3$ samples, extracted using the Debye model of frequency dependent permittivity. Samples had volume loadings from 0%vol. - 25%vol. in 5%vol. increments.

The converged values for the fitting terms used to create these permittivites are displayed in Table 4.1.

	5%vol.	10%vol.	15%vol.	20%vol.	25%vol.
ϵ_s	4.20+0.13i	6.08+0.30i	8.41+0.39i	11.25+0.55i	17.85+1.01i
τ	5.7 $\times 10^{-13}$	9.9 $\times 10^{-13}$	15.6 $\times 10^{-13}$	20.2 $\times 10^{-13}$	43.2 $\times 10^{-13}$

Table 4.1: Table showing the values for static permittivity, ϵ_s, and relaxation time, τ, that were converged upon when fitting to material S-parameters for $BaTiO_3$ – polyurethane composites.

The real part of relative permittivity shows an approximately linear dependence on the logarithm of the frequency, as is expected for a dielectric material [106–109]. In addition, the static permittivity of samples at low frequency (200 MHz) increases logarithmically with % volume loading (Figure 4.20). The logarithmic increase in permittivity with percentage volume loadings agrees with the simple Lichtenecker mixing equation for a relative real permittivity of $BaTiO_3$ of 5700, and for polyurethane of 2.86 [110]. These values were found by fitting to the static values of the logarithm of real permittivity as a function of percentage loading.

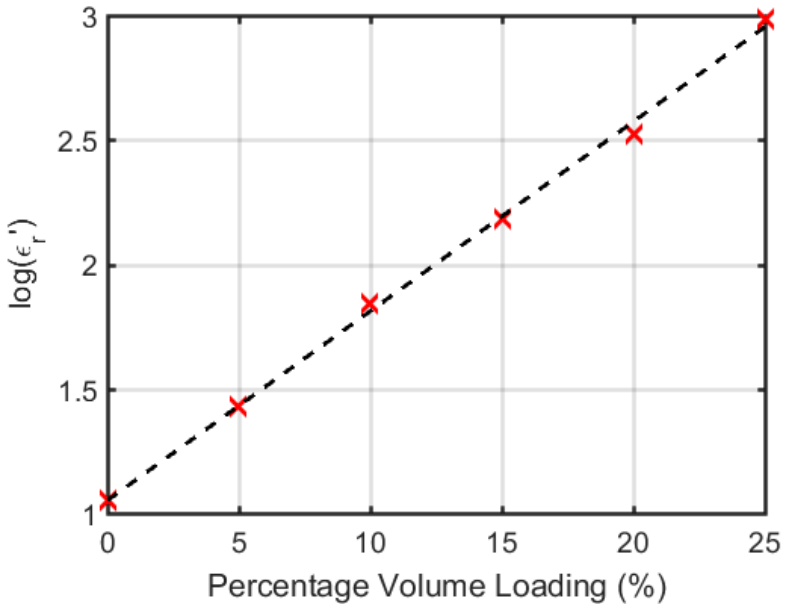

Figure 4.20: Natural log of the real part of relative permittivity at 200 MHz for $BaTiO_3$ – Polyurethane composites with increasing percentage volume of $BaTiO_3$. The dashed line shows a linear fit to the data.

4.3.4 Magnetic Composite Parameter Extraction

From the results in the previous subsection, it is apparent that accurate values for relative permittivity may be obtained over a wide frequency range for pure dielectric materials with μ_r=1. However, we are also interested in composites with a non-unity value of permeability. Using the same technique without assuming $\mu_r = 1$ or fitting with Equation (4.4), the results for relative permittivity and permeability of samples loaded with CIP ES are shown in Figure 4.21 and Figure 4.22. The relative permittivity and permeability of these samples at 200 MHz also increase logarithmically with percentage volume loading (Figure 4.23). A broad peak in the imaginary permeability from 1 GHz to 30 GHz, which increases in intensity with percentage loading is also recorded. The absorption peak is primarily associated with the ferromagnetic resonance (FMR) of iron, which occurs at a frequency close to 2 GHz. The absorption peak is broadened by the presence of higher order spherical modes in the particles [25, 33, 63, 111]. The size of these particles is such that the higher order spherical modes occur at frequencies similar to the FMR mode. Due to the particle size distribution of this CIP, these modes are also broadened and overlap the FMR mode to give a wide absorption band. It is possible that there are also conductive losses in these composites. Inter- and intra- particle conduction will contribute losses in permeability due to eddy currents [112]. These losses would be expected to increase with the square of frequency. However, since the size of the particles is so small, the eddy current loss may be assumed to be insignificant. In addition, the percentage loading of these composites is low, meaning the total eddy current losses in these composites should be negligible in comparison to the ferromagnetic losses.

There is a systematic error associated with the height of samples not completely filling the cavity of the stripline. This will have a similar effect to what happens in coaxial measurements when the sample fails to fill the entire cavity in that the extracted permittivity of samples will appear low. Samples were cast in a mould such that their height is accurate to within 20 μm and silver conductive paste was painted on the faces of the samples touching the outer conductors to remove the source of systematic error. However, there may also be air gaps between samples at the central conductor and between the sample interfaces at the center. These errors are difficult to estimate due again to roughness of the samples however it is

known that the error will reduce the determined permittivity. It is also difficult to remove air gaps between sample interfaces at the center of the line, as conductive paste may not be used to seal these gaps.

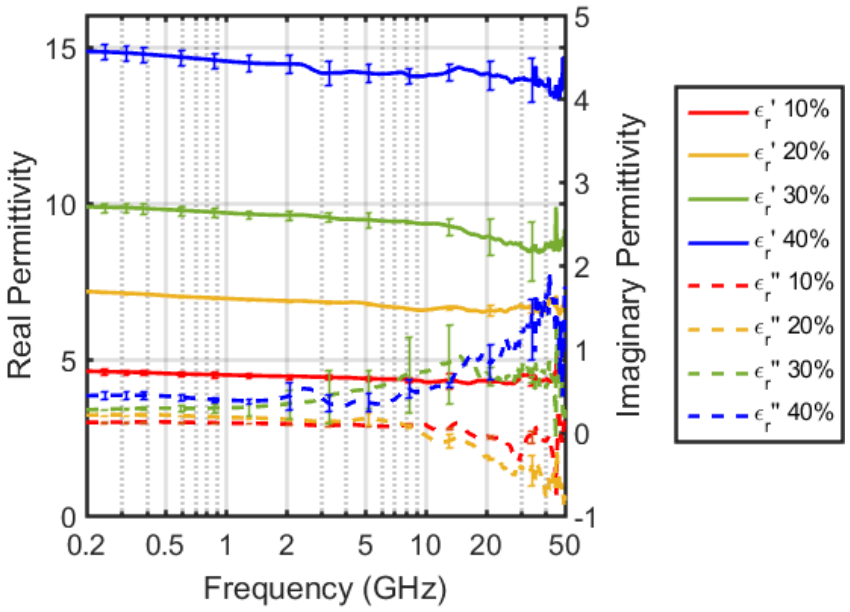

Figure 4.21: Relative complex permittivity for CIP ES – Polyurethane composites with increasing percentage volume loading of CIP.

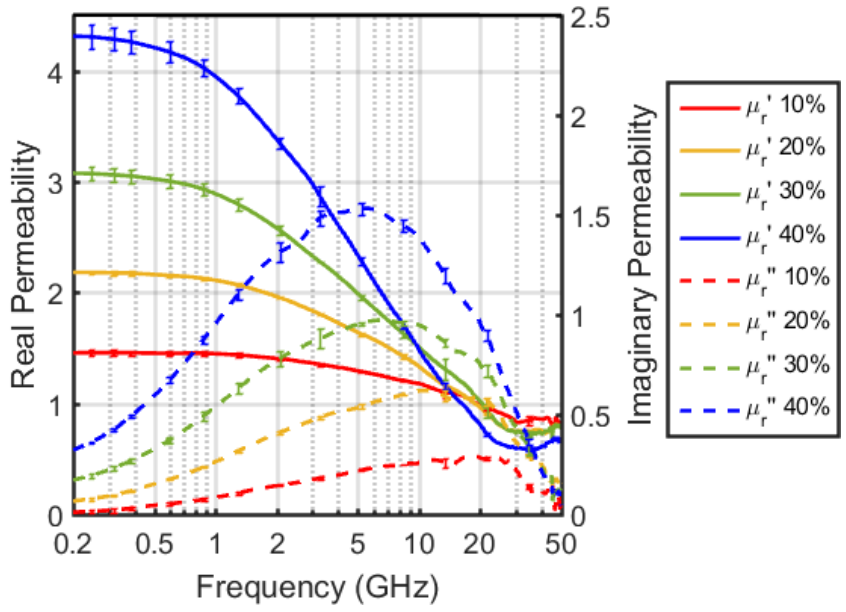

Figure 4.22: Relative complex permeability for CIP ES – Polyurethane composites with increasing percentage volume loading of CIP.

From modelling it is found that the permeability is affected less by air gaps at the top and bottom cavity interfaces than it is by gaps at the center of the cavity between samples. This is likely due to the electromagnetic field being concentrated at the central strip of the device, meaning the circulating magnetic field is more likely to be affected by air gaps in this region. The systematic error in permittivity from modelling a sample with 20 μm height discrepancy was found to be approximately 3% and the systematic error in permeability for a similar air gap along the center of the cavity was found to be only of the order of 1% however, there is again the introduction of oscillations at the Fabry-Perot frequencies. This oscillation error appears in both permeability and permittivity extractions, with the base value of the permittivity changing very little from the original value.

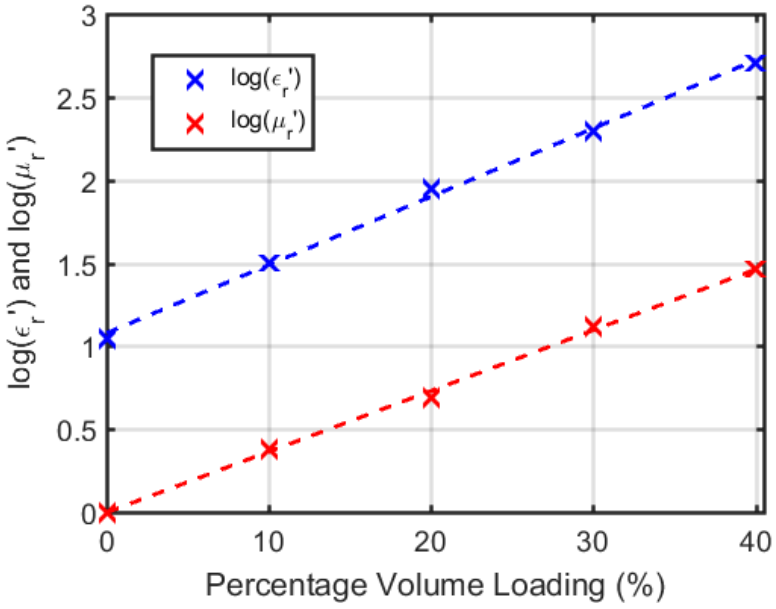

Figure 4.23: Natural log of the real parts of relative permittivity and permeability at a frequency of 200 MHz, as a function of percentage volume loading for CIP – Polyurethane composites. The dashed lines show the results of a least squares, straight line fit to the data.

There are apparent absorption modes in the relative permittivity for these samples at high frequencies. When looking at the refractive index resulting from the permittivity and permeability, displayed in Figure 4.24, these absorption modes do not appear. However, there are oscillations in the impedance data displayed in Figure 4.25. These oscillations are seen more strongly for the lower loadings of magnetic material, at higher frequencies when the permeability it low. It is likely that these absorption peaks in the

permittivity data are fake and are a result of the degeneracy in impedance at these $\frac{\lambda}{2}$ frequencies as seen in dielectric samples when fitting with a free permeability.

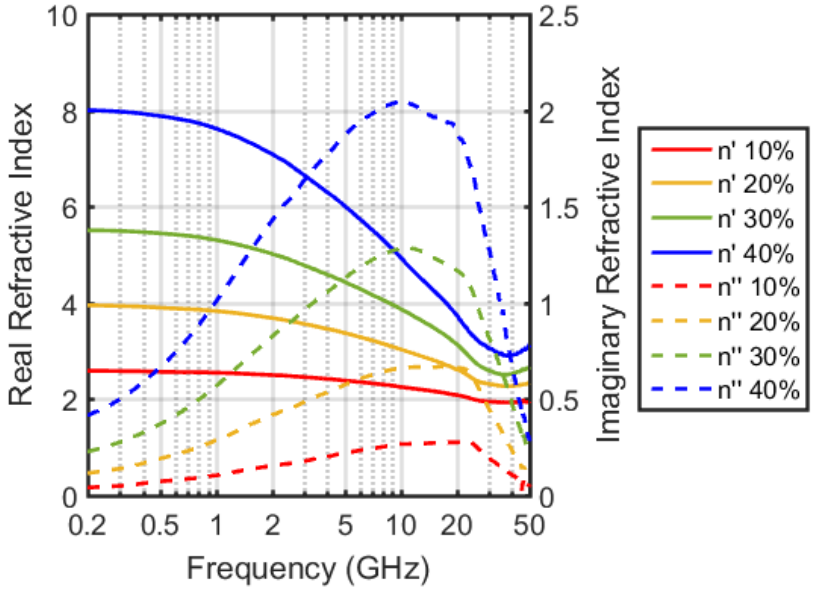

Figure 4.24: Refractive index for CIP ES – polyurethane composites with volume loading across the range 10%vol. - 40%vol. in 10%vol. increments.

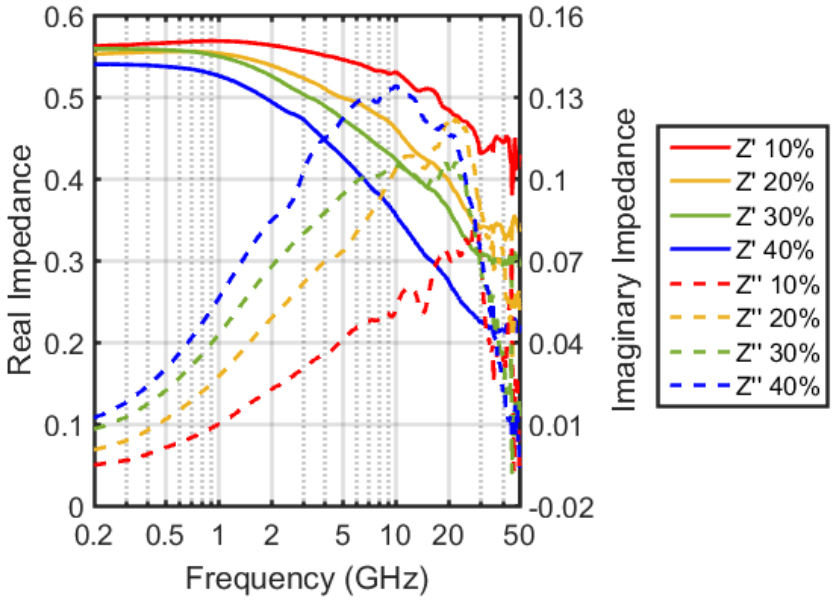

Figure 4.25: Impedance for CIP ES – polyurethane composites with volume loading across the range 10%vol. - 40%vol. in 10%vol. increments.

An attempt was made to fit to the S-parameters for these magnetic samples using a frequency dependent expression for both the permittivity and permeability. However, the fits to these S-parameters had many local minima, meaning it was not possible to converge on a final solution. The expression for the frequency dependent permeability of the samples was expressed in terms of a single Debye resonance to describe the FMR mode, with extra Lorentzian terms summed to account for multiple resonances as in [33, 113].

Since the refractive index for samples is seen to be more resistant to erroneous extraction at $\frac{\lambda}{2}$ frequencies, it is this data that will be primarily displayed throughout the thesis. An Argand plot of the refractive index, which may be referred to as a Cole-Cole plot for purely dielectric materials [114], gives better information on the absorption modes seen in these composites. Since the relative permittivity is not expected to exhibit resonances across the frequency range of interest, a Cole-Cole plot of the refractive index will display essentially the magnetic absorption modes in the composites. A Cole-Cole plot of the refractive index for CIP ES composites is shown in Figure 4.26.

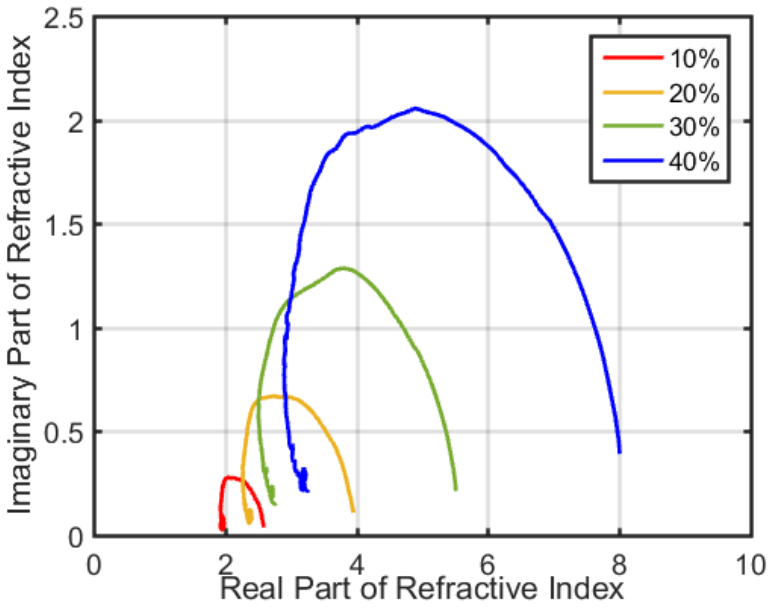

Figure 4.26: Cole-Cole plot of the refractive index for CIP ES – polyurethane composites with volume loading across the range 10%vol. - 40%vol. in 10%vol. increments..

The Cole-Cole plot of refractive index for these composites shows a similar shape for all loadings of magnetic material, indicating that the absorption mode in these composites is not dependent on the loading. This means that interactions between particles are able to be neglected for composites with loadings up to 40%vol.

4.4 Broader Frequency Characterisation of Composites

The investigation of higher order modes in spherical powders is not limited to investigation of carbonyl iron powders. Spherical nanopowders and hollow magnetic shells are of interest as the reduction in size for nanoparticles should, in theory, push the resonance frequency of spherical modes even higher. A recent study at The University of Exeter by C. McKeever has shed light on new even higher frequency modes that are supported in spherical shell particles at frequencies well above 30 GHz [14]. The results of this study are not yet published. With this knowledge in mind, it is necessary to begin reaching further for higher frequency, more broadband characterisation techniques of composite materials.

It is possible to apply a novel waveguide technique for high frequency characterisation. An experimental setup for high frequency measurements was accessed at The National Physical Laboratory (NPL). This experiment involves the use of a VNA with frequency extender attached that leads to a waveguide for propagation. There is a lens at the end of the waveguide transmission line that converts the supported wave into a free-space plane wave. This plane wave is then incident on the sample under test and transmission and reflection are measured. This experimental setup is similar to [115] and [116]. The frequency range investigated in this experiment was 150 - 210 GHz and other frequency conversion units were available for measurement at higher and lower frequencies.

Low-loss dielectric samples of PTFE and Polyurethane were measured, and the recorded S-parameters are displayed in Figure 4.27. All samples were fabricated as square-faced obloids with dimensions of 50 mm $\times$ 50 mm $\times$ T, where $T \geq 3$ mm. The propagation length of these samples is T. These samples are again simple in geometry, meaning sample manufacture was less difficult than is required for other techniques.

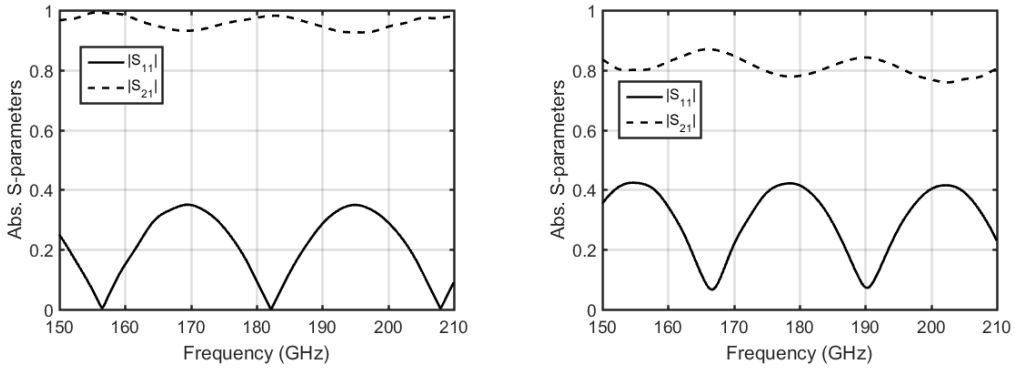

Figure 4.27: Graphs showing the measured S-parameters for **(a)** a 4 mm PTFE sample and **(b)** a 3.9 mm pure polyurethane sample.

From these S-parameters, relative permittivity was to be extracted. Due to the high frequency at which these measurements start, there is a range of local minima in the objective function for the fit to S-parameters due to the degeneracy in phase as it is unknown how many 2π phase cycles had occurred before reaching the measurement range. For this reason, the low frequency measurement of dielectric samples taken with the stripline device were fitted to simultaneously with the high frequency measurements. The experimental results were fitted to with the Debye theory described previously in this chapter. Relative permittivity for these dielectric samples are shown below, with a comparison of the measured and fitted S-parameters displayed in Figure 4.29 and Figure 4.30.

It was also necessary to add again a tolerance in the thickness and position for fitting to these S-parameter measurements. This meant adding a second pair of fitting parameters for the fit to each thickness of sample at low and high frequency. The tolerance in thickness at low frequency for the stripline measurements was Δt_1, with the tolerance in offset of the sample as Δx_1. For high frequency measurement by the planar freespace measurement, the tolerances in thickness and offset were Δt_2 and Δx_2, respectively. At high frequencies, the knowledge of the thickness and offset to a high precision is crucial as the wavelength is significantly smaller.

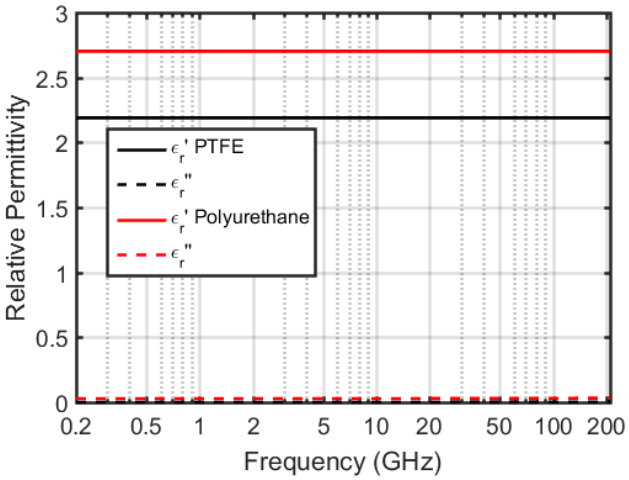

Figure 4.28: Graph showing the relative permittivity for polyurethane and PTFE across the frequency range 0.2 - 210 GHz.

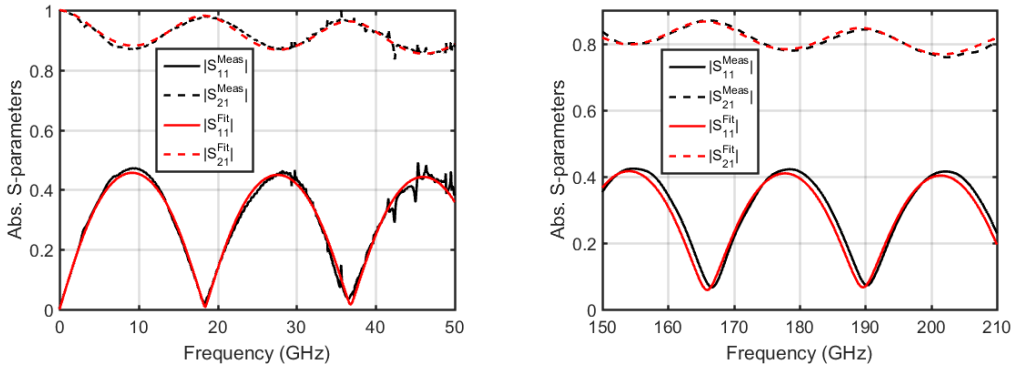

(a) **(b)**

Figure 4.29: Graphs showing the measured (Black) and fitted (Red) S-parameters for polyurethane samples measured across the frequency ranges **(a)** 0.2 - 50 GHz and **(b)** 150 - 210 GHz.

The resultant parameters for fitting to the set of S-parameters for the pure polyurethane samples are as follows:

- $\epsilon_s = 2.70 + 0.029i$
- $\tau = 1.21 \times 10^{-14}$ s
- $\Delta t_1 = -0.01$ mm
- $\Delta x_1 = -0.08$ mm.
- $\Delta t_2 = -0.01$ mm

- $\Delta x_2 = 0.01$ mm.

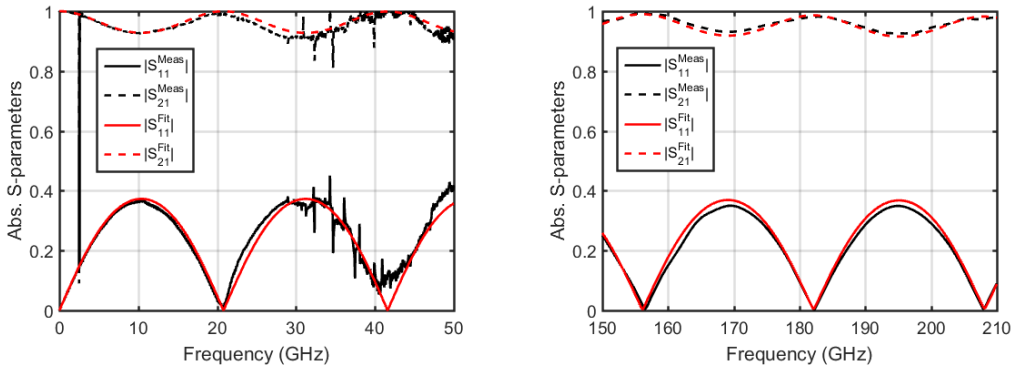

Figure 4.30: Graphs showing the measured (Black) and fitted (Red) S-parameters for PTFE samples measured across the frequency ranges **(a)** 0.2 - 50 GHz and **(b)** 150 - 210 GHz.

The resultant parameters for fitting to the set of S-parameters for the PTFE samples are as follows:

- $\epsilon_s = 2.19 + 0.000i$
- $\tau = 1.16 \times 10^{-14}$ s
- $\Delta t_1 = -0.18$ mm
- $\Delta x_1 = 0.03$ mm.
- $\Delta t_2 = -0.18$ mm
- $\Delta x_2 = 0.03$ mm.

Measurements were also taken for a composite comprising 20%vol. CIP ES in polyurethane. These S-parameters, however, were not able to be fitted to at this time. An expression for the frequency dependent permeability has not yet been utilised for reliably fitting to S-parameters. When attempting to use a frequency dependent expression for permeability, there are too many fitting parameters for a reasonable fit to be repeatably converged upon.

4.5 Chapter Summary

The relative complex permittivity for $BaTiO_3$ – polyurethane composites has been determined across the frequency range 200 MHz – 50 GHz for samples containing 5% – 25%vol. loading of dielectric filler. The relative complex permittivity and permeability for carbonyl iron – polyurethane composites at different volume loadings of carbonyl iron is also determined. The results demonstrate that this method can be used to measure the effective permittivity and permeability for composite materials across the frequency range 200 MHz to 50 GHz and is viable for materials with refractive index at least as high as 8. This measurement technique has an unprecedented frequency range of operation, and is viable for characterisation of both dielectric and magneto-dielectric materials.This method is used throughout the thesis to present investigations into the absorption properties of composites comprising CIP particles in polyurethane.

The stripline geometry has a height of 3 mm, a cavity length of 20 mm and a central strip width of 3.82 mm. It has been fabricated with transition regions that have been optimized to favor impedance matching. S-parameter measurements taken with this device have been calibrated using an improvement on the triple-short technique which involves the use of seven 'short' readings rather than three. By fitting to seven 'short' readings, the frequency range over which the application of this calibration technique, adapted from [26] has been increased such that there are no longer frequencies at which the calibration fails, related to the spacing of each 'short' reading. This allows a single set of calibration readings to be used that have a wide separation of the first and final 'short' reading, allowing greater reliability at the bottom end of stripline operation while still being valid across broadband frequency ranges.

The stripline technique presented here requires significantly less stock material for characterisation of sample sets, with the total mass of carbonyl iron used for ths investigation being of the order of 40 g. An equivalent investigation into multiple sample batches of the same volume loadings using a 12-18 GHz waveguide would require around 75 g of material, and would require exponentially more as lower frequencies were investigated. A set of samples for coaxial measurement across the frequency range 100 MHz – 18 GHz, assuming the central hole had been drilled rather than cast, would require around 65 g of material. To investigate higher frequencies would

require samples with infeasibly small and accurate dimensions. Most materials of interest for measurement at these higher frequencies come in limited batch amounts, at typically 100 g. The reduction of waste when characterising these materials is of great importance.

This device will have excellent utility in upcoming research as the interest in broadband devices increases, and the investigation of materials extends from UHF/VHF applications to dual-band and multi-band applications that extend well into the GHz regime [117–120]. It will become necessary to characterise novel materials for use in the substrates of these devices to further improve their performance.

Chapter 5

Broadband Characterisation of Carbonyl Iron Powder – Polyurethane Composites

5.1 Introduction

To investigate the relationship between a specific grade of CIP's physical properties and corresponding electromagnetic properties, a reliable method for characterising the average particle size and microstructure for the particles was required. This chapter presents an alternative method for particle size analysis that is not the typical laser diffraction method. This method, using SEM image analysis, can be used for reliable particle size analysis when powders are smaller than 1 μm in size. A comparison of the results for particle size distributions obtained through this method and by laser diffraction at two different institutes is presented and shows that the image analysis method used in this work returns results for particle size distributions that have significantly more sub-micron sized particles than seen through the laser diffraction technique. The results from particle size analysis of the as-received CIP grades compared with extracted electromagnetic properties showed that the size distributions were too broad to be able to perform a concise investigation into higher order spherical modes in magnetic powders. However, a distinct change in the magnetic absorption for different sized powders was still observed for powders of the size order 1 μm. The distribution of particle size was also seen to be a significant factor to consider when characterising spherical powders, as powders with significantly narrower size distributions exhibited sharper magnetic absorption modes at high frequencies.

A comparison of "hard" and "soft" CIP grades was also attempted in this chapter. However, when observing the cross-sections of CIP particles, it was discovered that there existed particles with a polycrystalline structure and particles with an onion-like structure in even the same grade of CIP. It was also observed that these structures had a wide variation in the way they were manifest. Some polycrystalline particles would have a small grain size of the order of 100 nm, while others would have large grain structures of the order of 1 μm. The same variation in domain sizes was observed for onion-like particles. In previous investigations into CIP properties, most literature assumes the size distribution and existence of microstructure match the description provided by the supplier. This work shows it is necessary to check the powder properties when explicitly comparing grades.

As discussed previously, the production of carbonyl iron powder is essentially a dual chemical reaction. Firstly there is a thermal decomposition of iron pentacarbonyl into iron and carbon monoxide, as in Equation (5.1). There then follows a second reaction causing the formation of carbon from this excess carbon monoxide, as in Equation (5.2). Alternation between these two processes results in the onion-like structure that most CIP grades possess. It is possible to tune the particle size distribution of a grade of CIP by changing the amount of time that the powders are condensed for, or by sifting the particles after production. It is also be possible to tune the number and thickness of layers in a grade of powder by changing the environment in the chamber. Changing the environment in the chamber may affect the balance between the chemical processes and may shift favor towards iron production Equation (5.1) over carbon production Equation (5.2), or vice versa. Other reactions take place during production which lead to oxygen and nitrogen being incorporated into CIP particles [18, 83, 121]. This can lead to large variations in the final product and highlights the need to analyse many grades of CIP to see how certain factors in production can affect the electromagnetic properties of these composites.

$$\mathrm{Fe(CO)_5} \longrightarrow \mathrm{Fe} + 5\,\mathrm{CO} \tag{5.1}$$

$$2\,\mathrm{CO} \longrightarrow \mathrm{C} + \mathrm{CO_2} \tag{5.2}$$

Once a grade has been produced, it is possible to change the properties further. For example, sintering the particles may remove the internal structure, reducing the internal structure from onion-like to polycrystalline. Particles may also be coated to reduce the effects of oxidation or to reduce surface charge effects and change their electromagnetic properties further. This coating is typically a phosphate coating [81, 122].

In this chapter, we investigate fabrication processes for different CIP grades and explore the difference of particle size, internal structure, and coating on their electromagnetic properties.

5.2 Method

5.2.1 Particle Cross-section Analysis

Particle cross-sections were taken for particles using the method described in Chapter 3, Section 3.6.2. The SEM imaging of these sections were taken using an acceleration voltage of 10 kV, beam current of 0.13 nA and a working distance of 5.9 mm. The working distance for these samples was higher than usual as the epoxy composites holding the sectioned particles were $\sim$ 5 mm tall and a compensation to the stub had not been applied. This did not affect the resolution of images.
The magnification ranged from $35000\times$ – $50000\times$.

5.2.2 Particle Size Analysis

SEM Analysis

The analysis of the particles was performed by inferring the radius of each particle from its area before counting the amount of particles falling within specified bins of size. The SEM images for this analysis were taken using the method described in Chapter 3, Section 3.7. The size bins were chosen to be from 0.1 – 5 μm with widths of 0.05 μm. Once the number of particles in each bin with a specific radius had been found, the volume that

these particles occupied was calculated. This weighting allows more accurate representation of the particle size distribution in terms of a percentage mass or volume of powder having a specific size.

The SEM images for particle size analysis were taken using an acceleration voltage of 10 kV and beam current of 10 nA with Everhart-Thornley Detection of back-scattered electrons. The working distance was between 5.3 – 5.4 mm and magnification of images was 5000×.

The particle size distributions, represented as a histogram of percentage volume as well as represented as a percentage volume cumulative sum are shown in Section 5.3.2. The cumulative sum is calculated by summing in series the histogram data for particle sizes, allowing one to determine a percentage volume of particles that fall below a specific size.

5.2.3 Sample Preparation

Samples were produced with 30% volume loadings by the same wet-cast technique that is described in Chapter 3.

5.3 Results

This section contains the results for the cross-section analysis, particle size analysis and electromagnetic characterisation of the following grades of carbonyl iron powder;

- CIP CM
- CIP SM
- CIP EW
- CIP EW-I
- CIP EM
- CIP ES
- CIP HS
- CIP HQ
- 3rd Party 800 nm particles

All CIP grades were acquired from *BASF* Germany, except for the final 800 nm spherical Fe particles that were obtained from a 3rd party supplier, *SS-nano*. The 800 nm spherical Fe particles were confirmed to be onion-like in nature by cross-sectional analysis. It is therefore assumed that the manufacturing process is similar to the production of CIP and that these particles are actually carbonyl iron particles rather than pure iron. The results for these particles can be directly compared with results obtained from CIP grades provided by BASF. The typical cross-sections for these 800 nm particles are displayed in Figure 5.2.

5.3.1 Cross-section Analysis

SEM images for the typical cross-sections of each grade of CIP are shown in this section. This was performed to ensure that all grades had the internal structure stated by BASF and to see if there were differences in the layer thickness or number of layers for each powder. Typical sections of particles are displayed in Figure 5.1 where it becomes clear that the internal structure of particles can vary greatly.

The structure of many particles can be confirmed to be onion-like by seeing the concentric ring structures shown in Figure 5.1a and Figure 5.1b. However, the nature in which these concentric rings are manifest is presented differently in each image. Figure 5.1a shows distinct boundaries between phases, with an iron phase that is around 400 nm in thickness and separating boundaries that are only a few tens of nanometers thick. It is less easy to infer a thickness of layers for the structure displayed in Figure 5.1b as the phases appear more mixed as well as less consistent in thickness. these two particles are similar in size, meaning that there may well be more to consider with these particles than only size and the existence of an internal structure when investigating CIP grades.

There are further concerns when considering the internal structure of particles in a grade of CIP as it has been seen that a grade of powder with onion-like structure may also have particles with polycrystalline structures, shown in Figure 5.1c and Figure 5.1d. This further complicates the analysis of these particles, as it is unsure how prevalent these particles are. Again, with the onion-like structure, it is possible to see that this polycrystalline structure may itself vary. Figure 5.1c shows a particle with a polycrystalline structure with a large grain structure, whereas Figure 5.1d shows a particle

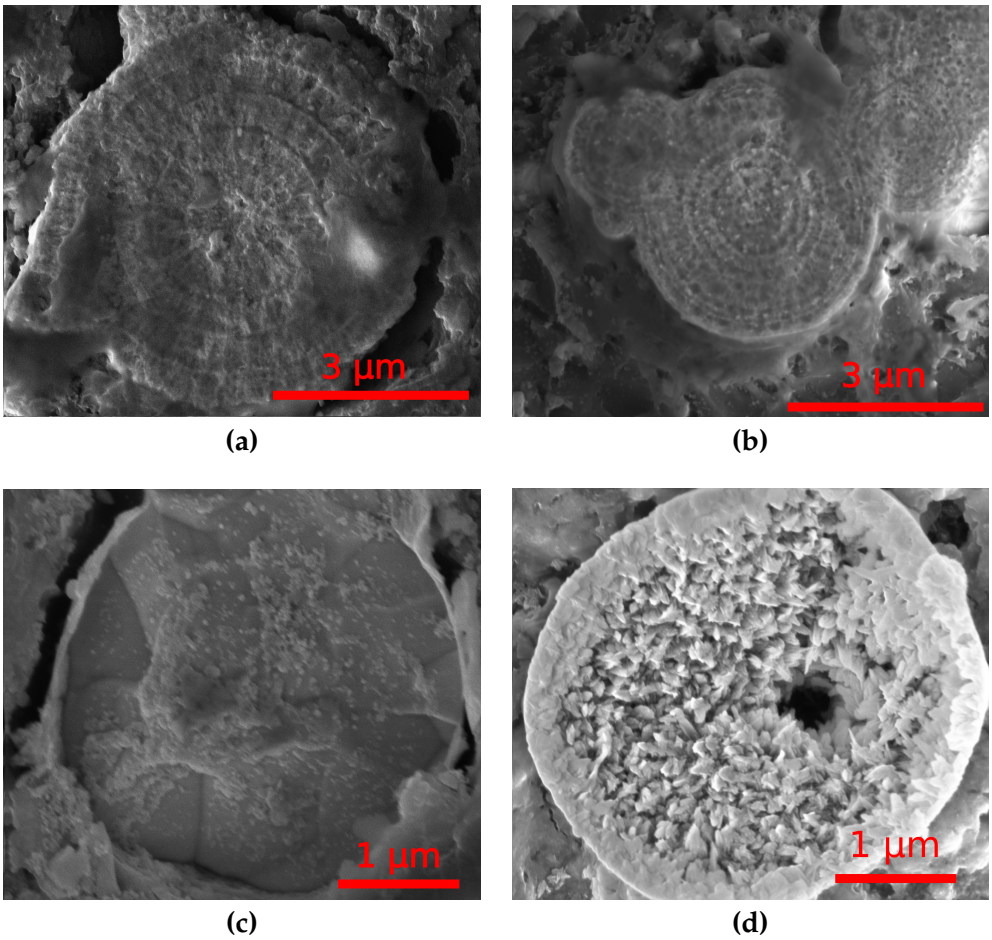

(a) **(b)**

(c) **(d)**

Figure 5.1: SEM micrographs of the cross section for CIP EW-I particles taken using the mechanical polishing technique. By comparing these images taken for the same grade, it is seen that there is great variation in the particle structure across the same powder. Images **(a-b)** show the anticipated onion ring structure, only with a variation in the way this structure has manifest itself. **(a)** shows a more defined boundary between layers and **(b)** shows a less explicit divide. Images **(c)**, and **(d)** show polycrystalline spheres with large and small grain sizes, respectively.

having a significantly smaller grain structure. The cross sections for 800 nm iron spheres from *SS-nano* are displayed in Figure 5.2 where the onion ring structure is again visible.

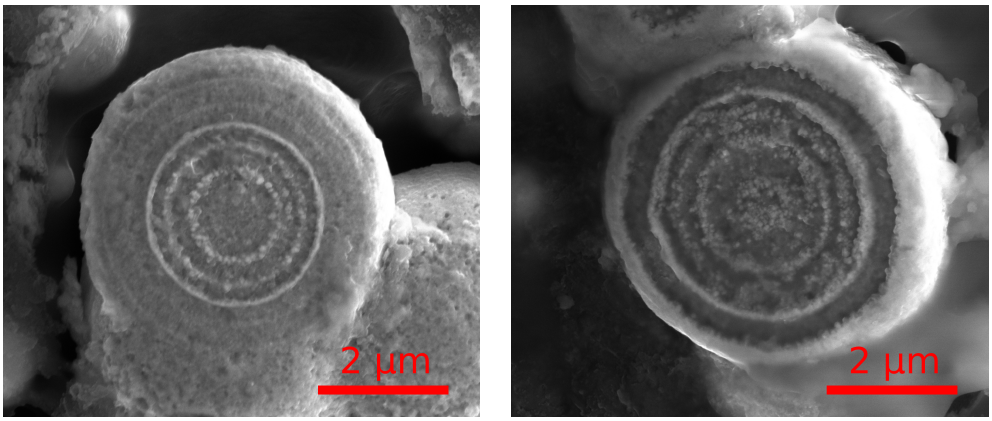

(a) (b)

Figure 5.2: Typical SEM micrographs for the cross-sections of 800 nm particles obtained from a 3rd party supplier.

5.3.2 Particle Size Analysis

Laser Light Diffraction

Laser light diffraction for particle size analysis performed at both Oxford and Johnson Matthey utilised a Mastersizer 2000 particle size analyser. The particles were dispersed in water and sonicated, and then run through the particle sizer. Sonication was used in order to break agglomerates, and the results are shown below for CIP grades ES, EM and HS. Johnson Matthey used the same technique for measuring the particle size distribution of CIP EM only, and provided a comparison of the results with and without sonication of the sample set. The index for the iron particles was assumed at Oxford to be $n = 1.52$ with an absorption of 0.9. At Johnson Matthey, the same value for refractive index of $n = 1.52$ was used, only with a value for absorption of 0.1. There is clear discrepancy between the particle size distributions from each of these iterations of analysis. The results from Oxford are shown in Figure 5.3. These results do show a mean value of particle size for each grade that is close to agreement with the expected values stated in BASF literature, with mean radii of 1.7 μm, 2.2 μm and 2.5 μm for CIP grades HS, ES and EM respectively. The results from JM appear to show significantly larger particles with the average size around 5 μm for CIP EM. From a comparison in Figure 5.4a between sonicated and unsonicated sample sets, we can see that more sub-micron particles are indeed detected but there is still a large discrepancy in the results from each institution for the

size of this CIP grade. It is possible that the discrepancy in volume of sub-micron particles is due to the different values for absorption used in each case of the experiment. The assumed absorption value when performing laser light diffraction is known to be critical when analysing particles that are in the sub-micron regime, with many more or many fewer sub-micron particles being identified depending on the value used. This is likely to shift the results from JM, but not sufficiently to account for the discrepancy seen. The reason particle size analysis by laser light diffraction fails for sub-micron particles is due to multiple scattering modes being supported by these smaller particles. The effect of these additional scattering modes is that the apparent sizes of these particles is larger than reality, causing a skew in the results that erroneously implies particles have fewer < 1 μm particles than there actually are. This discrepancy is shown in Figure 5.4b, where the results for SEM particle size analysis are compared with those produced by the laser light diffraction method.

It can be seen from Figure 5.4b that the particle size result from SEM imaging compared with both sets of results from laser light diffraction at different establishments appears to show more submicron particles as well as significantly fewer particles with radius greater than 3 μm. This is likely to be due to the issue stated previously with smaller particles producing higher order scattering terms that cause erroneous inference of larger particles. It may also be possible that particles with a particularly large radius were not kept adhered to the surface of the SEM stub for analysis. This would cause a reduction in the perceived upper limit of particle size for all powders in SEM analysis. This will be discussed in greater detail in the upcoming subsection.

SEM Analysis

This section exhibits the results for particle size analysis of each grade of CIP investigated through SEM imaging. The size distributions have been plotted as a histogram plot with a percentage volume corresponding to the volume of powder that fits within the stated radius bounds. Plotted alongside this size distribution is a cumulative sum of the corresponding percentage volume, which has been calculated by sequentially adding the percentage volume of each bin in increasing size. A smooth curve was fitted to the histogram data of particle sizes by using a skewed Gaussian curve.

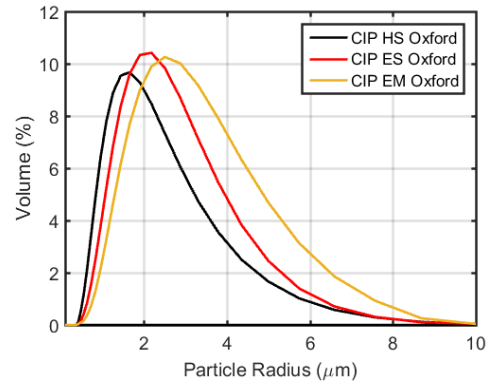

(a)

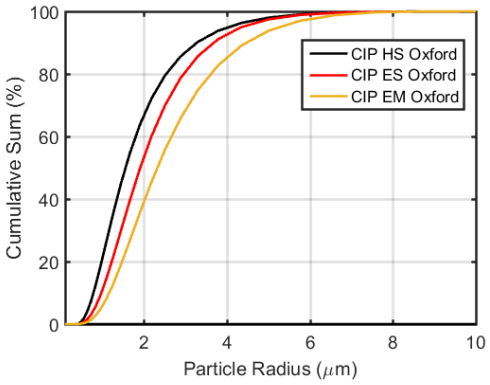

(b)

Figure 5.3: (a) Particle Size distribution and **(b)** cumulative sum of particle size distribution for CIP grades HS, ES and EM taken by Oxford using laser light diffraction equipment. The cumulative sum is taken by sequentially summing the value of volume percentage for each particle size until all data has been summed.

Figure 5.5 shows the particle size distributions for CIP grades CM, SM, EW and EW-I. The first two grades, CIP CM and SM are the particles expected to have a "soft", polycrystalline internal structure, with the discerning feature that these two grades of powder should have vastly different mean sizes and size distributions. CIPs EW and EW-I were both expected to be of similar size range, with "hard" onion-like structure and the discerning feature that CIP EW has no coating whereas CIP EW-I should possess a coating.

By comparing Figure 5.5a and Figure 5.5b it is possible to see that there is indeed a great difference in particle size and width of distribution for CIPs CM and SM, meaning an investigation into the particle size effects on electromagnetic properties of "soft" magnetic inclusions may be performed by

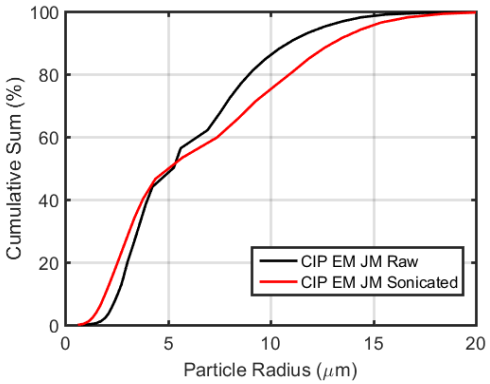

(a)

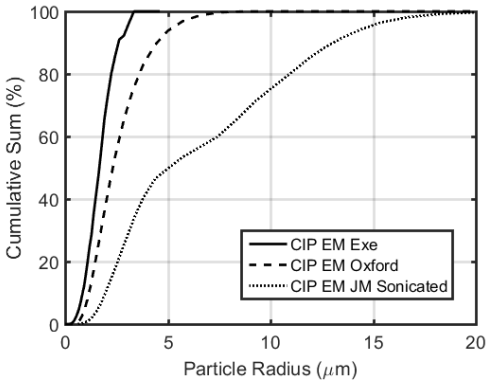

(b)

Figure 5.4: (a) Cumulative sum of the size distributions for CIP EM measured by Johnson Matthey using laser light diffraction techniques, comparing the results for a raw batch of powder (Black) with those for a sonicated batch (Red) **(b)** Cumulative sums of the particle size distributions for CIP EM measured in 3 different instances. One set are results from SEM imaging techniques at University of Exeter, and the two others are independently measured by Oxford and JM by laser light diffraction.

comparing these powders. The mean size for CIP SM appears to be significantly lower than expected from BASF literature, with an average radius measured of 1.65 μm compared with the expected value of 3.5 μm. This grade of powder, under SEM analysis, has proven to possess a higher number of sub-micron particles than would be expected. This may be similar to the discrepency seen when comparing analysis techniques in Section 5.2 where a grade of powder appears larger than it is due to multiple scattering modes of sub-micron particles. The mean particle size for CIP CM also appears to be smaller from SEM analysis than expected from stated values, with a measured mean particle size of 4.33 μm compared with the expected

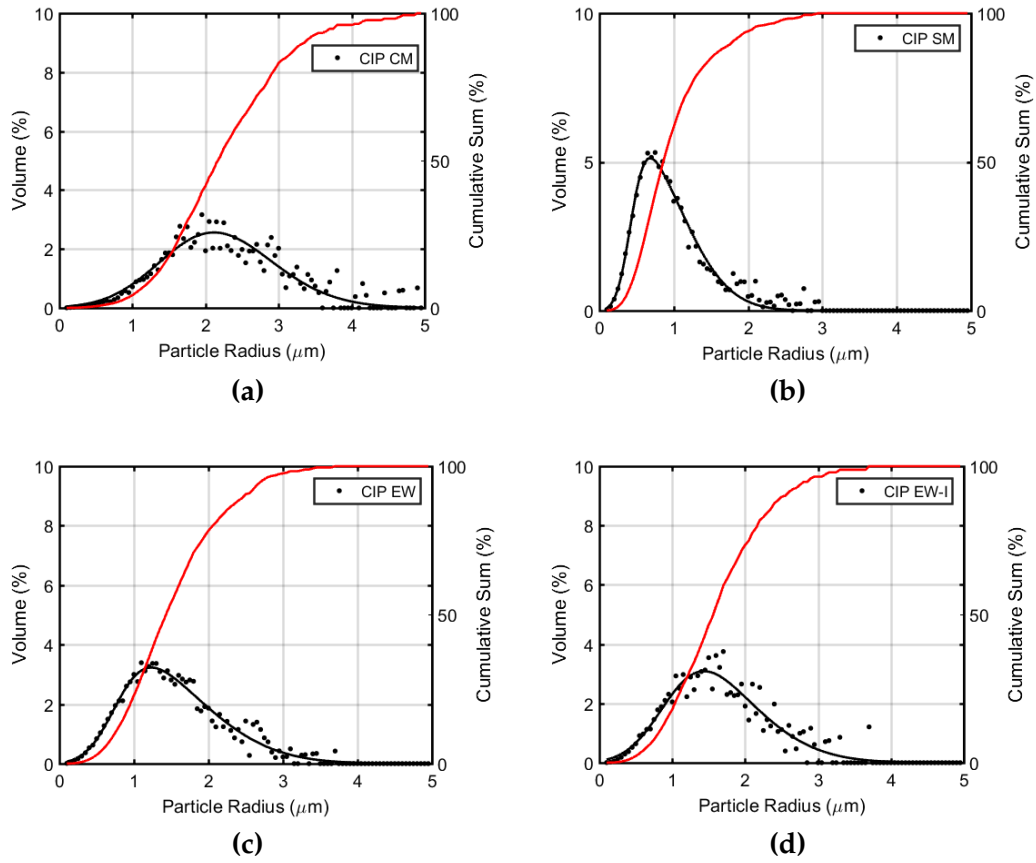

Figure 5.5: Particle size distribution (black) and cumulative sum of particle size distribution (red) for **(a)** CIP CM **(b)** CIP SM **(c)** CIP EW **(d)** CIP EW-I. Each of the distributions has been fitted to with a skewed Gaussian curve. From these curves, a full width at haf maximum (FWHM) is taken to give a numerical representation of the spread of data.

range of $7.0 - 9.5$ μm. A comparison of Figure 5.5c and Figure 5.5d shows that the two grades CIP EW and CIP EW-I do indeed possess similar mean particle sizes and size distributions, validating the comparison of the effects of a particle coating on electromagnetic properties.

Figure 5.6 displays the results for particle size analysis on CIP grades EM, ES, HS, HQ and the 3rd party 800 nm Fe particles. All of these particles possess an internal onion-like structure, and the greatest discerning factor between each is the mean size and size distribution. Analysis of these powders will provide insight into the particle size effects of the electromagnetic properties of CIP.

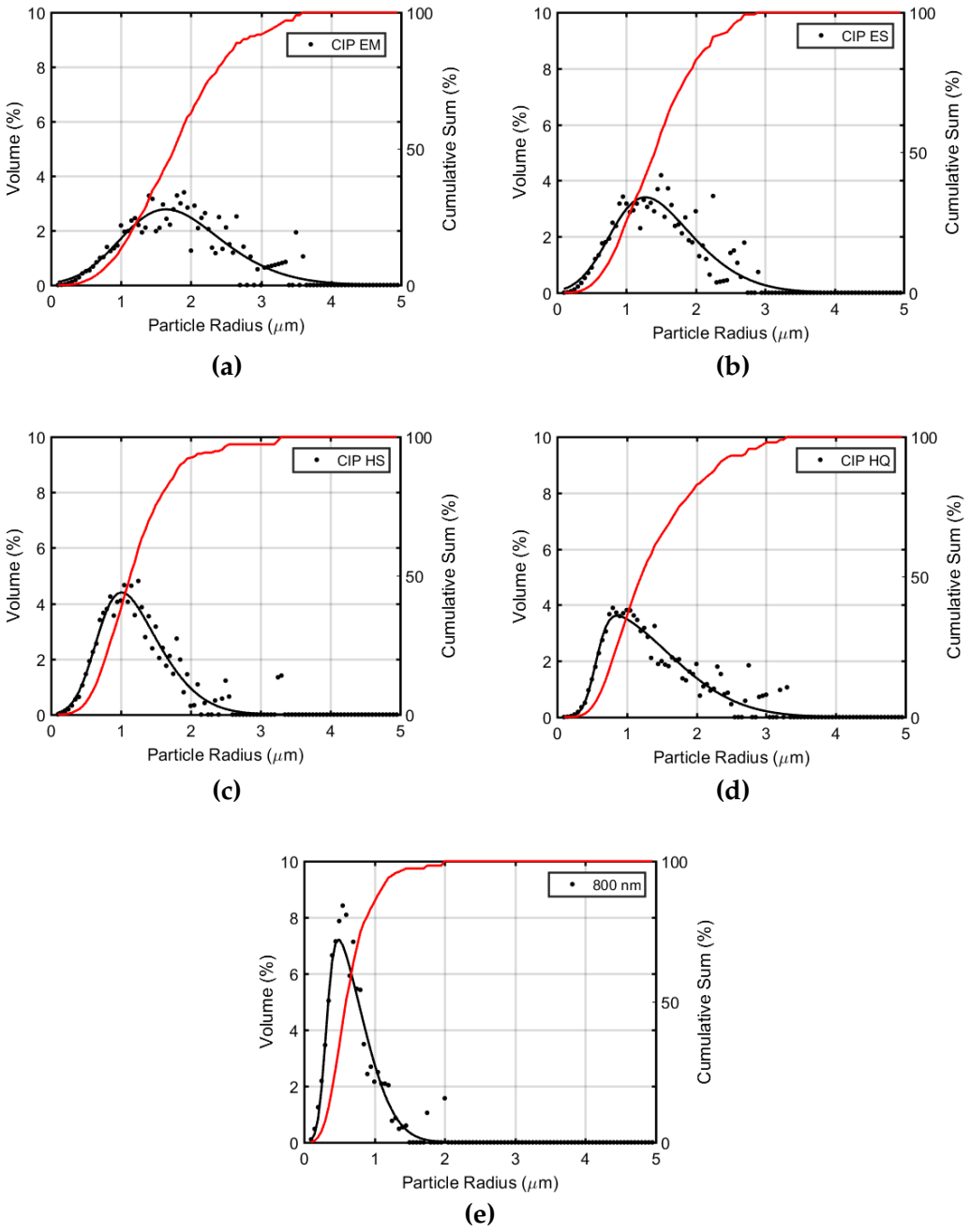

Figure 5.6: Particle size distribution (black) and cumulative sum of particle size distribution (red) for **(a)** CIP EM **(b)** CIP ES **(c)** CIP HS **(d)** CIP HQ and **(e)** 800 nm Fe. Each of the distributions has been fitted to with a skewed Gaussian curve. From these curves, a FWHM is taken to give a numerical representation of the spread of data.

CIP Grade	Stated Size (d50)	Measured Size	Structure	Coating
CIP CM	7.0 - 9.5 μm	4.33 ± 1.90 μm	Soft	Uncoated
CIP SM	3.5 μm	1.65 ± 0.95 μm	Soft	Uncoated
CIP EW	3.0 - 4.0 μm	2.81 ± 1.50 μm	Hard	Uncoated
CIP EW-I	3.0 - 4.0 μm	3.09 ± 1.55 μm	Hard	Coated
CIP EM	4.5 - 6.0 μm	3.46 ± 1.75 μm	Hard	Uncoated
CIP ES	3.4 - 4.5 μm	2.85 ± 1.45 μm	Hard	Uncoated
CIP HS	1.8 - 2.3 μm	2.23 ± 1.10 μm	Hard	Uncoated
CIP HQ	2.0 μm	2.20 ± 1.35 μm	Hard	Uncoated
800 nm Fe	800 nm	1.16 ± 0.65 μm	Hard	Uncoated

Table 5.1: A table showing the expected mean size and measured mean size for all grades of CIP investigated. The stated size is given by BASF and corresponds to the size below which 50% of the particles fall. The measured size was given by the same definition, and the distribution was inferred from the FWHM of each curve fitted to the measured data.

5.3.3 Electromagnetic Properties Comparisons

"Hard" vs. "Soft"

As already stated, the process for producing carbonyl iron particles involves the condensation of iron pentacarbonyl gas into iron and carbon monoxide, with a secondary reaction when carbon monoxide reaches high levels. This results in a layered structure for the particles, with an iron core and alternating layers of iron-carbide and iron. CIP grades with this onion-like internal structure are referred to as "hard" grades. It is possible to remove this structure after the production process by sintering these particles in a hydrogen atmosphere at temperatures greater than 300°C [121, 122]. Powders with a polycrystalline internal structure are referred to as "soft" powders. This section presents data for a comparison of results for composites formed from "hard" and "soft" magnetic powders, as in Figure 5.7. The section then displays data for these "hard" and "soft" particles separately, such that an investigation into the particle size effects of the electromagnetic properties of composites may be made for both "hard" and "soft" particles.

The permittivity and permeability for similar grades of carbonyl iron powder that exhibit "hard" and "soft" structures is compared in Figure 5.7. It is difficult to ascertain from these plots what the effects of internal structure are. Plots of the refractive index loss tangent, as well as a Cole-Cole plot of the complex refractive index are displayed in Figure 5.8. These plots show

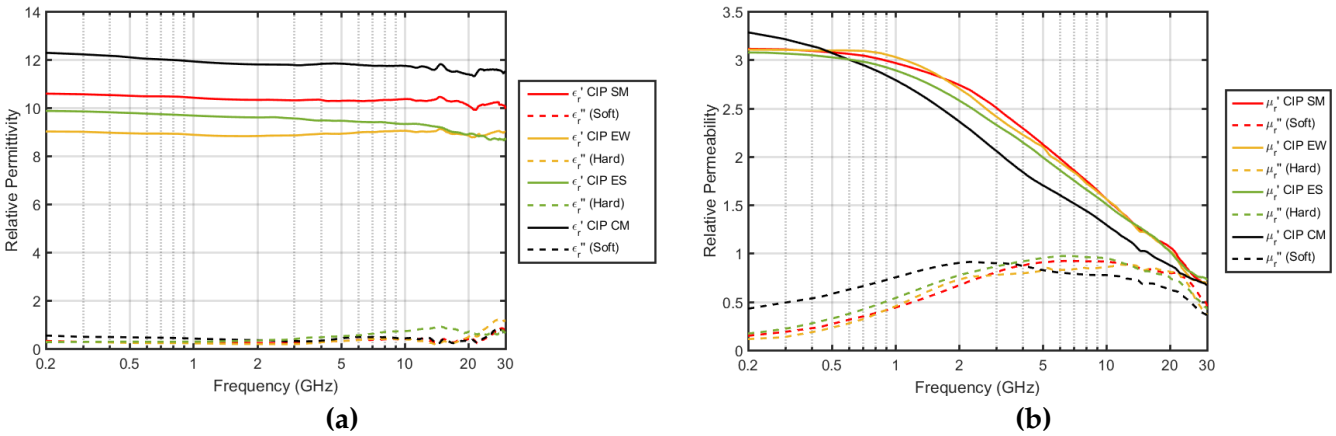

Figure 5.7: (a) Complex relative permittivity and **(b)** relative permeability for CIP grades SM, EW, ES and CM. CIP grades SM and CM are both described as "soft" powders, possessing a polycrstalline internal structure, whereas CIP grades EW and ES are "hard", possessing the onion-like internal structure.

that there is a higher order mode supported in these powders regardless of the structure that is present in the particles. The dependence on particle size distribution for the position in frequency of these modes is also similar regardless of internal structure. By decreasing the size distribution of the powders, the position in frequency of the higher order mode increases, and sharpens when the size distribution is narrowed.

"Hard" Particle Size Effect

Direct comparisons of only "hard" grades of CIP have been plotted in Figure 5.9. The plots display results for CIP grades EM, ES, EW and HQ. It is possible to see a difference between the electromagnetic properties for these composites that is dependent upon the mean size and distribution of particle size for each of the grades. The relative permittivity of these composites is almost constant with frequency, so to better look into the absorption properties of these composites as a function of frequency, the imaginary part of the index for these composites was compared instead. A plot of the loss tangent for the refractive index, as well as a Cole-Cole plot of the complex index are displayed in Figure 5.10.

From the plots displayed in Figure 5.10 it is clear to see the size dependence on higher order modes for composites formed from these powders.

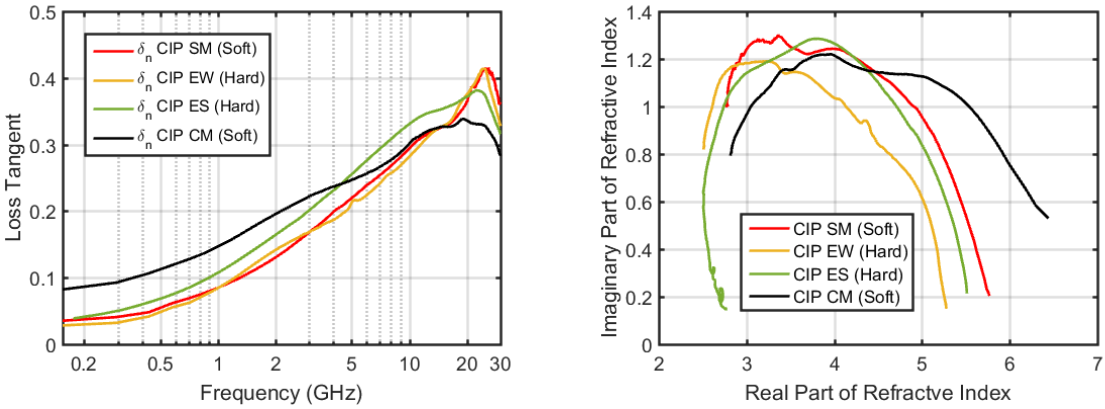

(a) **(b)**

Figure 5.8: (a) Refractive index loss tangent and **(b)** refractive index Cole-Cole plot for CIP grades SM, EW, ES and CM in composites at 30%vol. loading for CIP. CIP grades SM and CM are both described as "soft" powders, possessing a polycrstalline internal structure, whereas CIP grades EW and ES are "hard", possessing the onion-like internal structure.

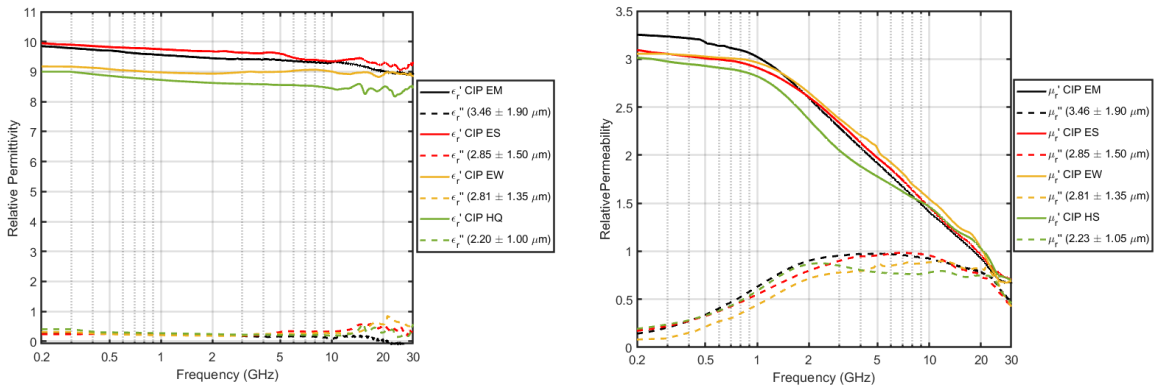

(a) **(b)**

Figure 5.9: (a) Complex relative permittivity and **(b)** relative permeability for CIP grades EM, ES, EW and HQ in composites at 30%vol. loading for CIP. Each of these powder grades are "hard", possessing onion-like internal structure.

Coating Effect

A comparison of results for CIP grades EW and EW-I is displayed in Figure 5.11. This is a direct comparison between two grades that should be identical other than the addition of a coating to the particles in the case of CIP EW-I. It is assumed that this coating is phosphate, and is intended to

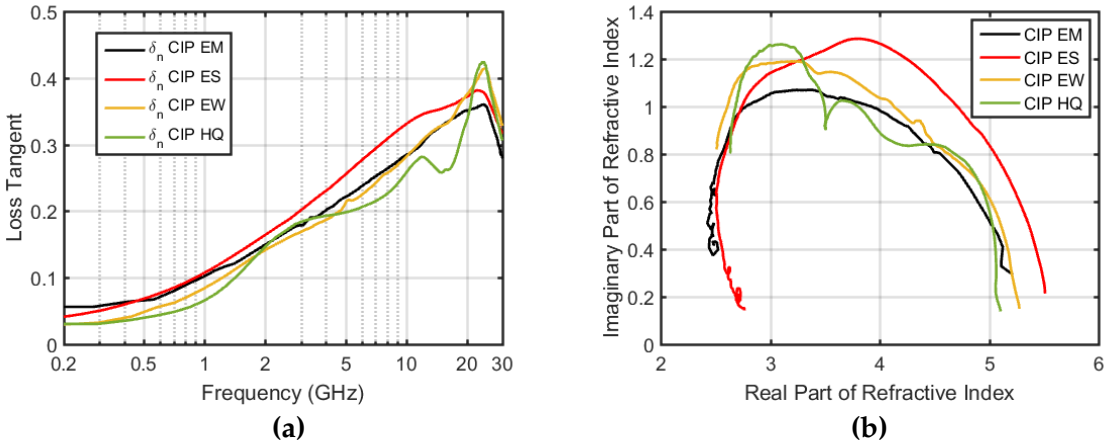

Figure 5.10: **(a)** Refractive index loss tangent and **(b)** refractive index Cole-Cole plot for CIP grades EM, ES, EW and HQ in composites at 30%vol. loading for CIP. Each of these powder grades are "hard", possessing onion-like internal structure. The plots are displayed in order of decreasing average particle size.

give the particles an element of isolation from each other, preventing inter-particle conduction. This coating is also useful for preventing oxidation of the particles post-production. There appears to be a reduction in both the real permittivity and permeability from the addition of a coating to these particles. It is possible that the coating is preventing the excitation of magnetic moments, and reducing the effective permeability of the particles. In order to better investigate the absorption of these particles, loss tangent for the refractive index, and a Cole-Cole plot from the complex parts of the refractive index are displayed in Figure 5.12.

From comparing the effects on the imaginary index that a coating on the particles has, it is difficult to state any strong effect. The absorption of the coated particles appears slightly stronger across all frequencies, with the apparent higher order mode at ∼22 GHz being stronger also. However, the differences between these two results are not great enough to infer any significant effect from the coating of the CIP EW-I particles.

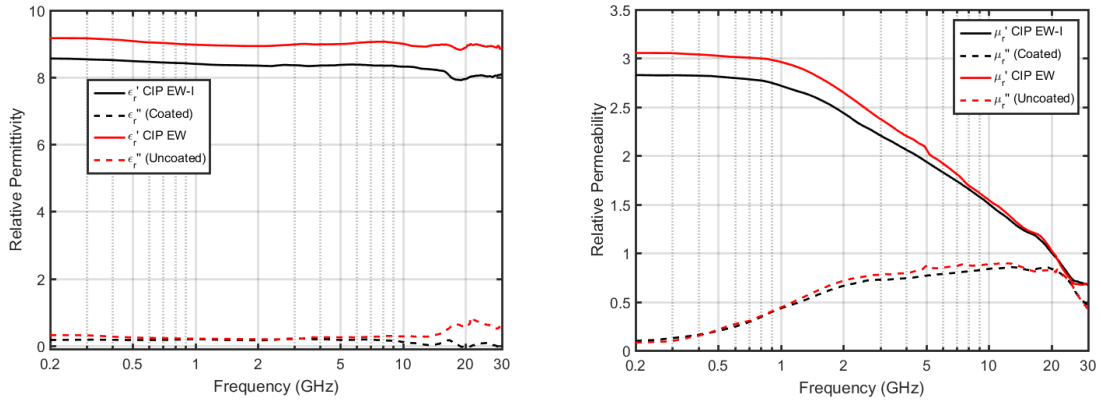

(a) **(b)**

Figure 5.11: **(a)** Complex relative permittivity and **(b)** relative permeability for CIP grades EW and EW-I. These two grades are expected to be similar in size and internal structure, with the only difference between them being the existence of a coating on CIP grade EW-I, whereas CIP EW has not been coated.

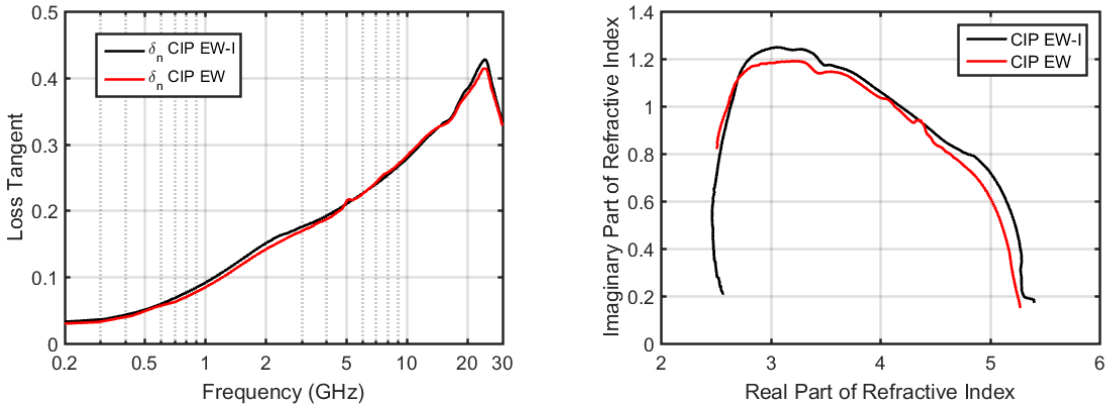

(a) **(b)**

Figure 5.12: **(a)** Refractive index loss tangent and **(b)** refractive index Cole-Cole plot for CIP grades EW and EW-I. These two grades are expected to be similar in size and internal structure, with the only difference between them being the existence of a coating on CIP grade EW-I, whereas CIP EW has not been coated.

5.3.4 Particle Size Effect on Refractive Index

It has been seen that the grade of CIP has some effects on the electromagnetic properties of these powders. By looking at the refractive index, it is clear that there is a distinction when looking at CIP grades based on their mean size and size distribution alone. To better highlight this dependence

on size and distribution of size, the refractive index for 5 grades of CIP have been compared. The volume distribution of particle size is displayed in Figure 5.13a while the cumulative sum of these distributions is shown in Figure 5.13b.

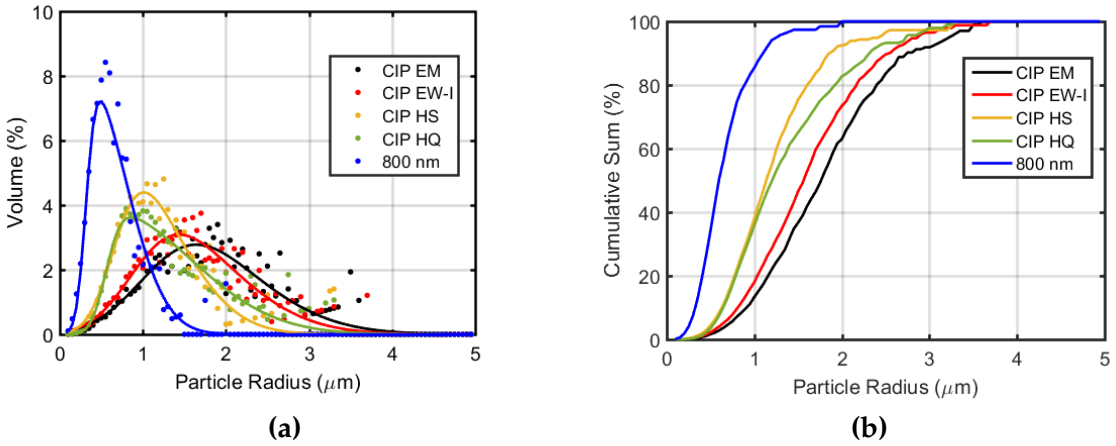

(a) **(b)**

Figure 5.13: (a) Size distributions as percentage volume and **(b)** cumulative sum of size distributions for CIP grades EM, EW-I, HS, HQ and 800 nm spherical iron powder.

Figure 5.14 shows the complex refractive index for the 5 grades of CIP whose size distributions are shown above. As the mean size and spread of distribution is decreased, the emergence of higher order modes at frequencies above 10 GHz is demonstrated. It is also possible to see a separation of the fundamental magnetic mode, typically seen at frequencies close to 2 GHz. It is known that the size distribution of nano-sized particles will affect the linewidth of the fundamental resonance, as the differing contributions between superparamagnetic and multi-domain particles will change the shape of this absorption spectrum [25, 123]. However, this is not yet fully understood for particles in the micron-size regime. It is not likely that contributions from superparamagnetic particles is the cause of the change in intensity and shape of the fundamental mode as a function of particle size. It is possible that there is a contribution due to single domain particles, which are known to have a different absorption spectrum from multi-domain or vortex-domain particles [24].

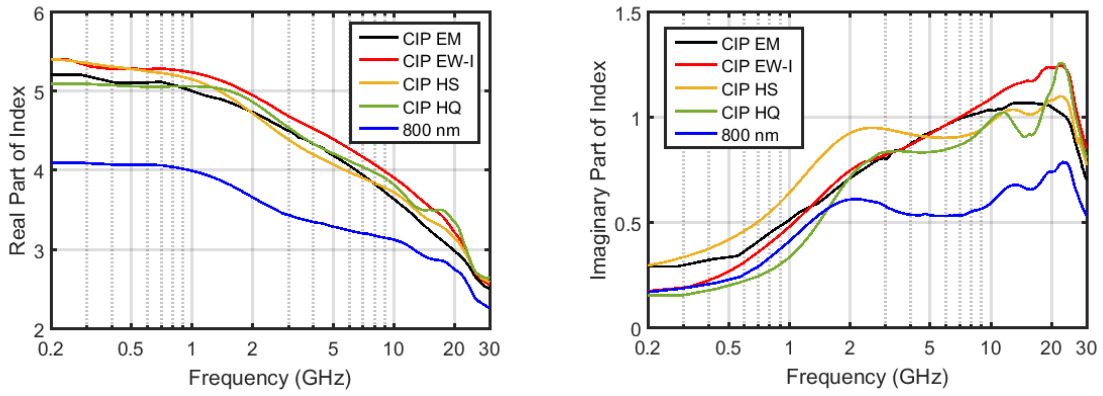

(a) **(b)**

Figure 5.14: (a) Real and **(b)** imaginary parts of index for CIP grades EM, EW-I, HS, HW and 800 nm Fe particles. Index is displayed across the frequency range 200 MHz - 30 GHz for composites containing 30%vol. CIP loading.

Plots of the refractive index loss tangent, and a Cole-Cole plot from the complex parts of the refractive index are shown in Figure 5.15. These plots highlight more strongly the size dependence pon the loss of composites formed from carbonyl iron powder and polyurethane.

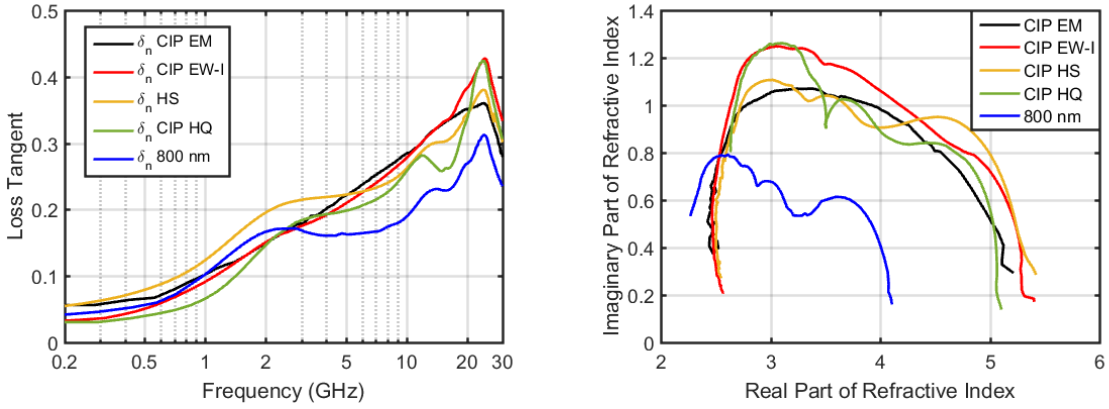

(a) **(b)**

Figure 5.15: (a) Refractive index loss tangent and **(b)** refractive index Cole-Cole plot for CIP grades EM, EW-I, HS, HW and 800 nm Fe particles. Index is displayed across the frequency range 200 MHz - 30 GHz for composites containing 30%vol. CIP loading.

Since higher order modes have been demonstrated to exist in these composites containing particles in the single-micron size regime, it is necessary to investigate if these higher order modes will be affected by interparticle

coupling when the volume loading of carbonyl iron powder is increased. The results for this dependence on volume fraction are displayed below.

5.3.5 Volume Fraction Dependence on Higher Order Modes

Composites were formed with CIP loading from 10% - 40%vol. in 10%vol. increments, as in Chapter 4. The powders used for the analysis of the volume fraction dependence on higher order modes were CIPs HS, ES, EM and EW-I. These powders were chosen due to their availability, as there was enough bulk material of each powder for the production of many composites to analyse. It is also possible to investigate the effect that particle coating has on the inter-particle coupling by investigation of CIP EW-I. Plots of the refractive index loss tangent for each powder at different volume loadings are displayed in Figure 5.16.

From comparing the shape of the curves in the plots of loss tangent and Cole-Cole plots of the refractive index, it is possible to infer whether a change in the volume fraction for CIP in composites affects the observed resonances. Since the shape of the curve at each loading for all samples is similar, it may be inferred that volume loading does not affect the modes. The lack of inter-particle coupling at higher loadings for these powders is unsurprising as the vortex domain structure for these particles causes the stray field to be confined mainly within the particles themselves, giving little possibility for coupling to occur. Also, since it has been observed that using a wet-mixing fabrication technique for samples prevents issues related to conduction by percolation, it may be inferred that a negligible amount of particles are touching.

5.4 Nanoparticle Composite Characterisation

Nanoparticles were obtained from a 3rd party supplier (*S S Nano*) that were claimed to be a spherical iron powder with average particle size of 100 - 130 nm. It was not possible to confirm the shape or size distribution of this powder by SEM analysis as the safe handling of nanopowders was not ensured. It was stated by the manufacturer that these powders had been fabricated using exploded wire technique [124].

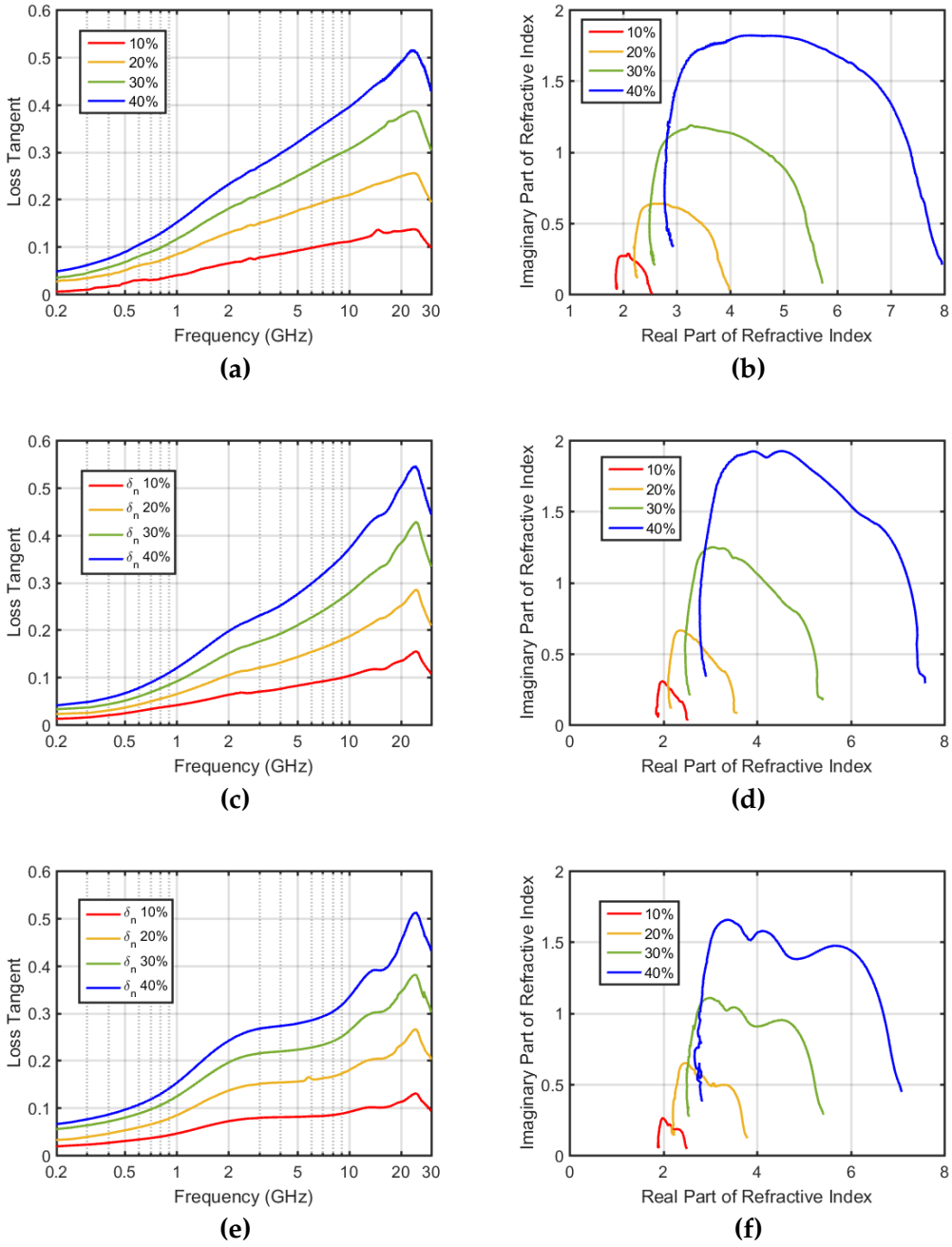

Figure 5.16: Loss tangent of refractive index for **(a)** CIP EM, **(c)** CIP EW-I, **(e)** CIP HS and Cole-Cole plot of complex parts for refractive index for **(b)** CIP EM, **(d)** CIP EW-I, **(f)** CIP HS.

Composite samples were manufactured using this powder and a similar

technique to the wet-cast technique described in Chapter 3, only the powders were pre-mixed into a suspension at a different facility capable of handling dry nano-powders more safely. It is not known what the effect of keeping these powders in suspension with the liquid parts of the polyurethane mixture for a prolonged period will be. The iron - polyurethane epoxy part A suspensions were then mixed in-house with polyurethane part B to produce composites with %volume loadings of 5%, 15%, 20% and 30%. It proved difficult to produce a large amount of samples as the technique for mixing composites was sub-optimal for producing homogeneous samples with accurate dimensions. The suspensions of nanoparticles were more viscous than those created previously with larger powders, so it was more difficult to create a homogeneous composite. When forcing a viscious mixture of composite material into the moulds, there is a higher chance of cracking and rough surfaces due to air bubbles. It is also more difficult to get an accurate height of sample to fit into the stripline cavity as the somposite mixture does not flow easily and self-level.

Preliminary results for the refractive index of these samples are displayed in Figure 5.17. As has been observed previously in this chapter, there are absorption modes at frequencies significantly higher than the expected FMR mode. The resonances, when compared with those seen in 800 nm spherical particles, are seen to be sharper and at a slightly higher frequency. It is expected from micromagnetic modelling and other literature that there should be higher order resonances at even higher frequencies for these powders [9, 24, 63]. However, due to the aformentioned issues in sample manufacture the samples were not ideal for characterisation above 30 GHz. The height of samples did not completely fill the stripline cavity and the roughness of sample meant that higher frequency measurements had a high amount of loss and sharp resonances in the S-parameter data.

The loss tangent of refractive index for a 30%vol. sample comprising 100 nm spherical iron powder is compared with that for a sample comprising 800 nm particles in Figure 5.18. Here we can see the higher order modes more clearly. The FMR, typically seen at $\sim$ 2 GHz for iron, appears to be suppressed in comparison to the higher order modes in this result, or the FMR has been shifted higher in frequency by the presence of particles that are single domain. The change in frequency for higher order modes is not as large as would be expected for the difference in average particle size for these 100 nm particle composites. It is possible that there are more high

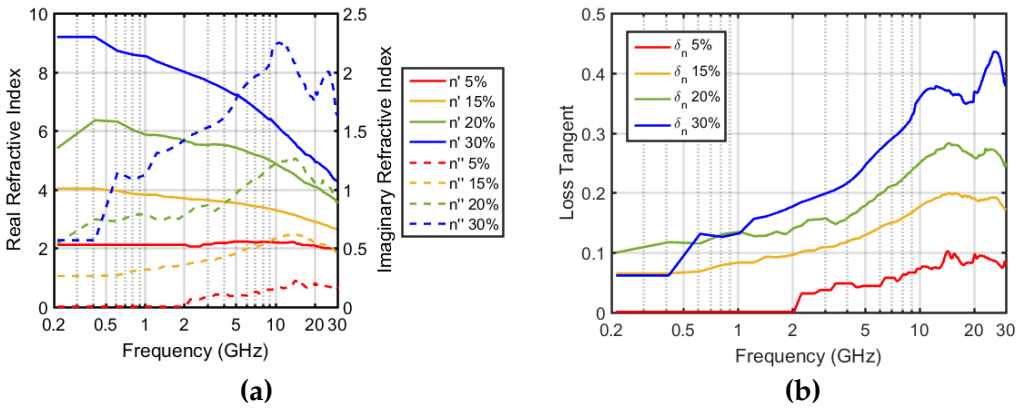

Figure 5.17: Graphs showing preliminary results for the refractive index, **(a)**, and loss tangent of refractive index, **(b)**, of composites comprising 100 nm iron powder in polyurethane.

frequency modes that have not been observed in this experiment.

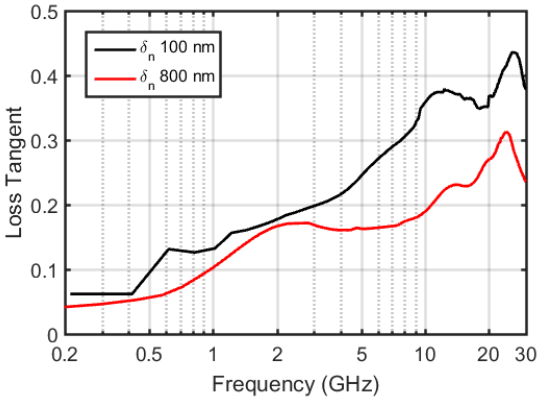

Figure 5.18: Graph comparing the refractive index loss tangents for composites comprising 100 nm Fe particles in polyurethane (Black) and 800 nm Fe particles in polyurethane (Red). Both composites are made with 30% volume loading of Fe powder.

It is also possible that agglomerates had been formed when these 100 nm composites were fabricated, meaning the average size of the effective particles in the composites would be significantly larger than otherwise expected. This larger effective particle size would cause composites to have a similar response to those seen in composites with larger inclusions, so the higher order modes would be more closely matching in frequency to those seen in the 800 nm powder composites. It is also possible to obtain 100 nm

nanoparticles that possess a coating to prevent oxidation and conduction between particles but these were not investigated due to limitations of time.

5.5 Chapter Summary

In summary, a total of 9 different carbonyl iron powders have been compared by including each into a composite with polyurethane for electromagnetic characterisation. Particle size distributions for each grade were measured, allowing an investigation into how the distribution and mean size of particles affects the properties of the powder. The results presented here for the average partice size are different from those measured by laser diffraction methods presented by BASF [125, 126] and by other institutes in this chapter. It is possible that there is discrepancy due to systematic error in either of the two techniques, so a more concise comparison is required.

It has also been possible to investigate the effects of internal structure on composite properties, by comparing two grades with "soft" polycrystalline structure with particles of a similar size that have an onion-like internal structure. However, the variance in internal structure for onion-like particles makes for a difficult comparison. It is difficult to state with confidence that any carbonyl iron grade with an onion-like structure will have a specific thickness for each of the phases comprising the structure. It is also difficult to currently state that all onion-like particles actually have the same concentric, disconnected structure as SEM analysis of particles has highlighted even a difference in the way an onion-like structure may manifest itself.

Some differences in grade properties have been measured that may be associated with the different design parameters of the particles. The ability to measure differences in CIP grades based on indeterminable discrepencies in manfacture highlights the need to be able to produce particles such that they have controllable features. These controllable features should include;

- Specific thicknesses of phases comprising the internal structure of "hard" particles,
- Ability to preferentially produce particles with either of the two onion-like structures displayed,
- Particle radii, with monodisperse or at least controllable distributions,
- Crystal size for polycrystalline particles.

This is by no means an extensive list of desirable variables, but is the list of necessary controllable parameters for a full investigation into spherical

magnetic modes in both solid spheres and spherical shells/ concentric shell structures.

The simplest problem to tackle is the tuning of mean size and size distribution for different grades of CIP. A technique for separating a single grade of carbonyl iron into subgrades with different mean sizes and size distributions is required. A technique for achieving this separation is described in Chapter 6, and the results of applying this technique are presented in the upcoming chapter.

Chapter 6

Particle Size Filtration by Air Elutriation

6.1 Introduction

It has been demonstrated in Chapter 5 that the size of spherical powders appears to have a strong affect on the prevalence of higher order magnetic modes in composites. It is necessary to investigate whether these modes are supported in these smaller powders as a result of the size distribution for particles alone or if they are a product of the differences in the manufacturing process between different grades of CIP.

As was discussed in Chapter 2, the separation of fine powders based on size for particles in the single-micron size regime is a not a trivial task. It is difficult to produce mechanical seives with a mesh that is fine enough to filter powders into separate sizes. Furthermore, those that have been produced require advanced equipment for sonically agitating the powders during the filtration so agglomerates are broken and the mesh does not become clogged. This chapter presents an air elutriation technique that is both cheap to manufacture, and simple to construct. This technique does not require wetting of the particles as dry air can be fed in.

This chapter contains results for the particle size distribution of CIP EM before and after the application of air elutriation to remove the smaller particles from the bulk. Results are then presented for the particle size distribution of 4 distinct sub-grades of CIP EM that were separated by air elutriation using a collection chamber to retain the smaller particles. Data is then presented for the electromagnetic properties of composites formed with polyurethane and each of the sub-grades of CIP EM.

6.2 Method

The experimental method for this air elutriation experiment is detailed in Chapter 3. The experiment first used a single glass bottle of inner diameter 65 mm, connected to a bubble filter to test the extraction of small particles from the bulk material. A bubble filter was connected in series to ensure the small particles were safely captured but the reaction of the small particles with the water meant that the captured particles were not suitable for characterisation. Drying powders out from a wet mixture would cause the powders to agglomerate, fusing particles together such that homogeneous samples would not be able to be fabricated. Once the single-bottle technique had been tested, a second bottle was connected in series between the first bottle and the bubble filter. This second bottle had an inner diameter of 180 mm, meaning the air flow speed in the first bottle would be reduced significantly when flowing through the second chamber. This reduction in the air flow speed would mean that the particles that had been carried through the first chamber would be able to settle for collection. Some particles did still inevitably make it through the entire system, meaning a bubble filter was still necessary for safe capture of fine particles.

As discussed in Chapter 3, the relation between particle radius cutoff, R, for an elutriation chamber of inner diameter, d, and insertion volume flow rate, Q is given by Equation (6.1).

$$Q = \frac{10\pi g}{3\mu} \cdot (\rho_{\mathrm{p}} - \rho_{\mathrm{f}}) d^2 R^2 \tag{6.1}$$

The filtration for each sub-batch of powders was run over the course of 24 hours for each volume flow rate of air. It is necessary to periodically tend to the set-up as the dust cloud that settles will stick to the sides of the glass bottle and inside the stainless steel tubing. On a regular basis during the day, the set-up was hit sharply with a metal rod to tap the powders back into the neck of the bottle. Vibrational motors were also loosely attached to the glass bottles and stainless steel tubes connecting the bottles also. The rattling of the vibrational motors against the set-up provided some agitation when the set-up was unable to be tended to during the night.

6.3 Results

6.3.1 Particle Size Filtration

Removal of Eluate

First the experiment was run with a single bottle, not collecting smaller particles lifted out from the chamber. This was to test that using a low volume flow rate would indeed separate smaller particles from the bulk. The experiment was run with a volume flow rate of 0.6 LPM. For a bottle with inner diameter of 65 mm this volume flow rate corresponds to an air flow speed of 3.0 mm s^{-1}.

Volume Flow Rate (LPM)	Predicted Diameter (μm)	Measured Diameter (d50) (μm)	d10 (μm)	d90 (μm)
Raw Powder	N/a	3.46 ± 1.96	1.82	5.50
1.2	$d \geq 3.56 \pm 0.44$	4.48 ± 1.46	3.04	5.94

Table 6.1: Table showing the predicted and measured size ranges for particles filtered from a batch of CIP EM. This size range is compared with that measured for a raw, unfiltered batch of CIP EM. d10, d50 and d90 correspond to the diameters below which 10%, 50% and 90% of measured particles fall.

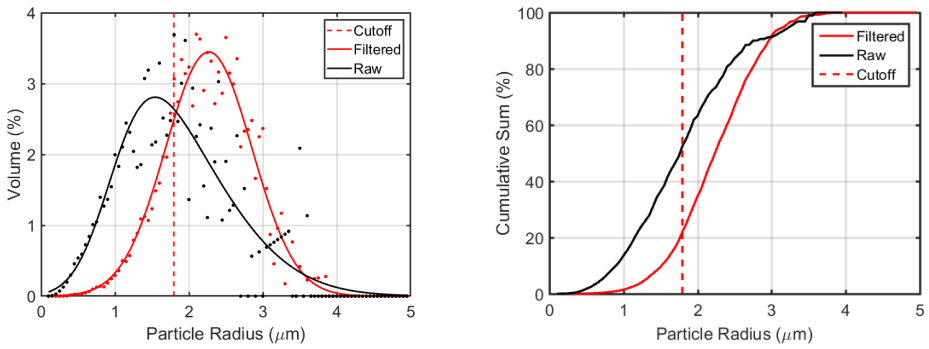

(a) **(b)**

Figure 6.1: **(a)** Particle size distribution for a sub-batch of CIP EM created by filtering at a volume flow rate of 0.6 LPM to remove particles. A skewed Gaussian fit is also plotted. **(b)** Cumulative sum of the histogram data normalised to total 100%. Dashed lines show the expected cutoff for maximum size of particles to be filtered from the bulk and in black is shown the particle size distribution and cumulative sum of the distribution for the raw, unfiltered CIP EM powder.

The size distribution for the powder left over when using a volume flow rate of 0.6 LPM has been narrowed by the filtration process. The mean particle radius has been increased from 1.73 μm to 2.26 μm and the dispersion of particle radii, calculated from the full width half maximum of the Gaussian data, has been decreased from 0.88 μm to 0.73 μm. These results are displayed in Figure 6.1 and Table 6.1. The source of uncertainty for predicting the radius of particles leaving the system is from considering the standard uncertainty in measurement of the inner diameter for each bottle, $\Delta d = \pm 5$ mm, and the uncertainty in monitoring the volume flow rate of air into the system, $\Delta Q = \pm 0.1$ LPM. The manometer used was able to measure volume flow rate to a precision of 0.1 LPM. Using a bubble filter on the end of the setup causes the volume flow rate to fluctuate as bubbles form, adding further to the uncertainty in volume flow rate. In the 6 mm stainless steel tubes connecting the elutriation chambers, powder builds up over time during the experiment. If the experiment is left unattended, this build-up can cause the tubes to become clogged, and pressure will build up until a jet of powder is pushed out from the connecting tube into the next chamber. This jet can cause particles that are larger than the cutoff of to be pushed through the entire system. The experiment was agitated regularly in an attempt to ensure this build-up was not an issue but it is likely that these jets still occurred throughout the duration of the experiment.

Collection of Eluate

The second experiment was performed to test the elutriation technique with a particle collection chamber. Again, 30 g of CIP EM was added to the first chamber and three volume flow rates of 0.8, 1.5 and 2.5 LPM were chosen for filtration. This experiment resulted in 4 sub-grades of powder, one for each flow rate and a final batch for the left over particles. Once these sub-grades had been collected, SEM analysis was performed to generate particle size distributions. Standard images of the 3 batches of powder collected at each volume flow rate as well as that for the powder left after the filtration process are shown in Figure 6.2. As can be seen from these images, the size distribution has visually changed, with smaller, more uniform particles appearing in Batch #1 Figure 6.2a, and larger agglomerates in the final sub-grade, Batch #4 Figure 6.2d. These agglomerates are considered to be spheres when undertaking particle size analysis, meaning their size is not

truly representative. This elutriation process, however, has still been shown to be effective for separating size ranges of powders and is now also verified for being of use when trying to remove these larger agglomerates from the bulk powder.

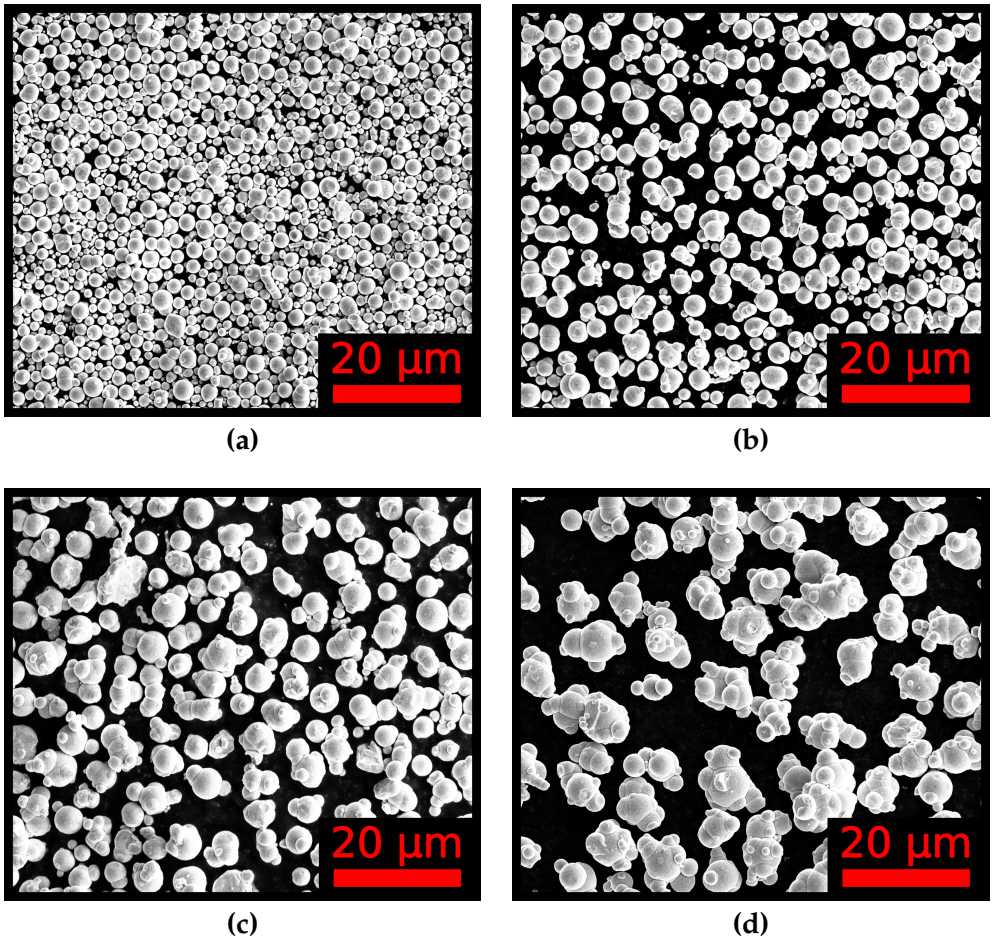

(a) (b) (c) (d)

Figure 6.2: SEM micrographs showing particle sizes for **(a)** particles collected in the second chamber using a volume flow rate of 0.8 LPM, **(b)** particles collected in second chamber when using a volume flow rate of 1.5 LPM, **(c)** particles collected in the second chamber when using a volume flow rate of 2.5 LPM and **(d)** the particles left in the first chamber after all volume flow rates had been used. All images taken with an acceleration voltage of 10 kV and beam current of 0.13 nA, detecting secondary electrons at 5000x magnification.

The results from particle size analysis are shown in Figure 6.3 where a percentage volume for bins of particle sizes as well as a cumulative sum for the size distributions are shown. It is shown that 4 distinct size ranges have been extracted from this single bulk batch of powder. The approximate size ranges as well as the expected mean size from each run of the filtration

process are given in Table 6.2. The expected values for radius are calculated from Equation (6.1) by finding the cutoff for each bottle at the given volume flow rate and taking the mid-point.

Batch No. (Volume Flow Rate)	Predicted Diameter (μm)	Mid-point (μm)	Measured Diameter (d50) (μm)	d10 (μm)	d90 (μm)
Raw	N/a	N/a	3.46 ± 1.76	1.82	5.50
4 Left over	$d \geq 7.34$	N/a	5.90 ± 0.88	3.82	7.70
3 (2.5 LPM)	$2.64 \leq d \leq 7.34$	4.68 ± 0.70	4.50 ± 0.60	3.16	6.18
2 (1.5 LPM)	$2.06 \leq d \leq 5.68$	3.62 ± 0.56	3.42 ± 0.48	2.22	5.46
1 (0.8 LPM)	$1.50 \leq d \leq 4.14$	2.66 ± 0.48	2.34 ± 0.40	1.42	3.06

Table 6.2: Table showing values for the predicted particle size range of each batch of powder filtered using the 2-bottle elutriation filter. Size distributions were determined by SEM analysis, with error given by the FWHM of a skewed Gaussian curve that has been fitted to the size distribution.

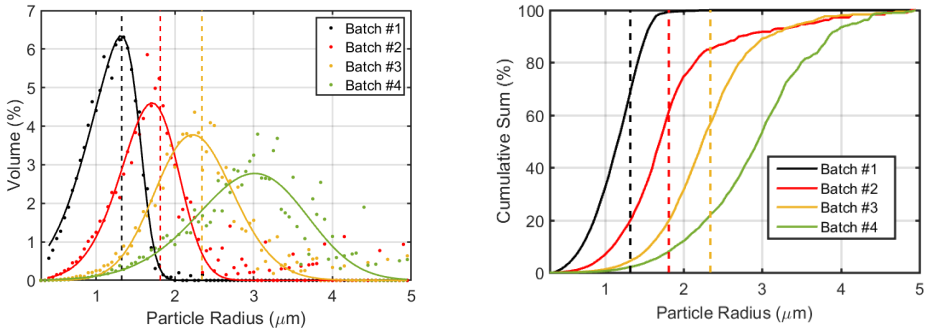

(a) **(b)**

Figure 6.3: **(a)** Particle size distribution for each batch of powder, displayed as a histogram scatter plot with a skewed Gaussian fit to each dataset. These Gaussian curves were used to calulate the FWHM for each curve, allowing an uncertainty to be provided. Dashed lines indicate the expected mean size for each batch, calculated as the midpoint between the cutoffs of the first and second chambers. **(b)** Cumulative sum of the particle size distribution for each batch of powder. Dashed lines again indicate the expected size for this batch, calculated from the midpoint between the cutoffs for the chambers at each volume flow rate.

In order to test repeatability, the experiment was performed again with 30 g of CIP EM and volume flow rates of 0.8, 1.5 and 2.5 LPM. The resulting mean sizes for each sub-grade of powder are in agreement to within 10%.

Batch No. (Volume Flow Rate)	Predicted Diameter (μm)	Mid-point (μm)	Measured Diameter (d50) (μm)	d10 (μm)	d90 (μm)
Raw	N/a	N/a	3.46 ± 1.76	1.82	5.50
4 Left over	$d \geq 7.34$	N/a	5.60 ± 1.63	3.74	7.60
3 (2.5 LPM)	$2.64 \leq d \leq 7.34$	4.68 ± 0.70	5.04 ± 1.30	3.28	6.76
2 (1.5 LPM)	$2.06 \leq d \leq 5.68$	3.62 ± 0.56	3.66 ± 1.06	2.52	4.98
1 (0.8 LPM)	$1.50 \leq d \leq 4.14$	2.66 ± 0.48	2.20 ± 0.76	1.34	3.26

Table 6.3: Table showing values for the predicted particle size range of each batch of powder compared with the results for a repeated filtration of CIP EM particles.

The likely source of discrepancy between experiments is the amount of time air was pumped through the system at each specific volume flow rate.

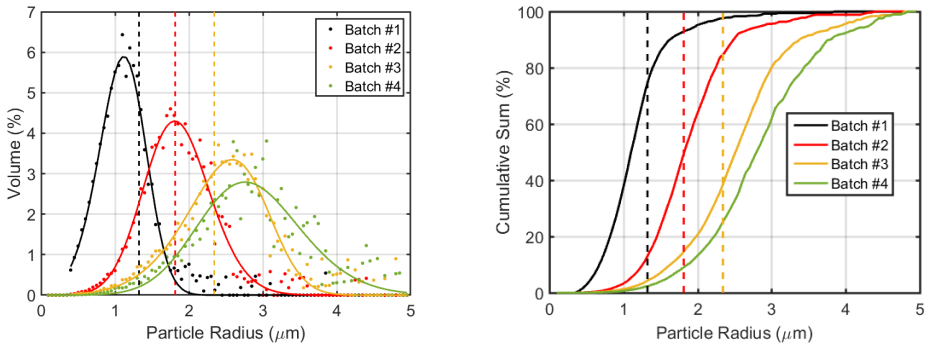

(a) **(b)**

Figure 6.4: **(a)** Particle size distribution and **(b)** cumulative sum of size siztribution for sub-batches of particles filtered from CIP EM in a repeated experiment.

A third elutriation experiment was performed to check the efficacy of this filtration for other similar grades of iron powder. An initial bulk grade of CIP ES was used with again 30 g only using volume flow rates of 0.8 LPM and 1.5 LPM. A comparison of the size distributions for each subgrade from the three experiments is shown for volume flow rates of 0.8 LPM and 1.5 LPM in Figure 6.5.

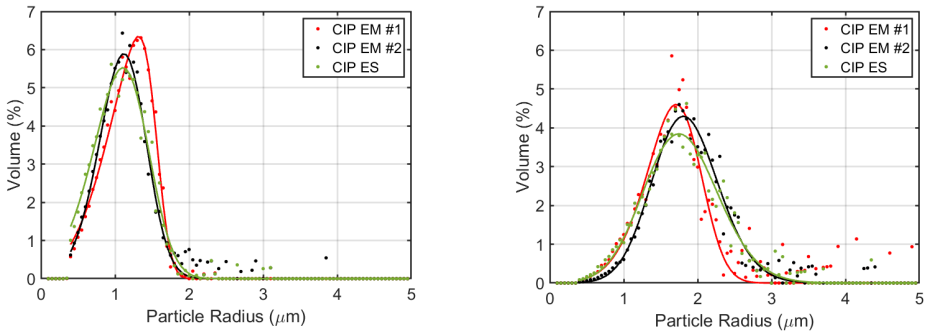

Figure 6.5: Comparisons of the particle size distributions for 3 sub-grades of powder filtered from bulk batches of powder when using elutriation volume flow rates of **(a)** 0.8 LPM and **(b)** 1.5 LPM.

Once the filtration technique had been verified as a viable method for removing the smaller particles from the bulk and collecting them for analysis, it was necessary to explore the effects this change in average particle size had on the electromagnetic properties of composites formed from them. The results for the electromagnetic characterisation of composites formed from these sub-batches is presented in the upcoming section.

6.3.2 Electromagnetic Characterisation

From each of the filtered sub-grades of CIP EM, composites with polyurethane were formed. The volume loading was chosen such that at least 3 samples could be made for measurements from each batch. The samples were cast using the method described in Chapter 4. The table below states the amount of polyurethane and iron powder used for each batch of samples, with an equivalent % volume loading provided. These samples were characterised using the stripline technique to determine their complex index as a function of frequency. The results for the complex index of samples are shown in Figure 6.6 and Figure 6.7.

Samples were all made with similar volume loadings for each sub-grade of CIP EM, and the results for index are shown to vary greatly between each batch. The absorption peak in the imaginary part of the index for Batch #4 samples is a single broad peak, similar to what has been observed in Chapter 4 for CIP ES while the almost triple peak observed for Batch #1 samples

Batch No.	Mass of Powder (g)	Mass of Polyurethane (g)	Percentage Volume Loading (%)
CIP EM #1	3.32	0.96	32.28
CIP EM #1 Repeat	3.32	0.95	32.51
CIP EM #2	3.34	1.00	31.52
CIP EM #2 Repeat	3.36	0.98	32.09
CIP EM #3	3.34	0.98	31.96
CIP EM #3 Repeat	3.12	0.92	31.85
CIP EM #4	3.31	0.95	32.44
CIP EM #4 Repeat	3.34	0.96	32.41

Table 6.4: Table showing the masses for each sub-grade of CIP EM used in each sample batch with the mass of polyurethane used also. See Table 6.2 for the size ranges of each CIP EM sub-grade and Table 6.3 for the size ranges of sub-grades of CIP EM that were filtered using a repeat of the same experiment. Corresponding volume percentage loadings for each batch of samples are also given.

is similar to results for CIPs HS, HQ and the 3rd party 800 nm powder detailed in Chapter 5. These results are also similar to studies performed by others on the size dependence for higher order magnetic modes, where a single broad peak is reduced to 2 or even 3 smaller peaks. One of these peaks relates to the FMR while other peaks are associated with higher order spherical magnetic modes [63].

The refractive index for each sub-grade of powder filtered from the original and repeated experiments agree across the frequency range measured, with slight deviation between batches 1 and 2. The discrepancy between the results for these two sub-batches of powder is due to a difference in the average particle size distributions that is less than 10%, which means that the appearance of these higher order magnetic modes is sensitive to the average particle size of the powder, as well as the distribution of sizes. The imaginary part of refractive index for each sample set made with each sub-grade of CIP EM for both the initial and repeated experiment are directly compared in Figure 6.8.

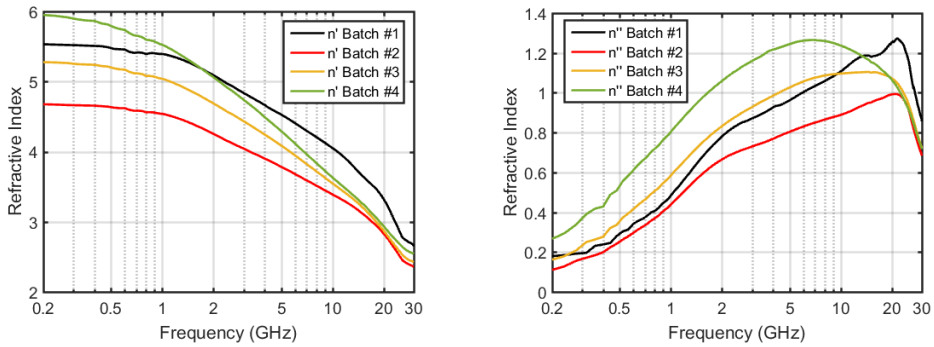

Figure 6.6: Real, **(a)**, and imaginary **(b)** parts of refractive index for composites of polyurethane and the first set of sub-grades for CIP EM, filtered by the elutriation technique.

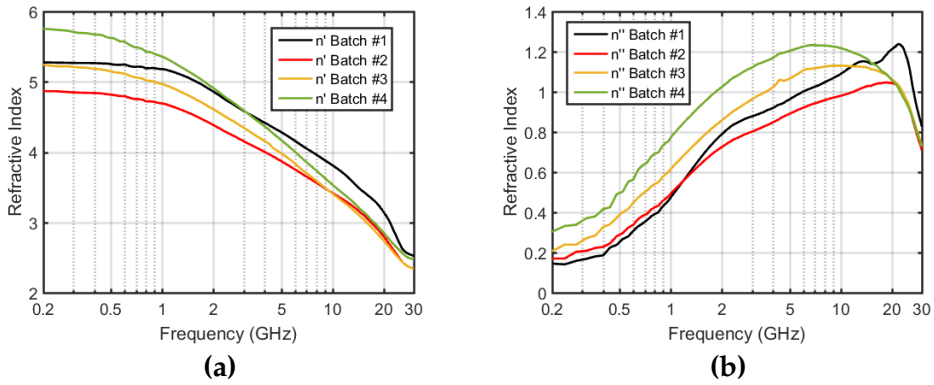

Figure 6.7: Real, **(a)**, and imaginary **(b)** parts of refractive index for composites of polyurethane and the second set of sub-grades for CIP EM, filtered by the elutriation technique in a repeated experiment.

The refractive index loss-tangent and Cole-Cole plots of the real and imaginary parts of index for each of these sets of composites are displayed in Figure 6.9 and Figure 6.10. The data for each of the sets of data agree closely.

The trend of absorption modes becoming more well-defined as particle size distribution decreases is similar to the results displayed in the previous chapter, and are a result of reducing the average particle size of a single grade of powder. This result means one may infer that the emergence of higher order modes is dominated by the average particle size of the powder, rather than other factors in particle fabrication.

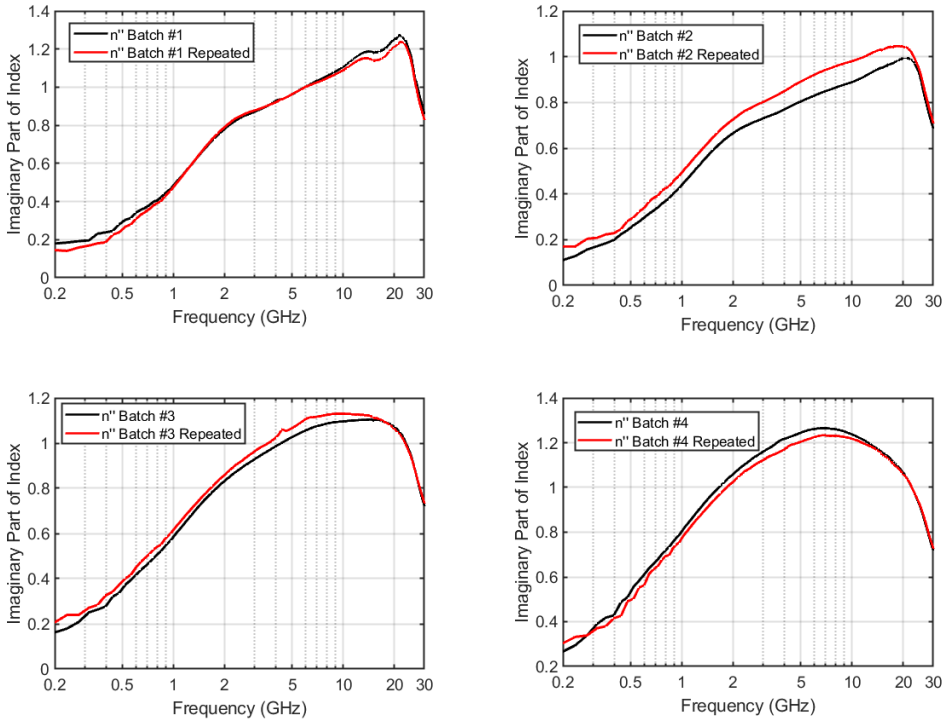

Figure 6.8: Direct comparison of imaginary refractive index for each sub-grade of CIP EM filtered through different experiments.

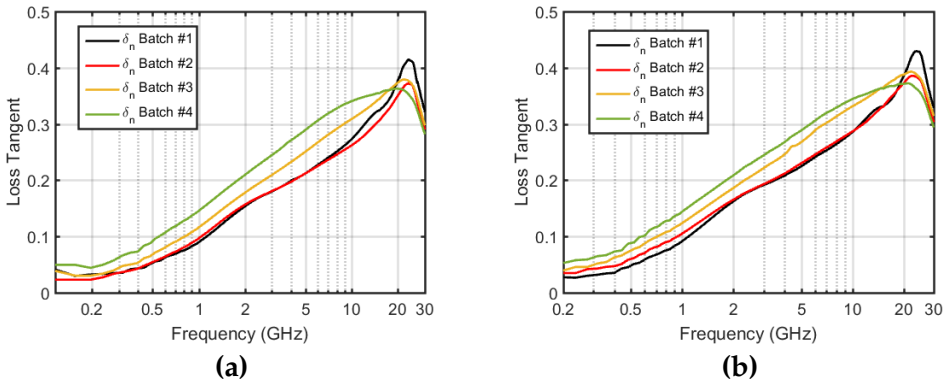

Figure 6.9: Refractive index loss tangent for composites formed from polyurethane and carbonyl iron powder CIP EM that has been split into sub grades by an elutriation technique. **(a)** shows the results for a first attempt of the experiment while **(b)** shows that for a repeated filtration.

6.4 Chapter Summary

A simple technique for separating batches of CIP into sub-batches with different size distributions has been demonstrated. This technique is shown

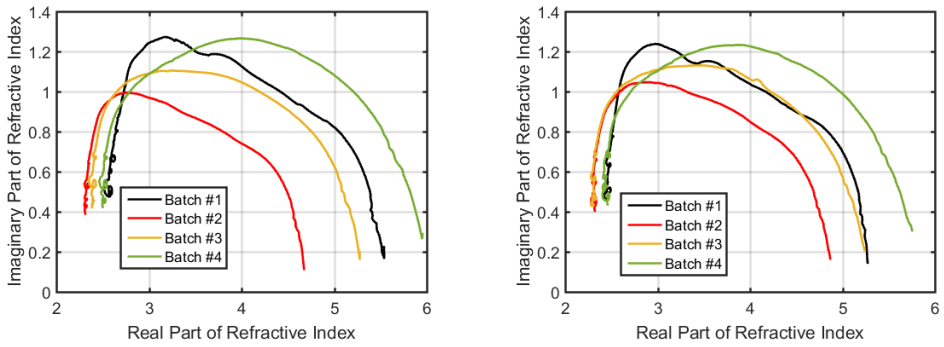

Figure 6.10: Refractive index Cole-Cole plot for composites formed from polyurethane and carbonyl iron powder CIP EM that has been split into sub grades by an elutriation technique. **(a)** shows the results for a first attempt of the experiment while **(b)** shows that for a repeated filtration.

to be viable for separating a powder with particle size distribution 3.46 μm $\pm$1.75 μm into 4 distinct sub-grades centred at 2.97, 2.25, 1.67 and 1.20 μm. The experiment has also been demonstrated for reducing another grade from a size distribution of 2.85 μm $\pm$1.55 μm into distinct sub-batches with size distributions centred at 1.77 and 1.08 μm. The results for all elutriation experiments agree to within 10% of the particle radius extracted at each flow rate. The demonstration of this technique's validity opens the ability to further develop a simple method for filtration of powders by particle size that may have narrower distributions than those that are able to be achieved by simply controlling the growth parameters during fabrication. By developing this technique further, it would be possible to simplify fabrication techniques such that particles may still be produced in large batches for a secondary treatment to give specifically sized grades. This would allow better scalability of production for spherical magnetic powders with specific size ranges or narrow size distributions.

Composites formed from polyurethane mixed with each of these batches have had their complex refractive index analysed as a function of frequency across the range 200 MHz - 30 GHz. These results show an emergence of higher order absorption modes at frequencies above 10 GHz that has already been seen in literature for as-bought CIP grades [30, 33, 127] however there has not yet been a report on the electromagnetic properties for carbonyl iron powder based on filtered particle size distributions from a single

grade. The emergence of these modes as particle size and distribution decrease is similar to results in Chapter 5 and those expected from the theory in Chapter 1, Section 1.1.1. This means one can infer that these higher order modes in different grades of CIP appear in the smaller of these spherical magnetic powders, or are at least more distinct for powders with narrower size distributions, rather than as a result of any other fabrication parameters.

The position of higher order modes in frequency appears to be approximately constant over these size ranges, fixed at $\sim$ 21 GHz and $\sim$ 15 GHz. The frequency at which these modes appear is expected to be heavily dependent on the mean size for the particles. However, the expected dependence of $\frac{1}{R^2}$ will have less sensitivity to size for micron sized particles compared with the drastic size effects seen for particles an order of magnitude smaller. In order to better understand these modes, it is necessary to see how the response of composites formed with sub-micron spherical powders changes as a function of applied DC magnetic bias field. This is covered in the next chapter.

Chapter 7

Effect of DC Magnetic Bias Field on Spherical Magnetic Modes

7.1 Introduction

This chapter contains results for the complex refractive index of carbonyl iron – polyurethane composites when a DC bias field is applied to the samples. This experiment was performed as the well known fundamental FMR for magnetic materials is expected to change intensity and position in frequency as magnetic field is applied [48]. It is expected that the higher order modes in spherical particles are a result of the vortex domain structure, which supports resonances that occur at higher frequencies. As discussed in Chapter 1, Section 1.2.4 there has not been successful simultaneous characterisation of relative permittivity and permeability for magnetic materials as a function of applied magnetic bias field.

The higher order modes presented in previous chapters are not yet observed to have a frequency dependence on externally applied magnetic fields. However, it is expected that the modes should be unaffected by this field, until the point of saturation for all particles is reached, and the vortex domain structure is removed from them. This will then cause a suppression of the higher order modes, giving evidence on the vortex domain structure's role in supporting higher order spherical magnetic modes.

Work has been performed previously for characterising the FMR of thin films and bilayers of magnetic materials as a function of applied DC bias field [128, 129]. However, these techniques tend to involve the use of thin films and application of a perturbation theory for shorted microstrip transmission lines [130, 131] rather than full characterisation for materials as a function of applied field. The transmission line cavity is not completely

filled in these experiments either, meaning the theory is only likely to be viable in the lower frequency regime, typically not higher than 10 GHz. Others have reported the frequency dependent permeability of ferrite materials as a function of applied bias field using a shorted coaxial method or impedance analyser, assuming that the relative permittivity is a constant [132–134]. Here, data is presented for the complex index of materials across the broad frequency range 200 MHz to 30 GHz when a DC bias field has been applied from 0 mT to 330 mT. This work can be improved to provide a full extraction of both relative permittivity and permeabilty from the S-parameter measurements.

7.2 Method

In this experiment, the stripline transmission line was inserted between two poles of an electromagnet. The electromagnet was able to provide a maximum magnetic field of $B = 330$ mT when a current of 6.0 A was running through the solenoids for the poles.The static magnetic field was applied across the stripline fixture in a direction that was perpendicular to the direction of propagation for the time-dependent field applied by the stripline fixture to the sample. The magnetic field was increased incrementally by increasing the current driving the electromagnet from 0.0 A – 6.0 A in 0.5 A increments. Measurements of the S-parameters for samples were recorded at each field setting.

It was necessary to take a set of calibration measurements, described in Chapter 4, for every applied field. This allowed a set of calibration parameters to be made for each field when characterising samples. As before, the index was more accurately extracted for all samples so this data was presented for the investigation. Multiple samples of different thicknesses in the propagation direction were characterised, and the results averaged. For the 800 nm particle composites, percentage volume loadings of 30%vol. and 40%vol. were investigated. Samples created from the second batch of filtered CIP EM presented in the previous chapter were used to provide an investigation into the effect of a DC bias field when looking at composites formed from particles with different size distributions.

The samples characterised in this chapter were those used in the previous chapter, Chapter 6, that had been filtered from CIP EM into 4 sub-grades

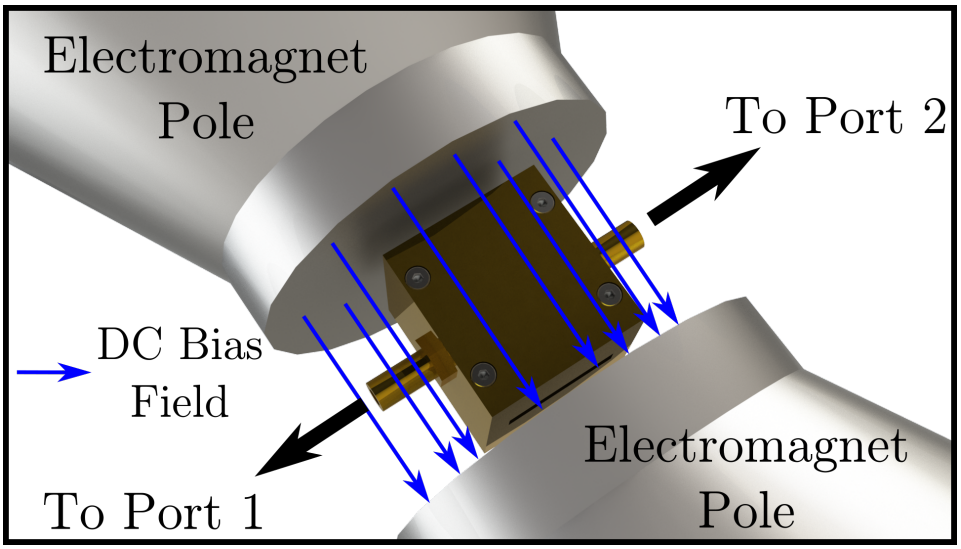

Figure 7.1: Schematic showing the positioning of the stripline device between two poles of an electromagnet for the experiment. DC magnetic bias field is applied perpendicular to wave propagation.

of different average sizes and size distributions. All four of the sample sets from sub-grades of CIP EM were characterised and the results averaged to give refractive index as a function of applied static bias field. These samples had a volume loading of ∼30 %vol. and were investigated to see if any difference in average size would give different behaviour under applied field.

7.3 Results

This section presents the results for how the complex refractive index of samples is changing when a DC bias magnetic field is applied to them. As was explained before, the stripline fixture was found to have a small amount of magnetic material in the brass used for fabricating the device. This meant that the stripline S-parameters changed depending on the field strength used for DC magnetic bias. Figure 7.2 shows the S-parameters for the stripline with zero field and a maximum field of 330 mT applied. Although the change in S-parameters is small, if uncorrected they produce a systematic error in parameter extraction that is discussed in the following pages.

Figure 7.3, below, displays the refractive index for a 30%vol. composite of polyurethane and 800 nm spherical iron particles when using the calibration parameters calculated at zero field to extract sample properties from

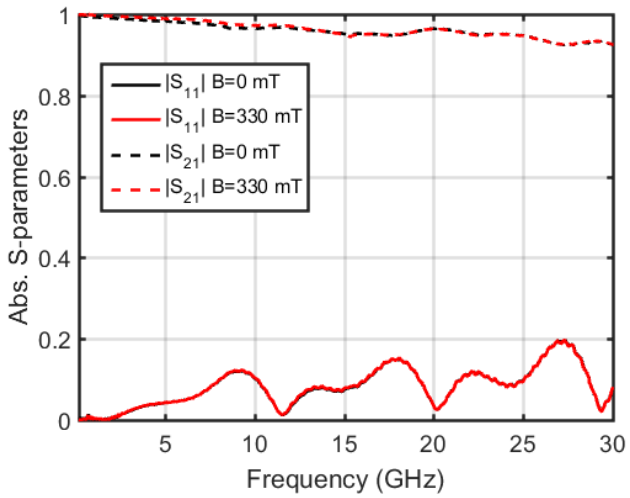

Figure 7.2: Absolute S-parameters for the empty stripline device with and without a magnetic DC bias field applied.

S-parameters measured at maximum field. The imaginary part of refractive index for the sample when subject to a DC magnetic bias field is erroneously extracted as a negative value at low frequencies, indicating that the change in the S-parameters for the empty stripline as a result of applying a DC magnetic bias field although small, is not to be neglected.

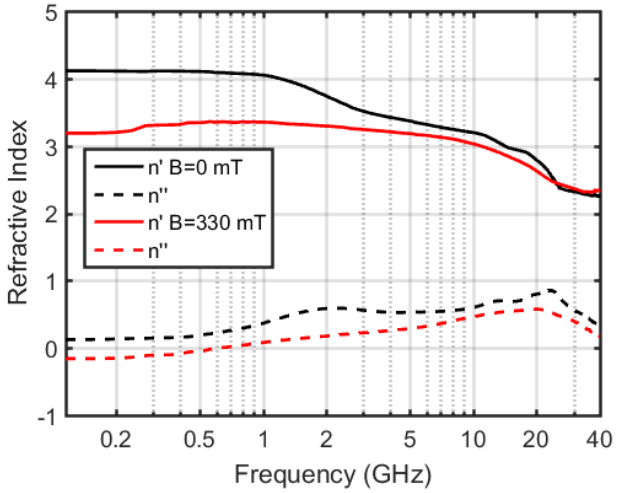

Figure 7.3: Refractive index for a 30%vol. composite containing 800 nm particles as a function of applied DC magnetic bias field, extracted using calibration parameters that were calculated only for the zero-field case.

The imaginary part of refractive index being negative at low frequencies is compensated when using a set of calibration S-parameters that have been calculated for the transition regions from stripline measurements at

all fields. Figure 7.4 shows the refractive index for the same sample as Figure 7.3, only extracted using relevant calibration parameters to the field applied.

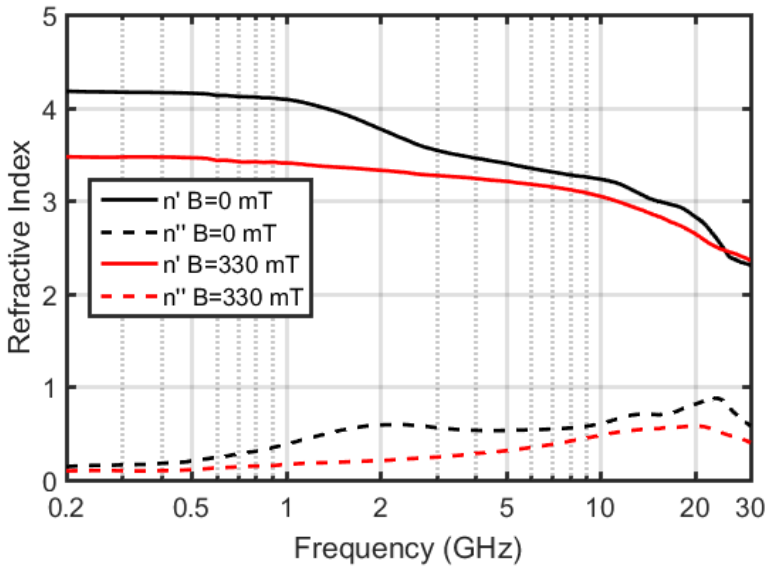

Figure 7.4: Refractive index for a 30%vol. composite containing 800 nm particles as a function of applied DC magnetic bias field, extracted using calibration parameters that were calculated for each applied DC bias field.

The change in S-parameters for the stripline device as the applied DC bias field is changed is as a result of the brass used to fabricate the stripline cavity. The brass used to fabricate the stripline cavity was an alloy with a trace amount of Fe (typically less than 0.5%) added to give ease in processing of the material. This trace amount of iron in the brass is enough to see a measurable affect on the S-parameters when a DC magnetic bias field is applied.

7.3.1 Filtered Particles

First a comparison is made between composites formed with powders of different average size and size distribution. The refractive index for all 4 sets of composites of the sub-grades of CIP EM were characterised with the application of a DC magnetic bias field. Only the refractive index for the composites holding batches #1 and #4 are displayed in this section as the intermediate samples did not exhibit any unexpected behaviour. The refractive index for each of batches #1 and #2 are shown in Figure 7.5 and

Figure 7.6. All four of the index distributions from this analysis share in common the trend of a primary absorption mode at $\sim$ 2 GHz that increases in frequency as applied DC bias field is increased. This absorption mode is associated with the FMR of the iron. The increase in frequency of the position of the primary absorption mode is a result of the increased strain on the magnetic moments that the DC bias field is providing, as has been discussed earlier in Chapter 2. As a field strength of $\sim$ 100 mT is applied to the sample, the higher order modes exhibited by the smallest of the filtered particles are suppressed, being indistinguishable from the FMR mode that approaches 15 GHz.

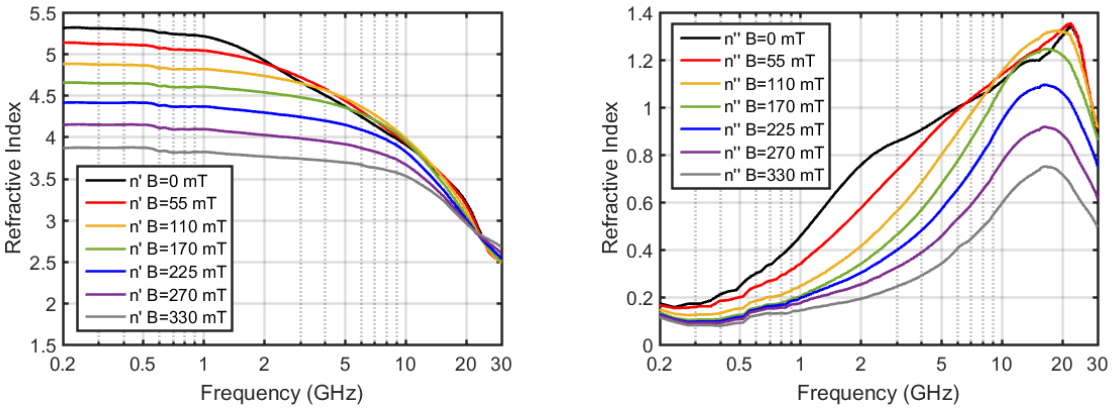

Figure 7.5: Real **(a)**, and imaginary **(b)** parts of refractive index for composites comprising Batch #1 of the filtered particles from CIP EM, plotted with increasing DC magnetic bias field from 0 mT - 330 mT

The static permeability, defined here as the real part of permeability at 200 MHz, for each of these composites as a function of applied DC magnetic bias field is displayed in Figure 7.7. The static permeability decreases as magnetic field strength is increased while the position of the FMR resonance peak is pushed higher in frequency.

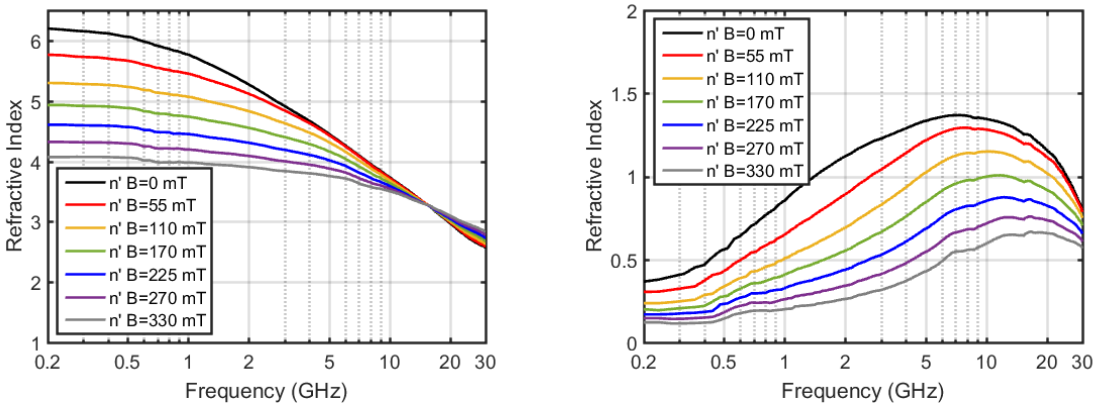

Figure 7.6: Real **(a)**, and imaginary **(b)** parts of refractive index for composites comprising Batch #4 of the filtered particles from CIP EM, plotted with increasing DC magnetic bias field from 0 mT - 330 mT

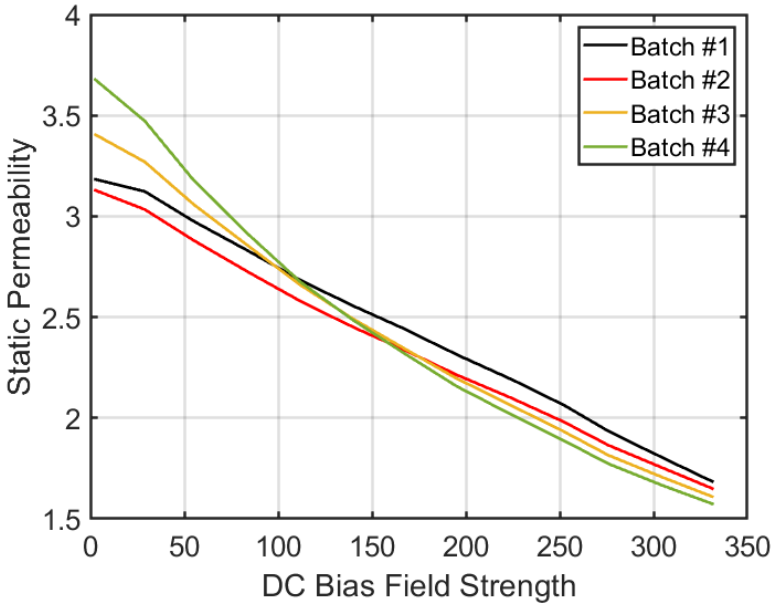

Figure 7.7: Real part of static permeability for each composite formed from the filtered particles plotted as a function of applied DC magnetic bias field strength.

7.3.2 Compared Volume Loading

To investigate the response of composites as a function of applied DC bias field for samples that contained different volume loadings of the sample material, samples with 30%vol. and 40%vol. loadings were compared. These samples comprised 800 nm spherical Fe particles. The results are displayed in this section.

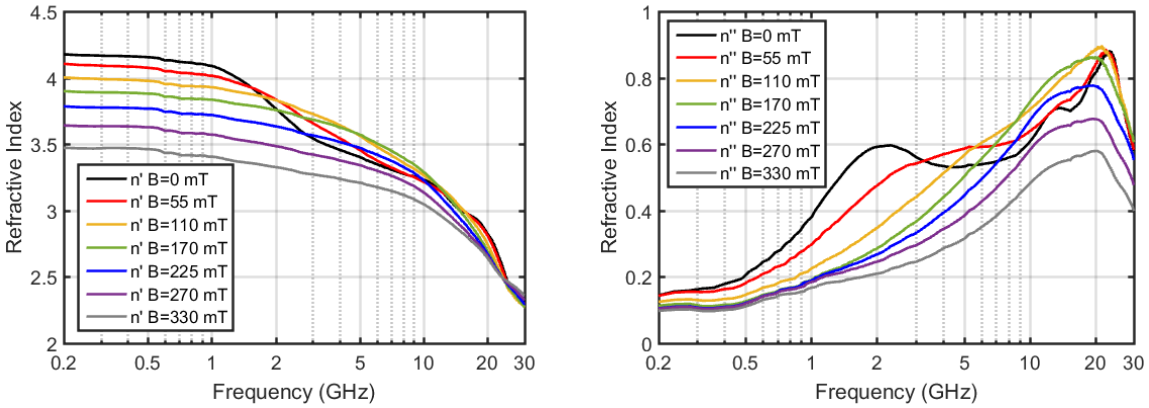

(a) **(b)**

Figure 7.8: Real **(a)**, and imaginary **(b)** parts of refractive index for composites comprising 30%vol. loading of 800 nm iron particles, plotted with increasing DC magnetic bias field from 0 mT - 330 mT

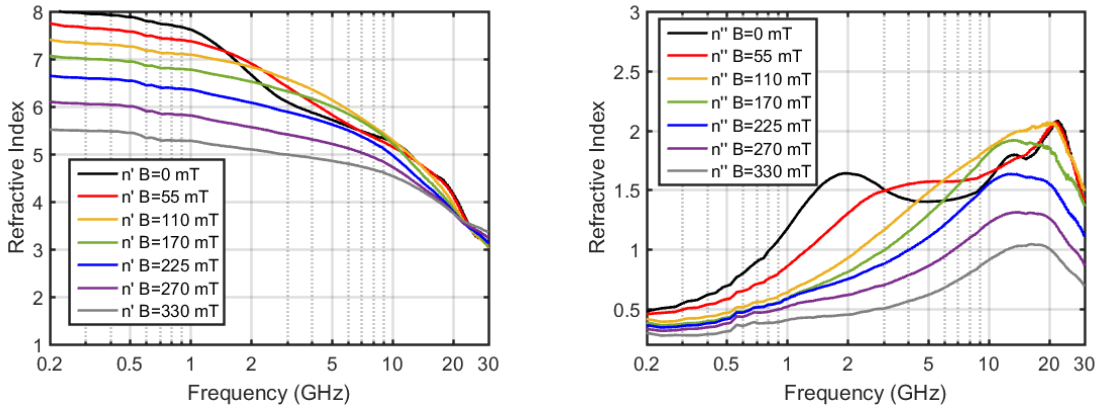

(a) **(b)**

Figure 7.9: Real **(a)**, and imaginary **(b)** parts of refractive index for composites comprising 40%vol. loading of 800 nm iron particles, plotted with increasing DC magnetic bias field from 0 mT - 330 mT

A study into the effect of DC bias field application when using different volume loadings is seen by comparing Figure 7.8 and Figure 7.9. The affect of the applied field appears similar between the two differently loaded sample sets with the exception that the higher order modes observed in the 40%vol. samples appear to become suppressed at a lower field than with the 30%vol. loading samples.

The highest frequency mode, at $\sim$ 20 GHz, appears to be affected more strongly by the DC bias field when using a composite with higher volume loading of magnetic powder. This is likely due to the induced magnetic field inside the composite being higher when there is more magnetic material in the samples, meaning the effective field that is applied is higher than that for the 30%vol. composite. The increase in the internal magnetic field as volume loading is increased may be observed by looking at the static permeability of the composites as a function of applied DC bias field strength. The real part of static permeability as a function of applied field strength is plotted in Figure 7.10. The steeper gradient of the curve for the 40%vol. sample is indicative of the internal field being stronger than it is in the 30%vol. sample.

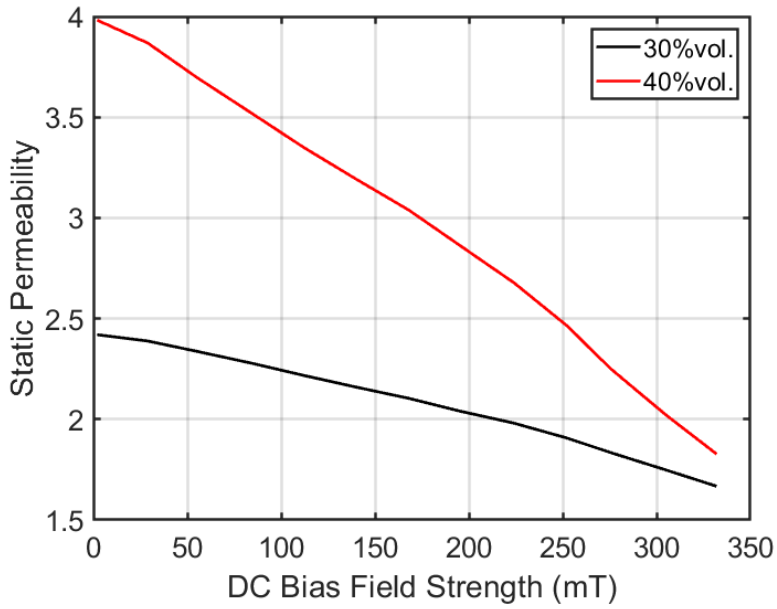

Figure 7.10: Real part of static permeability for each composite formed from the 3rd party 800 nm particles, plotted as a function of applied DC magnetic bias field strength.

7.4 Chapter Summary

The results show that the FMR of composites comprising polyurethane and different micron-sized powders increases with applied bias field, but the higher order modes at $\sim$ 20 GHz appear to remain at the same frequency. These higher order modes close to 20 GHz also appear to change in intensity, with the decrease in absorption at a DC bias field strength of $\sim$ 100 mT indicating the loss of absorption modes above this bias field strength. The higher order modes are expected to be removed upon applying a strong DC bias field as the field will remove the vortex domain structure in these magnetic particles, reducing them to a single domain or onion domain state. Neither the onion state nor the single domain state of these particles is able to support the higher order modes in spherical magnetic powders that have been observed. This indicates that the higher order modes seen in these particles is indeed dependent upon the vortex domain structure that results from their spherical shape. The apparent shift in resonant frequency for higher order modes may be explained by considering that smaller particles would be saturated at lower bias fields than larger particles, meaning the average size of particles with vortex domain state to support higher modes had decreased. The size distribution also would have decreased so an investigation into the behaviour of these modes when the field is changed at signifcantly lower fields may well be of interest to validate further the size dependence of these modes.

The work presented here is novel, reports on the electromagnetic properties for carbonyl iron powders as a function of applied DC bis field have not been seen elsewhere in literature, especially not across the frequency range presented here. The suppression of higher order modes in spherical magnetic powders has not been reported either. However, signifcant theory on the spherical magnetic modes being dependent on the vortex domain state has been reported so this work is valuable for the validation of higher order spherical mode theory.

The comparison of samples with differing volume loadings of magnetic material indicates the need to be able to infer the internal magnetic field that results from the applied external field. This will allow a more rigorous representation of the dependence of these modes on externally applied fields. However, this understanding was outside of the scope for this work, and would only be necessary for application purposes.

Chapter 8

Conclusions and Future Work

The work presented in this thesis considers the results for experiments performed to better understand the nature of higher order magnetic absorption modes in spherical iron powders. The results are presented across 4 experimental chapters that show the progression of the characterisation technique, the characterisation of multiple different spherical iron powders, and advanced characterisation of composites as a function of externally applied static magnetic field. Presented also is a technique for the filtration of spherical iron powders based on their size to investigate the size dependence of these absorption modes. This chapter provides conclusions from each of those experiments as well as possible extensions to the experiments for future work.

The first experimental chapter, Chapter 4, describes the measurement technique used to characterise samples in all of the subsequent chapters. Conventional stripline geometries used a 18 - 20° taper from coaxial geometry to stripline geometry and typically would not have a frequency range of operation exceeding 10 GHz. An optimised stripline device was fabricated that had carefully designed transition regions from coaxial geometry to stripline geometry that were not a standard single angle taper. The improvement in impedance matching for this transition region allowed better measurement of S-parameters for samples. This stripline was used in conjuction with an improved short-measurement calibration technique to extract the S-parameters for dielectric and magnetic samples. Dielectric samples of $BaTiO_3$ in polyurethane were characterised and the permittivity of samples was extracted using both a direct Fresnel theory extraction, calculating relative permittivity on a point-by-point basis, as well as by using a frequency dependent expression of permittivity in conjunction with Fresnel theory to fit to the entire range of S-parameters across the unprecedented

frequency range 0.2 - 50 GHz. Results are also presented in this chapter for the relative permittivity and permeability of samples comprising CIP ES in polyurethane at percentage volume loadings across the range 10 - 40%vol. in 10%vol. increments. All samples used for the thesis were created using a wet-cast technique, mixing the loading powder into a 2 part polyurethane mixture and curing in a suitable mould for the stripline geometry. The relative permittivity for dielectric samples was shown to have a logarithmic dependence on the volume loading, as was the case for CIP ES composites. This is in agreement with standard mixing laws, and also applied to the static relative permeability of CIP ES composites. The imaginary relative permeability of CIP ES composites showed a single broadband absorption mode that is likely a result of the wide size-distribution of the powder causing mutliple broad resonances to be supported. The degeneracy inherent in the extraction of impedance is discussed in this chapter, and highlights the uncertainty in extraction of relative permittivity and permeability for composites when samples are either not fabricated precisely enough, or permeability is close to unity. For this reason the refractive index, rather than the permittivity and permeability, is used to characterise samples for the rest of the thesis. The technique developed in this chapter has brought with it the ability to now consider the investigation of modes in magnetic materials that are significantly higher in frequency than have been able to be observed with previous techniques whilst still allowing an investigation into the response of the same magnetic materials at radio frequencies in a single measurement. The versatility of this technique may be pushed further by attempting measurements of magnetic materials as a function of temperature, taking a calibration reading of the stripline at fixed temperatures in a controlled environment before measuring the S-parameters of the stripline with magnetic composites inserted at different temperatures. This information would be invaluable for companies looking to use magnetic materials in communications applications as the performance of antennas at different temperatures is vital knowledge. It may also be possible to create a stripline that is capable of being used over an even more broadband frequency range for the investigation of particles that are in the size range of 100 nm. These smaller particles are expected to have resonances at frequencies even higher than the range that has been investigated in this thesis. Coaxial adapters are available with a dielectric region that has diameter 1 mm. These adapters have a recommended maximum frequency of 110 GHz,

meaning it is possible to fabricate a new stripline device for characterisation up to these frequencies. This device would require significantly more precision in sample manufacture to ensure a tight fit in the 1 mm tall stripline cavity. However, these S-parameter measurements may also be used in conjunction with those taken at lower frequencies with the 3 mm tall stripline, as well as higher frequency measurements taken using the waveguide to planewave adapters briefly described in Chapter 4, Section 4.4.

The second experimental chapter, Chapter 5, details results for the characterisation of 9 different grades of commercially available carbonyl iron powder as well as an incomplete investigation into the properties of composites comprised of 100 nm Fe particles in polyurethane. The carbonyl iron powders each had different particle size distributions, as well as different microstructures, and a single powder with a coating that has been assumed to be phosphate. The characterisation of each of these grades of powder involved confirming the internal structure of powders by cross-sectional analysis and SEM, as well as measuring the particle-size distribution by SEM analysis. Different methods for investigating the cross-section of powders as well as the particle-size distribution are discussed, and the final methods used were described. The final method for investigation of particle cross-sections involved polishing an epoxy loaded with carbonyl iron before etching the microstructure of particles with 2% nital etchant. The final method for particle-size analysis was by SEM analysis, imaging the particles directly and using image processing software to infer particle sizes from the images. This chapter highlighted the strong dependence of absorption modes on particle size distribution for the powders, and it was concluded that an additional investigation into the smaller particles was required. The analysis of composites containing 100 nm spherical Fe particles demonstrated that higher order modes were still supported in these smaller particles, but an extensive investigation was not able to be completed as the samples produced could not be ensured to have homogeneously dispersed particles and were of a low structural quality for characterisation. Future work on the investigation of magnetic nanopowders involve improving the sample fabrication technique to ensure nanoparticles have been well dispersed in the polymer matrix of composites. This will allow a deeper investigation into the size dependence of these modes in spherical iron powders. The results also highlighted a necessity to produce a technique for filtration of sub-micron sized particles.

To investigate the effect of size distribution on higher order absorption modes, a technique for filtering particles of different size ranges from a single grade of powder was required such that other nuances in manufacture may be isolated. This particle size filtration was the focus of the third experimental chapter, Chapter 6. The experiment demonstrates an ability to reliably remove the smallest particles from a bulk powder before showing that a second collection chamber may be used to capture the removed particles for fabrication of composites. A grade of CIP with an average particle size of $R = 1.73 \pm 0.88$ μm was separated into 4 batches with average particle sizes of $R_1 = 1.20 \pm 0.40$ μm, $R_2 = 1.67 \pm 0.48$ μm, $R_3 = 2.25 \pm 0.60$ μm and $R_4 = 2.97 \pm 0.88$ μm. This separation technique for carbonyl iron powders had been achieved for particle sizes significantly smaller than those previously reported in literature, and allow access to filtration of particles significantly smaller than are able to be filtered by standard sieves. This filtration process is also the first for this scale of filtration of carbonyl iron powders such that composites could be formed for characterisation. The characterisation of composites formed from these sub-grades of powder showed that higher order absorption modes were more well-defined in composites containing the smaller particles, and a comparison of the refractive index for each composite showed a transition from one broad absorption mode into 3 distinct absorption modes. The results presented in this chapter were promising as a proof of concept for methodology in simple filtration of particles by size, but did have areas where great improvement could be made. For example reducing the occurrance of jets of powder passing through the system would likely improve the filtration such that even narrower distributions of powder were attained. The results for electromagnetic properties of powders with the smallest average size also lead to a desire for filtration of particles that are in the 100 nm size regime. Future work for improvement of the elutriation technique could be as follows. The primary issue with filtering nanoparticles with this trechnique is that the volume air flow rate needs to be significantly lower than has been used in Chapter 6. This low volume air flow rate would not be capable of agitating bulk amounts of powder to form dust clouds for separation. If one were to attempt filtration with a lower volume flow rate and a smaller amount of powder in the chamber to allow dust cloud formation, there arises the issue of needing to repeat the experiment an unreasonable number of times to produce the required amount of powder for composite manufacture.

An alternative design to the experimental setup has been proposed that would allow bulk powder to be fed into the chamber at a steady rate, such that larger batches of powder may be processed in a single experiment. A diagram of this alternative design is displayed in Figure 8.1. The improved design has an additional cup in the filtration chamber, that has an inlet for the bulk powder. By using a syringe pump, and a syringe loaded with the bulk powder, it should be possible to feed the powder into the setup at a gradual rate, such that the flow of air is able to lift the particles into a dust cloud.

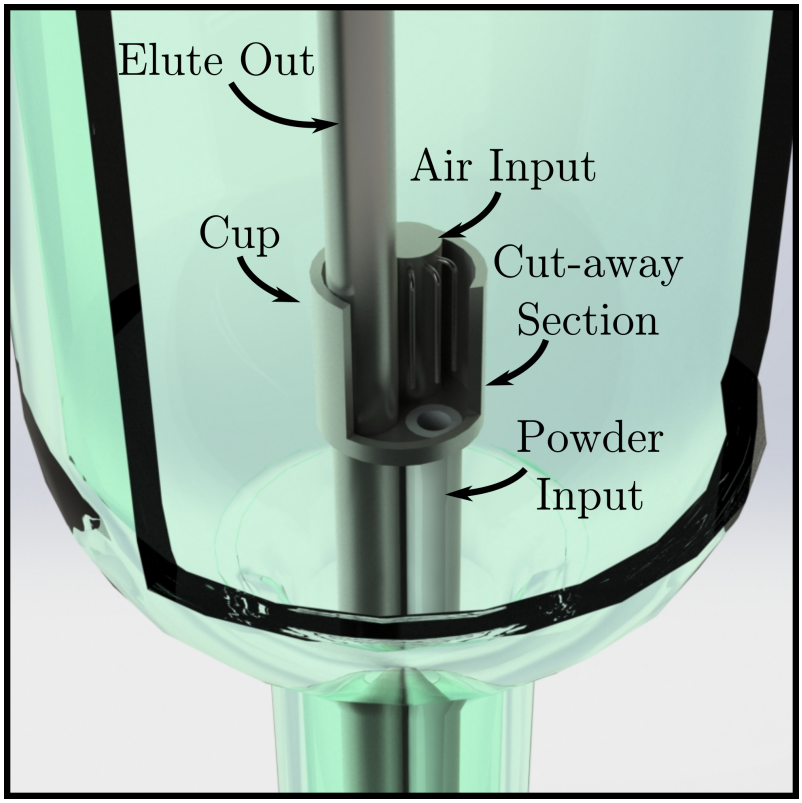

Figure 8.1: Diagram showing a possible improvement to the current air elutriation experiment. A cup would be used to allow a powder to be fed into the system, and the low volume air flow rate will be able to lift the input powder into a dust cloud.

As well as the issue of forming dust clouds from the smaller powders, there exists the issue of agglomerated particles needing to be broken up during the filtration. This isn't entirely necessary for the extraction of sub-micron powders, but will increase the yield if agglomeration of sub-micron sized particles is prevalent in the bulk. Another method for filtration of particles based on size using air is by cyclonic separation. This process is similar

to air elutriation in that an air flow carries the particles through chambers for filtration, only the flow is cyclonic rather than laminar. This involves the use of significantly higher volume flow rates of air, and the particles experience significantly more turbulence, causing agglomerates to be broken up during filtration.

The higher order absorption modes are expected to be a result of the vortex domain structure of spherical particles. To confirm the domain structure of these particles, a final investigation into the dependence of these higher order modes on an externally applied magnetic field was undertaken. The fourth experimental chapter, Chapter 7, exhibits results for the refractive index of composites containing the filtered particles, as well as composites containing 800 nm spherical iron particles while the composites were subject to an externally applied DC magnetic bias field. The results showed that the primary FMR absorption mode was heavily dependent on the strength of the externally applied field, whereby the frequency at which this mode occured would increase with applied field strength. The position in frequency of higher order absorption modes was not affected by the external field, but the strength did appear to be. The higher order absorption modes weakened as the field strength was increased, which was indicative of particles being saturated at high field strengths, losing their vortex domain structure and, with it, the ability to support higher order absorption modes. This result was used to conclude that the domain structure of spherical iron powders was indeed the vortex structure, and that this structure is necessary to support higher order magnetic absorption modes. The results presented in this chapter have not been found elsewhere in literature, as the broadband characterisation of composite materials as a function of DC magnetic bias field has previously been limited to low frequency meaesurements. Also the higher frequency measurement techniques involving coplanar waveguide transmission absorption, briefly discussed in Chapter 1, Section 1.2.4 may only be used to infer the location and width of modes rather than the electromagnetic properties of the particles. This experiment is currently limited in that the fabrication of the stripline involved use of slightly magnetic materials, so the simultaneous extraction of relative permittivity and permeability was unable to be completed. An improvement to the stripline fixture would be to ensure that the brass used for fabrication of the device did not contain any magnetic material. Also it is necessary to develop a method for

inferring the internal fields of the composite materials such that an analytical theory for the behaviour of these modes under DC magnetic bias field may be directly compared.

The work in this thesis has demonstrated the ability to preform broadband frequency characterisation of composite samples across the range 0.2 - 50 GHz. This method has limitations in characterisation that are related to sample manufacture and precision in the experimental technique. The method has been applied to explore higher order spherical absorption modes in CIP loaded composites that have long been observed but have not been fully understood. This work has been performed in conjunction with a thesis project, performed by C. Mckeever at The University of Exeter, concerning modelling these higher order spherical modes to better understand how they may be exploited. This work has not yet been published.

Bibliography

[1] L. Yousefi, B. Mohajer-Iravani, and O. M. Ramahi. "Enhanced Bandwidth Artificial Magnetic Ground Plane for Low-Profile Antennas". In: *IEEE Antennas and Wireless Propagation Letters* 6.3 (2007), pp. 289–292. ISSN: 1536-1225. DOI: 10.1109/LAWP.2007.895282.

[2] L. Parke et al. "Broadband impedance-matched electromagnetic structured ferrite composite in the megahertz range". In: *Applied Physics Letters* 104.22 (2014), p. 221905. ISSN: 0003-6951. DOI: 10.1063/1.4881186.

[3] Y. Shirakata et al. "High Permeability and Low Loss Ni–Fe Composite Material for High-Frequency Applications". In: *IEEE Transactions on Magnetics* 44.9 (2008), pp. 2100–2106. ISSN: 0018-9464. DOI: 10.1109/TMAG.2008.2001073.

[4] L. Parke et al. "Heavily loaded ferrite-polymer composites to produce high refractive index materials at centimetre wavelengths". In: *APL Materials* 1.4 (2013), p. 042108. ISSN: 2166532X. DOI: 10.1063/1.4824039.

[5] L. Parke. "Controlling the Electromagnetic Properties of Magnetic Composites and Metamaterials". PhD thesis. University of Exeter 2015.

[6] S. Mori et al. "High permeability and low loss of Ni-Zn-Fe ferrite/metal composite cores in high frequency region". In: *AIP Advances* 7.5 (2017), p. 056657. ISSN: 2158-3226. DOI: 10.1063/1.4976945.

[7] A. Goldman. *Modern Ferrite Technology*. 2010. ISBN: 9781441939227.

[8] A. Aharoni. "Exchange resonance modes in a ferromagnetic sphere". In: *Journal of Applied Physics* 69.11 (1991), pp. 7762–7764. ISSN: 0021-8979. DOI: 10.1063/1.347502.

[9] P. Toneguzzo et al. “Observations of exchange resonance modes on submicrometer sized ferromagnetic particles”. In: *Journal of Applied Physics* 81.8 (1997), p. 5546. ISSN: 00218979. DOI: 10.1063/1.364657.

[10] C. McKeever, F. Y. Ogrin, and M. M. Aziz. “Influence of surface anisotropy on exchange resonance modes in spherical shells”. In: *Journal of Physics D: Applied Physics* 51.30 (2018), p. 305003. ISSN: 0022-3727. DOI: 10.1088/1361-6463/aacd5b.

[11] A. Aharoni. “Exchange Resonance Modes in a Hollow Sphere”. In: *physica status solidi (b)* 231.2 (2002), pp. 547–553. ISSN: 0370-1972. DOI: 10.1002/1521-3951(200206)231:2<547::AID-PSSB547>3.0.CO;2-7.

[12] D. Betto and J. M. D. Coey. “Vortex state in ferromagnetic nanoparticles”. In: *Journal of Applied Physics* 115.17 (2014), p. 17D138. ISSN: 0021-8979. DOI: 10.1063/1.4867597.

[13] F. Alouges, S. Faure, and J. Steiner. “The vortex core structure inside spherical ferromagnetic particles”. In: *Discrete and Continuous Dynamical Systems* 27.4 (2010), pp. 1259–1282. ISSN: 1078-0947. DOI: 10.3934/dcds.2010.27.1259.

[14] C. McKeever. “High Frequency Dynamics of Nanomagnetic Particles”. PhD thesis. University of Exeter 2019 *to be published.*

[15] C. G. Goetzel. “Treatise on powder metallurgy”. In: *Journal of the Franklin Institute* 277.4 (1964), p. 367. ISSN: 00160032. DOI: 10.1016/0016-0032(64)90463-6.

[16] K. C. Hsu, C. C. Lin, and G. M. Lo. “The Effect of Wax Composition on the Injection Molding of Carbonyl Iron Powder with LDPE”. In: *Canadian Metallurgical Quarterly* 35.2 (1996), pp. 181–187. ISSN: 0008-4433. DOI: 10.1179/cmq.1996.35.2.181.

[17] M. Bloemacher and D. Weinand. “CatamoldTM-A new direction for powder injection molding”. In: *Journal of Materials Processing Technology* 63.1-3 (1997), pp. 918–922. ISSN: 09240136. DOI: 10.1016/S0924-0136(96)00014-3.

[18] D. I. Bloemacher. “Carbonyl iron powders: Its production and new developments”. In: *Metal Powder Report* 45.2 (1990), pp. 117–119. ISSN: 00260657. DOI: 10.1016/S0026-0657(10)80122-5.

[19] L. Zhao et al. "Application of Carbonyl Iron Powder as a Novel Mediator for Arterial Embolization Hyperthermia—Feasibility Investigation". In: *IFMBE Proceedings*. 2009, pp. 172–175. ISBN: 978-3-642-03886-0. DOI: 10.1007/978-3-642-03887-7_47.

[20] D. Li et al. "Magnetic Arterial Embolization Hyperthermia Mediated by Carbonyl Iron Powder for Liver Carcinoma". In: *IFMBE Proceedings 39*. 2013, pp. 1624–1627. DOI: 10.1007/978-3-642-29305-4_426.

[21] V. R. Gordeuk et al. "Carbonyl iron therapy for iron deficiency anemia." In: *Blood* 67.3 (1986), pp. 745–52. ISSN: 0006-4971.

[22] Q. Zhu et al. "Effects of carbonyl iron powder on iron deficiency anemia and its subchronic toxicity". In: *Journal of Food and Drug Analysis* 24.4 (2016), pp. 746–753. ISSN: 10219498. DOI: 10.1016/j.jfda.2016.04.003.

[23] L. Delisle. "A Method of Examination of Sections of Fine Metal Powder Particles with the Electron Microscope". In: March (1949), pp. 1–5.

[24] P. Toneguzzo et al. "Monodisperse Ferromagnetic Particles for Microwave Applications". In: *Advanced Materials* 10.13 (1998), pp. 1032–1035. ISSN: 0935-9648. DOI: 10.1002/(SICI)1521-4095(199809)10:13<1032::AID-ADMA1032>3.0.CO;2-M.

[25] D. Mercier et al. "Magnetic resonance in spherical Co-Ni and Fe-Co-Ni particles". In: *Physical Review B: Condensed Matter and Materials Physics* 62.1 (2000), pp. 532–544. ISSN: 0163-1829. DOI: 10.1103/PhysRevB.62.532.

[26] G. W. Hanson, J. M. Grimm, and D. P. Nyquist. "An improved deembedding technique for the measurement of the complex constitutive parameters of materials using a stripline field applicator". In: *IEEE Transactions on Instrumentation and Measurement* 42.3 (1993), pp. 740–745. ISSN: 00189456. DOI: 10.1109/19.231600.

[27] W. Barry. "A Broad-Band, Automated, Stripline Technique for the Simultaneous Measurement of Complex Permittivity and Permeability". In: *IEEE Transactions on Microwave Theory and Techniques* 34.1 (1986), pp. 80–84. ISSN: 0018-9480. DOI: 10.1109/TMTT.1986.1133283.

[28] E. Salahun et al. “A broadband permeameter for "in situ" measurements of rectangular samples”. In: *IEEE Transactions on Magnetics* 37.4 (2001), pp. 2743–2745. ISSN: 00189464. DOI: 10.1109/20.951293.

[29] S. Gómez et al. “Asymmetrical stripline based method for retrieving the electromagnetic properties of metamaterials”. In: *Journal of Applied Physics* 113 (2013), p. 024912. ISSN: 00218979. DOI: 10.1063/1.4775721.

[30] M. A. Abshinova et al. “Correlation between the microstructure and the electromagnetic properties of carbonyl iron filled polymer composites”. In: *Composites Part A: Applied Science and Manufacturing* 38.12 (2007), pp. 2471–2485. ISSN: 1359835X. DOI: 10.1016/j.compositesa.2007.08.002.

[31] V. A. Zhuravlev, V. I. Suslyaev, and E. Yu Korovin. “Dynamic Magnetic Characteristics of a Composite Polymeric Material Based on Carbonyl Iron”. In: *Russian Physics Journal* 53.5 (2010), pp. 541–543. ISSN: 10648887. DOI: 10.1007/s11182-010-9456-4.

[32] Y. Duan et al. “Electromagnetic properties of carbonyl iron and their microwave absorbing characterization as filler in silicone rubber”. In: *Bulletin of Materials Science* 33.5 (2010), pp. 633–636. ISSN: 02504707. DOI: 10.1007/s12034-010-0096-7.

[33] A. N. Lagarkov et al. “High-frequency modes in magnetic spectra of carbonyl iron”. In: *Journal of Magnetism and Magnetic Materials* 324.21 (2012), pp. 3402–3405. ISSN: 03048853. DOI: 10.1016/j.jmmm.2012.02.052.

[34] G. Walther et al. “Properties and sintering behaviour of fine spherical iron powders produced by new hydrogen reduction process”. In: *Powder Metallurgy* 57.3 (2014), pp. 176–183. ISSN: 0032-5899. DOI: 10.1179/0032589914Z.000000000178.

[35] S. W. Andrews et al. “Limitations of laser diffraction for measuring fine particles in oligotrophic systems: Pitfalls and potential solutions”. In: *Water Resources Research* 47.5 (2011), pp. 1–12. ISSN: 00431397. DOI: 10.1029/2010WR009837.

[36] K. W. Lee and B. Y. H. Liu. "On the Minimum Efficiency and the Most Penetrating Particle Size for Fibrous Filters". In: *Journal of the Air Pollution Control Association* 30.4 (1980), pp. 377–381. ISSN: 0002-2470. DOI: 10.1080/00022470.1980.10464592.

[37] Quantum Design. "Introduction to: Broadband FMR Spectroscopy Magnetization dynamics: Landau-Lifshitz-Gilbert Equation Introduction to: Broadband FMR Spectroscopy". In: *Application Note 1087-201* Rev. A0 (2017), pp. 1087–201.

[38] S. S. Kalarickal et al. "Ferromagnetic resonance linewidth in metallic thin films: Comparison of measurement methods". In: *Journal of Applied Physics* 99.9 (2006), p. 093909. ISSN: 0021-8979. DOI: 10.1063/1.2197087.

[39] J. Stöhr and H. C. Siegmann. *Magnetism: From Fundamentals to Nanoscale Dynamics*. 2006. ISBN: 9786540302824.

[40] S. Saremi-Yarahmadi et al. "Fabrication of nanostructured α-Fe2O3 electrodes using ferrocene for solar hydrogen generation". In: *Materials Letters* 63.5 (2009), pp. 523–526. ISSN: 0167577X. DOI: 10.1016/j.matlet.2008.11.011.

[41] E. P. Wohlfarth. *Ferro-magnetic Materials: A handbook on the properties of magnetically ordered substances*. 1980. ISBN: 9780444853127.

[42] J. M. D. Coey. *Magnetism and Magnetic Materials*. Vol. 1. 2009. ISBN: 9787301249796.

[43] E. Koch. "Exchange Mechanisms". In: *Correlated Electrons: From Models to Materials Modeling and Simulation*. Vol. 2. 2012. Chap. 7, pp. 7–20. ISBN: 9783893367962.

[44] D. C. Mattis. *The Theory of Magnetism Made Simple*. 2006. ISBN: 9812386718.

[45] N. L. Schryer and L. R. Walker. "The motion of 180° domain walls in uniform dc magnetic fields". In: *Journal of Applied Physics* 45.12 (1974), p. 5406. ISSN: 00218979. DOI: 10.1063/1.1663252.

[46] A. Hubert and R. Schäfer. *Magnetic Domains: The Analysis of Magnetic Microstructures*. 1998. ISBN: 9783540641087.

[47] N. A. Spaldin. *Magnetic Materials: Fundamentals and Applications*. Vol. 2. 2. 2010, p. 0. ISBN: 1139491555. DOI: 10.1517/13543784.7.5.803. arXiv: 1011.1669.

[48] C. Kittel. "On the theory of ferromagnetic resonance absorption". In: *Physical Review* 73.2 (1948), pp. 155–161. ISSN: 0031899X. DOI: 10.1103/PhysRev.73.155.

[49] G. S. Smith. "A simple derivation for the skin effect in a round wire". In: *European Journal of Physics* 35.2 (2014). ISSN: 13616404. DOI: 10.1088/0143-0807/35/2/025002.

[50] C. Kittel. "Ferromagnetic Resonance". In: *Journal de Physique et le Radium* 12.3 (1951), pp. 291–302. ISSN: 0368-3842. DOI: 10.1051/jphysrad:01951001203029100.

[51] J. H. Van Vleck. "Concerning the Theory of Ferromagnetic Resonance Absorption". In: *Physical Review* 78.3 (1950), pp. 266–274. ISSN: 0031-899X. DOI: 10.1103/PhysRev.78.266.

[52] T. Tsutaoka. "Frequency dispersion of complex permeability in Mn–Zn and Ni–Zn spinel ferrites and their composite materials". In: *Journal of Applied Physics* 93.5 (2003), p. 2789. ISSN: 00218979. DOI: 10.1063/1.1542651.

[53] J.L. Snoek. "Dispersion and absorption in magnetic ferrites at frequencies above one Mc/s". In: *Physica* 14.4 (1948), pp. 207–217. ISSN: 00318914. DOI: 10.1016/0031-8914(48)90038-X.

[54] V. Sharma, S. Kumari, and B. K. Kuanr. "Rare earth doped M-type hexaferrites; ferromagnetic resonance and magnetization dynamics". In: *AIP Advances* 8.5 (2018), p. 056232. ISSN: 2158-3226. DOI: 10.1063/1.5007297.

[55] S. D. Yoon and C. Vittoria. "Microwave and magnetic properties of barium hexaferrite films having the c-axis in the film plane by liquid phase epitaxy technique". In: *Journal of Applied Physics*. Vol. 93. 10 3. American Institute of Physics, 2003, pp. 8597–8599. DOI: 10.1063/1.1557791.

[56] C. Saka, K. Shiiki, and K. Shinagawa. "Simulation of domain structure for magnetic thin film in an applied field". In: *Journal of Applied Physics* 68.1 (1990), pp. 263–268. ISSN: 0021-8979. DOI: 10.1063/1.347126.

[57] G. Tong et al. "Grinding speed dependence of microstructure, conductivity, and microwave electromagnetic and absorbing characteristics of the flaked Fe particles". In: *Journal of Materials Research* 26.05 (2011), pp. 682–688. ISSN: 0884-2914. DOI: 10.1557/jmr.2011.18.

[58] Y. C. Chen et al. "Ferromagnetic resonance study of thickness-dependent magnetization precession in Ni80Fe20 films". In: *Journal of Applied Physics* 101.9 (2007), p. 09C104. ISSN: 0021-8979. DOI: 10.1063/1.2711072.

[59] M. Sharma and S. Pathak. "FMR Measurements of Magnetic Nanostructures". In: *Ferromagnetic Resoance - Theory and Applications* (2013), pp. 93–110. DOI: 10.5772/56615.

[60] J. Ding et al. "Higher order vortex gyrotropic modes in circular ferromagnetic nanodots". In: *Scientific Reports* 4.1 (2015), p. 4796. ISSN: 2045-2322. DOI: 10.1038/srep04796.

[61] D. Goll, A. E. Berkowitz, and H. N. Bertram. "Critical sizes for ferromagnetic spherical hollow nanoparticles". In: *Physical Review B - Condensed Matter and Materials Physics* 70.18 (2004), pp. 1–10. ISSN: 01631829. DOI: 10.1103/PhysRevB.70.184432.

[62] G. Viau et al. "Preparation and microwave characterization of spherical and monodisperse Co20Ni80 particles". In: *Journal of Applied Physics* 76.10 (1994), pp. 6570–6572. ISSN: 00218979. DOI: 10.1063/1.358473.

[63] G. Viau et al. "Size dependence of microwave permeability of spherical ferromagnetic particles". In: *Journal of Applied Physics* 81.6 (1997), pp. 2749–2754. ISSN: 00218979. DOI: 10.1063/1.363979.

[64] C. Mckeever, F. Y. Ogrin, and M. M. Aziz. "Dynamic susceptibility of concentric permalloy rings with opposite chirality vortices". In: *Journal of Applied Physics* 121 (2017). DOI: 10.1063/1.4983759.

[65] F. Butler and K. Banerjee. "Single-Domain Grain Size Limits for Metallic Iron". In: *Journal of Geophysical Research* 80.2 (1975), pp. 252–259.

[66] A. R. Muxworthy and W. Williams. "Critical single-domain grain sizes in elongated iron particles: implications for meteoritic and lunar magnetism". In: *Geophysical Journal International* 202.1 (2015), pp. 578–583. ISSN: 0956-540X. DOI: 10.1093/gji/ggv180.

[67] N. A. Usov and Yu B. Grebenshchikov. "Hysteresis loops of an assembly of superparamagnetic nanoparticles with uniaxial anisotropy". In: *Journal of Applied Physics* 106.2 (2009), p. 023917. ISSN: 0021-8979. DOI: 10.1063/1.3173280.

[68] C. Whitaker et al. "High-frequency hysteresis characterization of superparamagnetic particles". In: *2015 IEEE Magnetics Conference (INTERMAG)*. IEEE, 2015, pp. 1–1. ISBN: 978-1-4799-7322-4. DOI: 10.1109/INTMAG.2015.7157564.

[69] J. Ge et al. "Superparamagnetic Composite Colloids with Anisotropic Structures". In: *Journal of the American Chemical Society* 129.29 (2007), pp. 8974–8975. ISSN: 0002-7863. DOI: 10.1021/ja0736461.

[70] A. Kolhatkar et al. "Tuning the Magnetic Properties of Nanoparticles". In: *International Journal of Molecular Sciences* 14.8 (2013), pp. 15977–16009. ISSN: 1422-0067. DOI: 10.3390/ijms140815977.

[71] J. M. Bell, M. F. Iskander, and J. J. Lee. "Ultrawideband Hybrid EBG/Ferrite Ground Plane for Low-Profile Array Antennas". In: *IEEE Transactions on Antennas and Propagation* 55.1 (2007), pp. 4–12. ISSN: 0018-926X. DOI: 10.1109/TAP.2006.888455.

[72] M. I. Kitra et al. "Low SAR Ferrite Handset Antenna Design". In: *IEEE Transactions on Antennas and Propagation* 55.4 (2007), pp. 1155–1164. ISSN: 0018-926X. DOI: 10.1109/TAP.2007.893370.

[73] M. Chen, C. C. Chen, and J. L. Volakis. "A novel textured ferrite ground plane for low-profile spiral antenna". In: *Journal of Electromagnetic Waves and Applications* 27.13 (2013), pp. 1720–1724. ISSN: 0920-5071. DOI: 10.1080/09205071.2013.823124.

[74] Rogers Corporation. *Magtrex 555 High Impedance Laminates Data Sheet*. 2019.

[75] J. Lee et al. "Role of Small Permeability in Gigahertz Ferrite Antenna Performance". In: *IEEE Magnetics Letters* 4 (2013), pp. 5000104–5000104. ISSN: 1949-307X. DOI: 10.1109/LMAG.2012.2237163.

[76] M. F. Samani and R. Safian. "On bandwidth limitation and operating frequency in artificial magnetic conductors". In: *IEEE Antennas and Wireless Propagation Letters* 9 (2010), pp. 228–231. ISSN: 15361225. DOI: 10.1109/LAWP.2010.2046390.

[77] R. Diaz. "Magnetic loading of artificial magnetic conductors for bandwidth enhancement". In: *IEEE Antennas and Propagation Society International Symposium. Digest. Held in conjunction with: USNC/CNC/URSI North American Radio Sci. Meeting (Cat. No.03CH37450)*. Vol. 2. IEEE, 2003, pp. 431–434. ISBN: 0-7803-7846-6. DOI: 10.1109/APS.2003.1219268.

[78] H. Moon et al. "An Extremely Low-Profile Ferrite-Loaded Wideband VHF Antenna Design". In: *IEEE Antennas and Wireless Propagation Letters* 11 (2012), pp. 322–325. ISSN: 1536-1225. DOI: 10.1109/LAWP.2012.2191131.

[79] X. Chen et al. "Impedance matching for omnidirectional and polarization insensitive broadband absorber based on carbonyl iron powders". In: *Journal of Magnetism and Magnetic Materials* 476.October 2018 (2019), pp. 349–354. ISSN: 03048853. DOI: 10.1016/j.jmmm.2018.12.054.

[80] M. Li et al. "A Low-Profile Dual-Polarized Dipole Antenna Using Wideband AMC Reflector". In: *IEEE Transactions on Antennas and Propagation* 66.5 (2018), pp. 2610–2615. ISSN: 0018-926X. DOI: 10.1109/TAP.2018.2806424.

[81] V. G. Syrkin et al. "Production of Phosphatized Carbonyl Iron Powders". In: *Poroshkovaya Metallurgiya* 12.11 (1973), pp. 99–101. ISSN: 1098-6596. DOI: 10.1017/CBO9781107415324.004. arXiv: arXiv:1011.1669v3.

[82] V. G. Syrkin and I. S. Tolmasskii. "Effects of Processing Parameters on the Electromagnetic Properties of Phosphatized Carbonyl Iron Powder". In: *Poroshkavoya Metallurgiya* 12.144 (1974), pp. 8–12. ISSN: 1098-6596. DOI: 10.1017/CBO9781107415324.004. arXiv: arXiv:1011.1669v3.

[83] V. G. Syrkin. "Preparation of iron powder by the thermal decomposition of iron pentacarbonyl". In: *Soviet Powder Metallurgy and Metal Ceramics* 3.3 (1965), pp. 232–239.

[84] Anritsu Company. "Understanding VNA Calibration". In: (2012), p. 16.

[85] M. Thompson. "Transmission Lines". In: *Transmission Lines*. 1999.

[86] Y. Qing et al. "Epoxy-silicone filled with multi-walled carbon nanotubes and carbonyl iron particles as a microwave absorber". In: *Carbon* 48.14 (2010), pp. 4074–4080. ISSN: 00086223. DOI: 10.1016/j.carbon.2010.07.014.

[87] Y. C. Qing et al. "Electromagnetic and microwave absorption properties of carbonyl iron and carbon fiber filled epoxy/silicone resin coatings". In: *Applied Physics A* 100.4 (2010), pp. 1177–1181. ISSN: 0947-8396. DOI: 10.1007/s00339-010-5738-5.

[88] Y. Wang et al. "Gap-Corrected Thin-Film Permittivity and Permeability Measurement with a Broadband Coaxial Line Technique". In: *IEEE Transactions on Microwave Theory and Techniques* 64.3 (2016), pp. 924–930. ISSN: 00189480. DOI: 10.1109/TMTT.2016.2519915.

[89] S. B. Cohn. "Impedance of the Shielded-Strip Transmission Line". In: *Microwave Theory and Techniques* 2.2 (1954), pp. 52–57.

[90] Analog Devices. *Microstrip and Stripline Design MT-094*, pp. 1–7.

[91] M. K. Hammood. "Impedance of Stripline". In: *Tikrit Journal of Pure Science* 17.4 (2012), pp. 144–147.

[92] A. M. Nicolson. "Broad-Band Microwave Transmission Characteristics from a Single Measurement of the Transient Response". In: *IEEE Transactions on Instrumentation and Measurement* 17.4 (1968), pp. 395–402. ISSN: 0018-9456. DOI: 10.1109/TIM.1968.4313741.

[93] A. M. Nicolson and G. F. Ross. "Measurement of the Intrinsic Properties of Materials by Time-Domain Techniques". In: *IEEE Transactions on Instrumentation and Measurement* 19.4 (1970), pp. 377–382. ISSN: 0018-9456. DOI: 10.1109/TIM.1970.4313932.

[94] W. B. Weir. "Automatic Measurement of Complex Dielectric Constant and Permeability". In: *Proceedings of the IEEE* 62.1 (1974), pp. 33–36. ISSN: 0018-9219. DOI: 10.1109/PROC.1974.9382.

[95] T. Campbell et al. "Broadband and low loss high refractive index metamaterials in the microwave regime". In: *Applied Physics Letters* 102.9 (2013), p. 091108. ISSN: 00036951. DOI: 10.1063/1.4794088.

[96] T. I. Campbell. "The Development of 3D Metamaterials with Independent and Controllable Electric and Magnetic Properties The Development of 3D Metamaterials with Independent and Controllable Electric and Magnetic Properties". MA thesis. University of Exeter 2013.

[97] S. Kim and J. Baker-jarvis. "An Approximate Approach to Determining the Permittivity and Permeability near λ / 2 Resonances in Transmission / Reflection Measurements". In: *Progress in Electromagnetics Research B* 58.January (2014), pp. 95–109.

[98] J. L. Arias et al. "Preparation and characterization of carbonyl iron/poly(butylcyanoacrylate) core/shell nanoparticles". In: *Journal of Colloid and Interface Science* 299.2 (2006), pp. 599–607. ISSN: 00219797. DOI: 10.1016/j.jcis.2006.03.005.

[99] A. S. Cushman and P. Hubbard. "Air Elutriation of Fine Powders". In: 244.1867 (1906).

[100] R. E. Pollard. "Subsieve particle-size measurement of metal powders by air elutriation". In: *Journal of Research of the National Bureau of Standards* 51.1 (1953), p. 17. ISSN: 0091-0635. DOI: 10.6028/jres.051.003.

[101] G. G. Stokes. "On the Effect of the Internal Friction of Fluids on the Motion of Pendulums". In: *Mathematical and Physical Papers* (1905), pp. 1–10. DOI: 10.1017/CBO9780511702266.002.

[102] S. Zaitsev, O. Shtempluck, and E. Buks. "Effects of electron beam induced carbon deposition on the mechanical properties of a micromechanical oscillator". In: (2011), pp. 1–4. arXiv: 1105.1049.

[103] FEI. *Helios NanoLab 450 / 450 S / 450 ML / 650 / 600i User Operation Manual*. 2012.

[104] Malvern Ltd. *Mastersizer 2000 User Manual*. 2007.

[105] D. F. Kelley, T. J. Destan, and R. J. Luebbers. "Debye function expansions of complex permittivity using a hybrid particle swarm-least squares optimization approach". In: *IEEE Transactions on Antennas and Propagation* 55.7 (2007), pp. 1999–2005. ISSN: 0018926X. DOI: 10.1109/TAP.2007.900230.

[106] K. C. Cheng et al. "Dielectric properties of epoxy resin–barium titanate composites at high frequency". In: *Materials Letters* 61.3 (2007), pp. 757–760. ISSN: 0167577X. DOI: 10.1016/j.matlet.2006.05.061.

[107] A. Patsidis and G. C. Psarras. "Dielectric behaviour and functionality of polymer matrix - Ceramic BaTiO 3 composites". In: *Express Polymer Letters* 2.10 (2008), pp. 718–726. ISSN: 1788618X. DOI: 10.3144/expresspolymlett.2008.85.

[108] C. G. Raptis, A. Patsidis, and G. C. Psarras. "Electrical response and functionality of polymer matrix-titanium carbide composites". In: *Express Polymer Letters* 4.4 (2010), pp. 234–243. DOI: 10.3144/expresspolymlett.2010.30.

[109] A. Djordjević et al. "Causal Models of Electrically Large And Lossy Dielectric Bodies". In: *Electronics and Energetics* 27.2 (2014), pp. 221–234. DOI: 10.2298/FUEE1402221D.

[110] R. Simpkin. "Derivation of Lichtenecker's Logarithmic Mixture Formula From Maxwell's Equations". In: *IEEE Transactions on Microwave Theory and Techniques* 58.3 (2010), pp. 545–550. ISSN: 0018-9480. DOI: 10.1109/TMTT.2010.2040406.

[111] L. Z. Wu et al. "High frequency complex permeability of iron particles in a nonmagnetic matrix". In: *Journal of Applied Physics* 99.8 (2006), p. 083905.

[112] S. Konda, Y. Yoshida, and O. Ichinokura. "Eddy current loss evaluation of magnetic powder core based on electric and magnetic networks". In: *AIP Advances* 7.5 (2017), p. 056678. ISSN: 2158-3226. DOI: 10.1063/1.4978587.

[113] J. Baker-Jarvis, R. G. Geyer, and P. D. Domich. "A Nonlinear Least-Squares Solution with Causality Constraints Applied to Transmission Line Permittivity and Permeability Determination". In: *IEEE Trans. Instrum. Meas.* 41.5 (1992), pp. 646–652. ISSN: 15579662. DOI: 10.1109/19.177336.

[114] J. G. Powles. "Cole-Cole plots as they should be". In: *Journal of Molecular Liquids* 56.2 (1993), pp. 35–47. ISSN: 01677322. DOI: 10.1016/0167-7322(93)80017-P.

[115] Y. Yashchyshyn and K. Godziszewski. "A New Method for Dielectric Characterization in Sub-THz Frequency Range". In: *IEEE Trans. Terahertz Sci. Technol.* 8.1 (2018), pp. 19–26. ISSN: 2156342X. DOI: 10.1109/TTHZ.2017.2771309.

[116] T. Chang et al. "Measurement of complex terahertz dielectric properties of polymers using an improved free-space technique". In: *Meas. Sci. Technol.* 28.4 (2017), p. 045002. ISSN: 13616501. DOI: 10.1088/1361-6501/aa58b5.

[117] Y. Li, L. Li, and J. Cai. "Dual-band noise suppressors based on Co/Au multilayered magnetic nanowires". In: *IEEE Transactions on Magnetics* 48.11 (2012), pp. 4398–4401. ISSN: 00189464. DOI: 10.1109/TMAG.2012.2195715.

[118] Y. Hong et al. "Design of a Multiband Antenna for LTE/GSM/UMTS Band Operation". In: *International Journal of Antennas and Propagation* 2014 (2014), pp. 1–9. ISSN: 1687-5869. DOI: 10.1155/2014/548160.

[119] F. Ahmed, M. H. M. Chowdhury, and N. Hasan. "A Compact Multiband Antenna for 4G/LTE and WLAN Mobile Phone Applications". In: *2016 3rd International Conference on Electrical Engineering and Information Communication Technology (ICEEICT)*. IEEE, 2016, pp. 1–4. ISBN: 978-1-5090-2906-8. DOI: 10.1109/CEEICT.2016.7873058.

[120] E. Ameri, S. H. Esmaeli, and S. H. Sedighy. "Wide band radar cross section reduction by thin AMC structure". In: *AEU - International Journal of Electronics and Communications* 93 (2018), pp. 150–153. ISSN: 14348411. DOI: 10.1016/j.aeue.2018.06.007.

[121] R. König et al. "The crystal structures of carbonyl iron powder – revised using in situ synchrotron XRPD". In: *Zeitschrift für Kristallographie - Crystalline Materials* 232.12 (2017), pp. 835–842. ISSN: 2196-7105. DOI: 10.1515/zkri-2017-2067.

[122] M. Kabátová, E. Dudrová, and H. Bruncková. "The effect of calcination on morphology of phosphate coating and microstructure of sintered iron phosphated powder". In: *Surface and Interface Analysis* 45.7 (2013), pp. 1166–1173. ISSN: 01422421. DOI: 10.1002/sia.5244.

[123] S. D. W. Folly and R. S. de Biasi. "Determination of Particle Size Distribution by FMR". In: *Brazilian Journal of Physics* 31.3 (2001), pp. 398–401. ISSN: 01039733. DOI: 10.1590/S0103-97332001000300009.

[124] Yu A. Kotov. *Electric explosion of wires as a method for preparation of nanopowders*. 2003. DOI: 10.1023/B:NANO.0000006069.45073.0b.

[125] BASF. *Carbonyl Iron Powder Product Sheet url:https://www.dispersions-pigments.basf.com/portal/load/fid827906/CIP_General_PO_e.pdf Last Accessed May 2018*. Tech. rep., p. 7.

[126] J. E. Japka. "Microstructure and Properties of Carbonyl Iron Powder". In: *JOM* 40.8 (1988), pp. 18–21. ISSN: 1047-4838. DOI: 10.1007/BF03258115.

[127] A. V. Lopatin et al. "The efficiency of application of magnetic polymer composites as radio-absorbing materials". In: *Journal of Communications Technology and Electronics* 53.5 (2008), pp. 487–496. ISSN: 1064-2269. DOI: 10.1134/S106422690805001X.

[128] D. Pain et al. "An improved permeameter for thin film measurements up to 6 GHz". In: *Journal of Applied Physics* 85.8 (1999), pp. 5151–5153. ISSN: 0021-8979. DOI: 10.1063/1.369107.

[129] A. Gerber et al. "Permeability and Magnetic Properties of Ferromagnetic NiFe/FeCoBSi Bilayers for High-Frequency Applications". In: *IEEE Transactions on Magnetics* 43.6 (2007), pp. 2624–2626. ISSN: 0018-9464. DOI: 10.1109/TMAG.2007.893786.

[130] Y. Liu et al. "Broadband complex permeability characterization of magnetic thin films using shorted microstrip transmission-line perturbation". In: *Review of Scientific Instruments* 76.6 (2005). ISSN: 00346748. DOI: 10.1063/1.1935429.

[131] T. Lepetit et al. "Accurate characterization of both thin and thick magnetic films using a shorted microstrip". In: *IEEE Transactions on Magnetics* 50.9 (2014). ISSN: 00189464. DOI: 10.1109/TMAG.2014.2318022.

[132] J. Eberhardt, F. Caspers, and C. Vollinger. "Ferrite Material Characterization in a Static Bias Field for the Design of a Tunaeable Cavity". In: *Proc. of IPAC 2014*. 2. 2014, pp. 6–8. ISBN: 9783954501328.

[133] J. Eberhardt, F. Caspers, and C. Vollinger. "Ferrite Characterization for the Design of an Accelerating Cavity With Perpendicular Biasing". In: *IEEE Transactions on Nuclear Science* 63.2 (2016), pp. 693–698. ISSN: 00189499. DOI: 10.1109/TNS.2015.2463091.

[134] J. Lee et al. "Control of magnetic loss tangent of hexaferrite for advanced radio frequency antenna applications". In: *Journal of Applied Physics* 113.7 (2013), p. 073909. ISSN: 0021-8979. DOI: 10.1063/1.4793089.